Karlsruhe Institute of Technology

Geophysical
Institute KIT-Dept. of Physics

Acoustic and elastic 2D full-waveform inversion of submarine gas hydrate deposits: a synthetic study

Akustische und elastische 2D Wellenforminversion von submarinen
Gashydrat-Lagerstätten: Eine synthetische Studie

Master's Thesis of

Tobias Gerach

at the KIT- Department of Physics
Geophysical Institute (GPI)

Reviewer:	Prof. Dr. Thomas Bohlen
Second reviewer:	PD Dr. Joachim Ritter
Advisor:	M.Sc. Laura Gassner

20. January 2016 – 20. February 2017

Fakultät für Physik
Karlsruher Institut für Technologie
76128 Karlsruhe

I declare that I have developed and written the enclosed thesis completely by myself, and have not used sources or means without declaration in the text.

Karlsruhe, February 17, 2017

. . . .

(Tobias Gerach)

Abstract

Gas hydrates are only stable under strict conditions known as the gas hydrate stability zone (GHSZ). Any gas that is produced below the GHSZ will be trapped as a layer of free gas in the pore space below the gas hydrate bearing sediments. Due to the elevated elastic velocities in gas hydrate bearing sediments and the significant reduction of compressional wave velocity in the partially gas saturated sediment, this interface can be mapped in seismic sections as an anomalous seismic reflector, called bottom simulating reflector (BSR). Although the BSR defines the base of the GHSZ, we cannot infer any other information about gas hydrates from it. Therefore, more advanced techniques have to be developed to quantify gas hydrate deposits.

Recent studies tried to quantify free gas and gas hydrate saturations in marine sediments using a predictive model that relates free gas and gas hydrate saturations in the pore space of sediments to seismic velocities. Therefore it is necessary to obtain highly resolved velocity models for a realistic interpretation. Seismic full-waveform inversion (FWI) is predestined for this task because of its high resolution and its capability to resolve highly heterogenous subsurfaces.

In this study, we create a 2D subsurface model containing gas hydrate and free gas bearing sediments. Utilizing this model and the acquisition geometry from a marine seismic survey in the Black Sea, we calculate synthetic observed data with a time-domain finite-difference method. Subsequently, we perform 2D acoustic and elastic FWI reconstruction tests to evaluate the imaging potential of FWI for the purpose of studying marine gas hydrate deposits.

P- and S-wave velocity characteristics of the gas hydrate and free gas bearing sediment were successfully reconstructed. Compared to acoustic FWI, elastic FWI suffers less from inversion artifacts and increases the resolution throughout the subsurface. The residual elastic energy was reduced by up to four orders of magnitude and the final model explains the observed data almost perfectly in case of acoustic FWI as well as elastic FWI.

In conclusion, seismic FWI is able to increase the overall resolution of the subsurface model compared to typical seismic imaging methods such as travel time tomography and reconstruct the properties of gas hydrate and free gas bearing sediments in marine environments. Therefore, FWI can be used to specify the extent of marine gas hydrate deposits and quantify gas hydrate and free gas saturation in marine sediments more precisely.

Zusammenfassung

Gashydrate sind nur unter bestimmten Bedingungen, der sogenannten Gashydrat Stabilitätszone (GHSZ), stabil. Gas, das unterhalb der GHSZ produziert wird, wird in den Sedimenten unterhalb der gashydrathaltigen Sedimente im Porenraum eingeschlossen. Aufgrund der erhöhten elastischen Geschwindigkeiten in gashydrathaltigen Sedimenten und der signifikanten Reduzierung der Kompressionswellengeschwindigkeit im teilweise gasgesättigten Sediment, kann dieser Übergang in seismischen Daten als irregulärer Reflektor, dem sogenannten Bottom Simulating Reflector (BSR), beobachtet werden. Obwohl ein BSR die Basis der GHSZ definiert, können daraus keine weiteren Informationen über Gashydrate abgeleitet werden. Demzufolge müssen fortgeschrittenere Methoden entwickelt werden, um Gashydrat-Lagerstätten quantifizieren zu können.

Aktuelle Studien haben versucht die Sättigung von freiem Gas und Gashydrat in marinen Sedimenten zu quantifizieren, indem sie ein Vorhersagemodell berechnet haben, welches die Sättigung von Gashydrat und freiem Gas im Porenraum mit seismischen Geschwindigkeiten in Verbindung bringt. Deshalb ist es notwendig ein hochaufgelöstes Geschwindigkeitsmodell zu erhalten um sie realistisch interpretieren zu können. Seismische Wellenforminversion ist prädestiniert für diese Aufgabe, da sie auch stark heterogene Untergründe hoch auflösend abbilden kann.

In dieser Arbeit erstellen wir ein 2D Untergrundmodell, das gashydrat- und gasgesättigte Sedimente enthält. Wir nutzen dieses Modell und die Akquisitionsgeometrie einer seismischen Erkundung im Schwarzen Meer, um synthetische, observierte Daten mit einer Finite-Differenzen Methode im Zeitbereich zu berechnen. Anschließend führen wir 2D akustische und elastische Wellenforminversion Rekonstruktionstests durch, um das Potential der Wellenforminversion bezüglich der Auflösung von Gashydrat-Lagerstätten beurteilen zu können.

Die P- und S-Wellengeschwindigkeits Eigenschaften von gashydrat- und gashaltigen Sedimenten konnte erfolgreich rekonstruiert werden. Im Vergleich zur akustischen Wellenforminversion leidet die elastische Wellenforminversion weniger unter Inversionsartefakten und erhöht die Auflösung der Sedimente im ganzen Untergrund. Das Residuum wurde um bis zu vier Größenordnungen reduziert und das finale Modell erklärt die observierten Daten nahezu perfekt.

Zusammenfassend kann gesagt werden, dass seismische Wellenforminversion es ermöglicht die Auflösung im Untergrund im Vergleich zu den üblichen seismischen Abbildungsmethoden deutlich zu verbessern und die Eigenschaften von gashydrat- sowie gasgesättigen Sedimenten korrekt zu rekonstruieren.

Contents

1. Introduction

Although renewable energy resources become more efficient and cheaper every year due to governmental subventions and new technologies, natural gas still represents more than 20 % of the world's primary energy consumption. Unfortunately, the current supply of natural gas cannot meet those demands in the long run. Marine gas hydrate deposits bind natural gas in quantities of up to 3000 Gt and could improve the balance of supply and demand drastically. However, the exploration of this unconventional energy resource is still challenging. The most efficient way to remotely probe large volumes of marine sediment is seismic reflection profiling. In the case of gas hydrate deposits in marine sediments, this is particularly true, since they can be identified by the occurrence of a bottom simulating reflector (BSR). The BSR is a characteristic strong, reversed polarity event that is considered to be the base of the gas hydrate stability zone (GHSZ) and separates the high-velocity gas hydrate bearing sediments from the underlying low-velocity free gas bearing sediments.
However, if we want to study the distribution of gas hydrates and free gas within the sediments and estimate the thickness, saturation and quantity of methane in the hydrated sediments with seismic data, we need a very detailed understanding of the elastic parameters, i.e. P- and S-wave velocity as well as density. Common seismic imaging methods such as traveltime tomography can not resolve the subsurface at the level of detail that is required. Therefore, more accurate imaging methods have to be developed and tested to study marine gas hydrate deposits. A promising solution is the application of full waveform inversion (FWI), since it uses the entire waveform, resulting in highly resolved subsurface models even in the case of strong heterogeneity. To date, only a few studies used 2D FWI to characterize gas hydrates in marine sediments. Jaiswal et al. (2012) and Delescluse et al. (2011) applied acoustic FWI in the frequency domain to 2D multichannel seismic data (MCS). Both studies concluded that FWI is a promising imaging method even with an acoustic approximation to elastic data, due to the narrow aperture of MCS which restricts mode conversion. Kim et al. (2013) used elastic FWI in the frequency domain to study gas hydrate deposits in the western part of the Ulleung Basin. Similar to the aforementioned studies, they used MCS data and observed increased P- and S-wave velocities at the location of the BSR.

In the summer of 2008, German research institutes launched the SUGAR project (Submarine Gas Hydrate Reservoirs) with the aim to produce natural gas from marine gas hydrates and to sequester CO_2 from industrial sources in marine sediments. In the scope of this project, high resolution 2D and 3D seismic surveys were conducted during cruise MSM34 onboard the German research vessel MARIA S. MERIAN from December 2013 to

January 2014 (Bialas et al., 2014) in the northwestern part of the Black Sea. Zander et al. (2016) confirmed the existence of multiple BSRs in the survey area. Therefore, we use the horizons of the 3D seismic measurements as well as velocity models resulting from traveltime tomography to construct a 2D subsurface model of the survey area. Moreover, we add a layer of gas hydrate bearing sediment and an underlying layer of free gas bearing sediment to the model, abiding by established rock-physics based gas hydrate models. We use this model and the acquisition geometry of the 2D seismic survey with ocean bottom seismometers (OBS) to simulate acoustic and elastic (pseudo-)observed data using a time-domain finite-difference scheme. Finally, we perform acoustic and elastic 2D FWI reconstruction tests in the time domain.

Thesis structure

This thesis is divided into five main chapters:
In the second chapter, we describe the essential theory needed to understand the methodological approach of this work. First, we derive the equations of motion for an elastic medium and present a numerical solution using a time-domain finite-difference (FD) method. Next, we discuss the inverse problem of the full-waveform inversion and acquire elastic gradients in the stress-displacement formulation. Furthermore, we describe the preconditioning possibilities of the gradients and finish the chapter by introducing the L-BFGS method we use to approximate the inverse Hessian.

To understand the influence of gas hydrate on seismic velocities of marine sediments, we introduce the basic information in the third chapter. Additionally, we compare the most recent empirical and rock-physics based gas hydrate models to gain insights into the physical properties of gas hydrate and free gas bearing sediments.

In the fourth chapter, we introduce the acquisition geometry, the true models and the initial models we use to simulate observed data. Moreover, we compare the results of acoustic and elastic forward modeling and specify the configuration we use for the finite-difference forward modeling scheme.

The results of the acoustic and elastic FWI reconstruction tests are shown in chapter five alongside one case study. In this case study, we investigate the influence of the initial model accuracy on the FWI result. Additionally, we examine the connection between S-wave velocity and observed artifacts in the P-wave velocity model by using an improved initial S-wave velocity model. The final full-waveform inversion involves noise contaminated data.

In the final chapter, we draw conclusions based on the previously discussed FWI results and continue to give recommendations for further investigations.

2. Theoretical background

In this chapter, we describe the essential theory that is required in this thesis. First, we derive the equations of motion for an elastic medium. Subsequently, we present a solution to these equations by using a time-domain finite-difference (FD) scheme. At last, we discuss the general full-waveform inversion (FWI) problem and the necessary tools to solve it.

2.1. Equations of motion for an elastic medium

Wave propagation in a general medium is described by a set of three equations, called the equations of motion:

$$\rho \frac{\partial^2 u_i}{\partial t^2} = \frac{\partial \sigma_{ij}}{\partial x_j} + f_i \ , \tag{2.1}$$

where ρ denotes the density, σ the stress tensor and x the vector in space of the direction $\{i, j\} = \{x, y, z\}$. They relate external body forces f_i in the medium to measurable displacements u_i, which makes them the most fundemental equations in seismology (Lay and Wallace, 1995).

To describe how a general medium reacts to external body forces, we need relationships between stress and displacement. Therefore, we use stress-strain relationships which relate stress to displacement gradients (Lay and Wallace, 1995). In the case of an elastic medium, the most general constitutive law is *Hooke's law*

$$\sigma_{ij} = C_{ijkl} \epsilon_{kl} \ . \tag{2.2}$$

The elastic moduli, C_{ijkl}, define the material properties of the medium. The infinitesimal strain tensor ϵ_{kl} is defined as

$$\epsilon_{kl} = \frac{1}{2} \left(\frac{\partial u_k}{\partial x_l} + \frac{\partial u_l}{\partial x_k} \right) \ . \tag{2.3}$$

Since many materials in Earth are considered isotropic, C_{ijkl} simplifies to two independent elastic moduli, called the *Lamé constants*, λ and μ:

$$C_{ijkl} = \lambda \delta_{ij} \delta_{kl} + \mu(\delta_{il} \delta_{jk} + \delta_{ik} \delta_{jl}) \ , \tag{2.4}$$

where δ denotes the *Kronecker delta function.* In further consequence, for an isotropic elastic medium, equation (2.2) is given by

$$\sigma_{ij} = \lambda \epsilon_{kk} \delta_{ij} + 2\mu\epsilon_{ij} \; . \tag{2.5}$$

By combining the homogenous equation of motion (eq. 2.1), Hooke's law (eq. 2.5) and the stress-displacement relationship (eq. 2.3), we can develop the three-dimensional homogenous equation of motion for a uniform, isotropic, linear elastic medium (Lay and Wallace, 1995):

$$\rho \frac{\partial^2 \mathbf{u}}{\partial t^2} = (\lambda + \mu)\nabla(\nabla \mathbf{u}) + \mu \nabla^2 \mathbf{u} \; . \tag{2.6}$$

It can be shown (Lay and Wallace, 1995) that every displacement field comprises two fundamental wave types that propagate with a distinct velocity determined by the material properties λ and μ of the medium. The wave types are P-waves with the velocity v_P and S-waves with the velocity v_S:

$$v_\mathrm{P} = \sqrt{\frac{\lambda + 2\mu}{\rho}} \, , \qquad v_\mathrm{S} = \sqrt{\frac{\mu}{\rho}} \; . \tag{2.7}$$

Equation (2.6) cannot be solved analytically for complex media, hence we need an efficient numerical solution. One such solution is presented in the next section. There we use the stress-velocity formulation of equation (2.6) by substituting $\mathbf{u}$ with $\mathbf{v} = \frac{\partial \mathbf{u}}{\partial t}$.

2.2. Solution of the elastic wave equation by finite-differences

Full-waveform inversion requires an accurate and efficient way to simulate wave propagation through complex media. The time-domain finite-difference (FD) method satisfies both conditions. We use it to approximate the partial derivatives in equation (2.6) by replacing them with discrete finite-difference operators. Therefore, we have to discretize the wave equation in space and time.

2.2.1. Discretization

The most efficient way to discretize the wave equation, is to calculate the velocity $\mathbf{v}$, the stresses σ_{ij} and the Lamé constants λ and μ at discrete cartesian coordinates

$$x = i \cdot dh \, , \qquad y = j \cdot dh \tag{2.8}$$

and at discrete times

$$t = n \cdot dt \; . \tag{2.9}$$

Therefore, every grid point is located in the intervals

$$i = 1, \ldots, N_\mathrm{x} \tag{2.10a}$$

$$j = 1, \ldots, N_\mathrm{y} \tag{2.10b}$$

$$n = 1, \ldots, N_\mathrm{t} \tag{2.10c}$$

where N_x denotes the number of grid points in x-direction, N_y the number of grid points in y-direction and N_t the number of time steps. The spatial distance between two grid points is given as dh and the sampling between two time steps is given as dt.

We use the staggered grid approach proposed by Virieux (1986) and Levander (1988), which places the model parameters (λ, μ and ρ) and the diagonal stress components σ_{kk} on integral grid points (i, j) and off-diagonal stress components and particle velocities on half integral grid points $(i + \frac{1}{2}, j + \frac{1}{2})$ as illustrated in figure 2.1. The basic idea of the finite-difference method, is to replace the partial derivatives of the wave equation with FD-operators. To obtain those operators, we consider the second-order Taylor-series of a function $f(x)$ at $x = x_0 + \Delta x$ to derive the forward operator

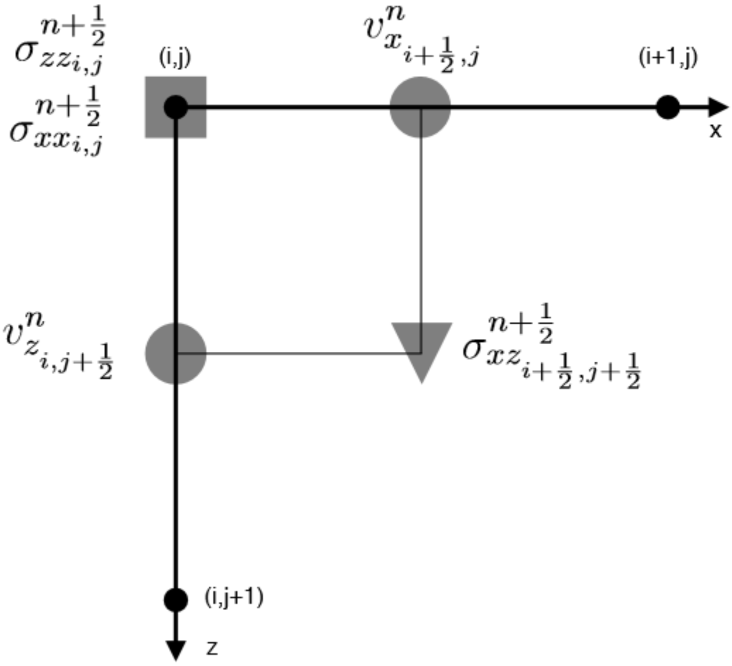

Figure 2.1.: Geometry for a standard staggered grid as proposed by Virieux (1986) and Levander (1988). Graphic modified from Wittkamp (2016).

$$D_{+} f(x_0) = \frac{f(x_0 + \Delta x) - f(x_0)}{\Delta x} + \mathcal{O}(\Delta x^2) \, , \tag{2.11}$$

and at $x = x_0 - \Delta x$ to derive the backward operator

$$D_{-}f(x_0) = \frac{f(x_0) - f(x_0 - \Delta x)}{\Delta x} + \mathcal{O}(\Delta x^2)\,. \tag{2.12}$$

If we combine equations (2.11) and (2.12) with an arithmetic mean, we get the central operator D_0. Finally, we can apply D_0 to the staggered grid to replace the spatial and temporal derivatives:

$$\frac{\partial}{\partial x} f(x) = \frac{f(i + \frac{1}{2}\Delta x) - f(i - \frac{1}{2}\Delta x)}{\Delta x} + \mathcal{O}(\Delta x^2) \tag{2.13a}$$

$$\frac{\partial}{\partial t} f(t) = \frac{f(n + \frac{1}{2}\Delta t) - f(n - \frac{1}{2}\Delta t)}{\Delta t} + \mathcal{O}(\Delta t^2) \tag{2.13b}$$

Higher order approximations of the spatial and temporal derivatives with FD-operators is possible, although only operators that are of higher-order in space are used in this work. The finite-difference scheme used was originally developed by Bohlen (1998), who shows the explicit FD-scheme for the discretized wave equation in his work.

2.2.2. Grid dispersion and instability

To ensure a stable simulation, the choice of dh and dt has to fullfill one criterion each. For analytic solutions, dh has to comply with the Nyquist-Shannon theorem $dh = \frac{\lambda}{2}$, however for numerical simulations, this is not sufficient and would result in numerical dispersion. Therefore dh has to satisfy

$$dh \leq \frac{\lambda_{\min}}{n} = \frac{v_{\min}}{n f_{\max}} \tag{2.14}$$

to avoid grid dispersion. The factor n denotes the number of grid points per minimal wavelength and depends upon the accuracy of the FD-operator (table 2.1). For $n = 16$ the simulation is accurate to the second decimal place (Daniel Köhn, 2011), although in the case of second order FD-operators, $n = 12$ should be sufficient.

The temporal discretization dt has to be chosen according to the Courant-Friedrichs-Lewy criterion (Courant et al., 1928). It states, that dt has to be smaller than the time a propagating wave needs to travel between two adjacent grid points:

$$dt \leq \frac{dh}{h\sqrt{d}\,v_{\max}}\,. \tag{2.15}$$

In the case of a two dimensional simulation $d = 2$. The factor h is dependent on the accuracy of the FD-operator. It is listed in table 2.1.

Table 2.1.: Number of grid points n per minimal wavelength and factor h required for higher order FD-operators.

FD order	n	h
2nd	12	1.0
4th	8	7/6
6th	6	149/120
8th	5	2161/1680

2.2.3. Initial and boundary conditions

To define a problem that results in a unique solution, we must specify initial and boundary conditions. As initial conditions, the particle velocity $\mathbf{v}$ and the stresses σ_{ij} as well as their derivatives have to be zero at any given location $\mathbf{x}$:

$$\mathbf{v}(\mathbf{x}, t = 0) = 0 \qquad \frac{\partial}{\partial t}\mathbf{v}(\mathbf{x}, t = 0) = 0 \tag{2.16a}$$

$$\sigma_{ij}(\mathbf{x}, t = 0) = 0 \qquad \frac{\partial}{\partial t}\sigma_{ij}(\mathbf{x}, t = 0) = 0 \tag{2.16b}$$

If we want to accurately simulate surface waves or in the case of this thesis multiple reflections in a marine environment, we have to apply a free surface boundary condition at the top of the model, i.e. all stresses have to vanish. To achieve this, we use the mirroring technique proposed by Levander (1988).

Another boundary condition is necessary to prevent reflections at artificial boundaries created by the discretized, limited subsurface model. An effective method to achieve this, is the convolutional perfectly matched layer method (C-PML). C-PMLs stretch the coordinates at the boundary by applying a coordinate transformation that maps coordinates to complex numbers, replacing propagating waves by exponentially decaying waves. The implemented C-PML method is based on Komatitsch and Martin (2007) and is applied on the lateral and inferior boundary.

2.3. Full-waveform inversion

Typical research of a physical system, such as the Earth, can generally be divided into three steps (Tarantola, 2005). The first step involves the discovery of a minimal set of model parameters $\mathbf{m} = (m_1, \ldots, m_n)^T$ that characterizes the system (**parameterization of the system**). In the second step, we use physical laws (represented by the operator $g(\cdot)$) to make predictions of measurements $\mathbf{d}_{\text{syn}}$ using a set of given values of the model parameters $\mathbf{m}$ (**forward modeling**):

$$\mathbf{d}_{\text{syn}} = g(\mathbf{m}) \,. \tag{2.17}$$

For the last step, we want to use actual field data measurements $\mathbf{d}_{\text{obs}}$ to infer values of the model parameters $\mathbf{m}$ (**inverse problem**):

$$\mathbf{m} = g^{-1}(\mathbf{d}_{\text{obs}}) \,. \tag{2.18}$$

In the case of seismic full-waveform inversion (FWI), we typically see two types of parameterizations: One in terms of density and seismic velocities $\mathbf{m} = (\boldsymbol{\rho}, \mathbf{v}_{\text{P}}, \mathbf{v}_{\text{S}})^T$ or the other in terms of density and the Lamé constants $\mathbf{m} = (\boldsymbol{\rho}, \boldsymbol{\lambda}, \boldsymbol{\mu})^T$. We discussed the forward modeling step in the previous section, where we presented a solution to the elastic wave equation by finite-differences. In the following section, we find a solution to the inverse problem using a local optimization method.

2.3.1. Inverse problem

The solution of the inverse problem of elastic wave propagation classically involves only a part of the measured seismograms, i.e. the first arrivals. The goal of full-waveform inversion is to find a model that explains every phase of the observed data. This increases the resolution capability up to half of the propagated wavelength, hence making it superior to travel time tomography. Additionally, we can obtain information about density, since we consider the amplitudes as well.

As previously mentioned, we are going to use a local optimization method. Therefore, we require an accurate initial model $\mathbf{m}_0$ as a priori information to calculate a set of synthetic data $\mathbf{d}_{\text{syn}}(\mathbf{m})$ (see chapter 2.2). This modeled data can now be compared to the observed data $\mathbf{d}_{\text{obs}}$:

$$\Delta\mathbf{d} = \mathbf{d}_{\text{syn}}(\mathbf{m}) - \mathbf{d}_{\text{obs}} \,, \tag{2.19}$$

where $\Delta\mathbf{d}$ is called misfit or data residuals. The data residuals can be measured by a vector norm. In this work, we use the least-squares L_2-norm:

$$E(\mathbf{m}) = \frac{1}{2}\Delta\mathbf{d}^T\Delta\mathbf{d} = \frac{1}{2}\sum_{\text{sources}}\int \mathrm{d}t \sum_{\text{receiver}} \Delta\mathbf{d}^2(\mathbf{x}_{\text{r}}, \mathbf{x}_{\text{s}}, t, \mathbf{m}) \,, \tag{2.20}$$

where $E(\mathbf{m})$ is called misfit or objective function. It represents the sum of the residuals over all time samples and all source and receiver positions, as well as the residual energy which cannot be explained by the synthetic model. Therefore, an optimum model can be found in a (local) minimum of the misfit function $E(\mathbf{m})$.

If we perturbate the initial model

$$\mathbf{m} = \mathbf{m}_0 + \Delta\mathbf{m} \,, \tag{2.21}$$

and consider a Taylor series of the objective function

$$E(\mathbf{m_0} + \mathbf{\Delta m}) = E(\mathbf{m}_0) + \Delta\mathbf{m}\left(\frac{\partial E(\mathbf{m}_0)}{\partial \mathbf{m}}\right) + \frac{1}{2}\Delta\mathbf{m}\left(\frac{\partial^2 E(\mathbf{m}_0)}{\partial \mathbf{m}^2}\right)\Delta\mathbf{m}^T + O(\|\Delta\mathbf{m}\|^3) \,, \tag{2.22}$$

we can find a minimum of the objective function, where its derivative vanishes:

$$\frac{\partial E(\mathbf{m})}{\partial \mathbf{m}} = \frac{\partial E(\mathbf{m}_0)}{\partial \mathbf{m}} + \Delta\mathbf{m}\left(\frac{\partial^2 E(\mathbf{m}_0)}{\partial \mathbf{m}^2}\right) \overset{!}{=} 0 \ . \tag{2.23}$$

Finally, we obtain the model perturbation $\Delta\mathbf{m}$ by rearranging equation (2.23):

$$\Delta\mathbf{m} = -\left(\frac{\partial^2 E(\mathbf{m}_0)}{\partial \mathbf{m}^2}\right)^{-1} \frac{\partial E(\mathbf{m}_0)}{\partial \mathbf{m}} = -\mathbf{H}^{-1} \cdot \nabla_{\mathbf{m}} E(\mathbf{m}_0) \ , \tag{2.24}$$

where $\nabla_{\mathbf{m}} E(\mathbf{m}_0)$ denotes the gradient of the misfit function and $\mathbf{H}$ denotes the Hessian, which contains the second derivatives of the misfit function.

Equation (2.24) requires the calculation of the inverse Hessian matrix, which, in case of large scale problems like FWI, can be very time consuming. Therefore, we approximate it using a multi-parameter L-BFGS method, that will be introduced in chapter 2.3.3. Combining equations (2.21) and (2.24), we obtain the basic local optimization scheme at iteration K:

$$\mathbf{m}_{K+1} = \mathbf{m}_K + \Delta\mathbf{m}_K = \mathbf{m}_K - \mathbf{H}_K^{-1} \cdot \nabla_{\mathbf{m}} E(\mathbf{m}_K) \ . \tag{2.25}$$

2.3.2. Gradient calculation: Adjoint state method

The local optimization method we use in our inversion procedure requires the calculation of the gradient of the misfit function $E(\mathbf{m})$. For this purpose, we use the adjoint state method proposed by Tarantola (1984) and Mora (1987).

In general, the gradient of the misfit function $E(\mathbf{m})$ can be written as

$$\begin{aligned} \frac{\partial E(\mathbf{m})}{\partial \mathbf{m}} &= \frac{1}{2} \sum_{\text{sources}} \int \mathrm{d}t \sum_{\text{receiver}} \frac{\partial \Delta\mathbf{d}^2}{\partial \mathbf{m}} \\ &= \sum_{\text{sources}} \int \mathrm{d}t \sum_{\text{receiver}} \frac{\partial \mathbf{d}_{\text{syn}}(\mathbf{m})}{\partial \mathbf{m}} \Delta\mathbf{d} \ . \end{aligned} \tag{2.26}$$

If we consider a small model perturbation $\delta\mathbf{m}$ to the synthetic data after a second order Taylor series expansion

$$\mathbf{d}_{\text{syn}}(\mathbf{m} + \delta\mathbf{m}) = \mathbf{d}_{\text{syn}}(\mathbf{m}) + \frac{\partial \mathbf{d}_{\text{syn}}(\mathbf{m})}{\partial \mathbf{m}} \delta\mathbf{m} + O(\|\delta\mathbf{m}\|^2) \ , \tag{2.27}$$

and calculate the difference to the unperturbed synthetic data $\mathbf{d}_{\text{syn}}(\mathbf{m})$, we acquire a similar mathematical expression as equation (2.26):

$$\delta\mathbf{d} = \frac{\partial \mathbf{d}_{\text{syn}}(\mathbf{m})}{\partial \mathbf{m}} \cdot \delta\mathbf{m} \ . \tag{2.28}$$

This can be interpreted as a linear mapping of a small change in the model space $\delta\mathbf{m}$ to a small change in the data space $\delta\mathbf{d}$. In continuous form, equation (2.28) can be written as

$$\delta\mathbf{d} = \int_{\mathrm{V}} \mathrm{d}V \frac{\partial \mathbf{d}_{\mathrm{syn}}(\mathbf{m})}{\partial \mathbf{m}} \delta\mathbf{m} \,, \tag{2.29}$$

as long as the Fréchet derivative $\frac{\partial \mathbf{d}_{\mathrm{syn}}(\mathbf{m})}{\partial \mathbf{m}}$ is known. As a consequence, it is possible to find the perturbation in the data space $\delta\mathbf{d}$, by integrating over all perturbations in the model space $\delta\mathbf{m}$ (Tarantola, 2005).

Equivalently, perturbations in the data space $\delta\mathbf{d}'$ can be integrated to find the perturbations in the model space $\delta\mathbf{m}'$:

$$\delta\mathbf{m}' = \sum_{\mathrm{sources}} \int \mathrm{d}t \sum_{\mathrm{receiver}} \left[\frac{\partial \mathbf{d}_{\mathrm{syn}}(\mathbf{m})}{\partial \mathbf{m}} \right]^{*} \delta\mathbf{d}' \,, \tag{2.30}$$

where the Fréchet derivative is replaced with its adjoint. Since the mapping from model to data space and vice versa is a linear operation, the Fréchet derivative and its adjoint are identical (Tarantola, 2005):

$$\left[\frac{\partial \mathbf{d}_{\mathrm{syn}}(\mathbf{m})}{\partial \mathbf{m}} \right] = \left[\frac{\partial \mathbf{d}_{\mathrm{syn}}(\mathbf{m})}{\partial \mathbf{m}} \right]^{*} \,. \tag{2.31}$$

Therefore, equations (2.26) and (2.30) are equivalent expressions, as long as the perturbations in the data space $\delta\mathbf{d}'$ are interpreted as data residuals $\Delta\mathbf{d}$:

$$\begin{aligned} \delta\mathbf{m}' &= \sum_{\mathrm{sources}} \int \mathrm{d}t \sum_{\mathrm{receiver}} \left[\frac{\partial \mathbf{d}_{\mathrm{syn}}(\mathbf{m})}{\partial \mathbf{m}} \right]^{*} \delta\mathbf{d}' \\ &= \sum_{\mathrm{sources}} \int \mathrm{d}t \sum_{\mathrm{receiver}} \frac{\partial \mathbf{d}_{\mathrm{syn}}(\mathbf{m})}{\partial \mathbf{m}} \Delta\mathbf{d} \\ &= \frac{\partial E(\mathbf{m})}{\partial \mathbf{m}} \,. \end{aligned} \tag{2.32}$$

In conclusion, we have to find a solution to the forward problem (eq. 2.29) and identify the Fréchet derivatives to calculate the gradient accordingly.

2.3.2.1. Elastic gradients for stress-displacement formulation

After the very general approach, we have to apply the adjoint state method to the equations of motion for an elastic medium. The derivation of the elastic gradients is not part of this work, hence we refer to the work of Daniel Köhn (2011) for more details. He derived the gradients for the parameterization $\mathbf{m} = (\boldsymbol{\rho}, \boldsymbol{\lambda}, \boldsymbol{\mu})^T$ and in stress-displacement formulation:

$$\frac{\partial E(\mathbf{m})}{\partial \rho} = - \sum_{\text{sources}} \int \mathrm{d}t \left(\frac{\partial u_x}{\partial t}\frac{\partial \Psi_x}{\partial t} + \frac{\partial u_z}{\partial t}\frac{\partial \Psi_z}{\partial t} \right) , \tag{2.33a}$$

$$\frac{\partial E(\mathbf{m})}{\partial \mu} = - \sum_{\text{sources}} \int \mathrm{d}t \left[\left(\frac{\partial u_x}{\partial z} + \frac{\partial u_z}{\partial x} \right) \left(\frac{\partial \Psi_x}{\partial z} + \frac{\partial \Psi_z}{\partial x} \right) + 2 \left(\frac{\partial u_x}{\partial x}\frac{\partial \Psi_x}{\partial x} + \frac{\partial u_z}{\partial z}\frac{\partial \Psi_z}{\partial z} \right) \right] , \tag{2.33b}$$

$$\frac{\partial E(\mathbf{m})}{\partial \lambda} = - \sum_{\text{sources}} \int \mathrm{d}t \left(\frac{\partial u_x}{\partial x} + \frac{\partial u_z}{\partial z} \right) \left(\frac{\partial \Psi_x}{\partial x} + \frac{\partial \Psi_z}{\partial z} \right) , \tag{2.33c}$$

where u_j denotes the forward propagated wave field and Ψ_j the backward propagated residual wave field:

$$\Psi_j(\mathbf{x}, t) = \sum_{\text{receiver}} G_{ij}(\mathbf{x}, -t; \mathbf{x}_\mathrm{R}, 0) * \delta u_i(\mathbf{x}_\mathrm{R}, t) \, . \tag{2.34}$$

These adjoint equations can be interpreted as a zero-lag cross-correlation between the incident and residual wave field. Therefore, we only need two forward simulations to calculate the gradients.

A parameterization in terms of density and the Lamé constants might not always be the best solution, since a parameterization by seismic velocities and density shows less ambiguities (Köhn et al., 2012). Therefore, we parameterize the FWI experiments in this work with $\mathbf{m} = (\boldsymbol{\rho}, \mathbf{v}_\mathrm{P}, \mathbf{v}_\mathrm{S})^T$. To obtain the gradients in respect to $\mathbf{v}_\mathrm{P}$, $\mathbf{v}_\mathrm{S}$ and ρ, we apply the chain rule on the Fréchet derivatives in the adjoint problem. Additionaly, we use the relationships between $\mathbf{v}_\mathrm{P}$, $\mathbf{v}_\mathrm{S}$, the Lamé constants λ, μ and the density ρ in equation (2.7) to derive the new gradients:

$$\frac{\partial E(\mathbf{m})}{\partial v_\mathrm{P}} = 2\rho v_\mathrm{P} \frac{\partial E(\mathbf{m})}{\partial \lambda} , \tag{2.35a}$$

$$\frac{\partial E(\mathbf{m})}{\partial v_\mathrm{S}} = -4\rho v_\mathrm{S} \frac{\partial E(\mathbf{m})}{\partial \lambda} + 2\rho v_\mathrm{S} \frac{\partial E(\mathbf{m})}{\partial \mu} , \tag{2.35b}$$

$$\frac{\partial E(\mathbf{m})}{\partial \rho} = \left(v_\mathrm{P}^2 - 2v_\mathrm{S}^2 \right) \frac{\partial E(\mathbf{m})}{\partial \lambda} + v_\mathrm{S}^2 \frac{\partial E(\mathbf{m})}{\partial \mu} + \frac{\partial E(\mathbf{m})}{\partial \rho} \, . \tag{2.35c}$$

2.3.2.2. Preconditioning of the gradients

We use the forward and backward propagated wave fields to calculate the gradients by a zero lag cross-correlation. Therefore, the gradients will suffer from the same effects as the wave fields themselves. The most prominent effect is geometrical spreading, i.e. the loss of amplitude at a distance R from the source by a factor of $1/\sqrt{R}$. This results in relatively high amplitudes in the vicinity of the sources and adjoint sources (receiver), which leads to concentrated model updates in these areas. To counteract this behavior, we apply different types of preconditioning to the gradients.

The first one is a circular shape taper that is applied locally around the source positions. It sets the gradient to zero at the source position itself and increases logarithmically to one at the boundary of the circle.

The radius of the circle is given in grid points and is applied shotwise. The second class of preconditioning is applied globally and it represents an approximation of the diagonal elements of the Hessian for one source each (Plessix and Mulder, 2004), which accounts for the effect of geometrical spreading:

$$\mathbf{H}_\mathrm{a}^{-1}(\mathbf{x}_\mathrm{s},\mathbf{x}) = \left[\varepsilon + \int \mathrm{d}t |\mathbf{u}(\mathbf{x}_\mathrm{s},\mathbf{x},t)|^2 \left(\operatorname{asinh}\left(\frac{x_\mathrm{r}^\mathrm{max} - x}{z}\right) - \operatorname{asinh}\left(\frac{x_\mathrm{r}^\mathrm{min} - x}{z}\right)\right)\right]^{-1} , \qquad (2.36)$$

where $x_\mathrm{r}^\mathrm{min}$ and $x_\mathrm{r}^\mathrm{max}$ denote the minimum and maximum receiver positions for the source location $\mathbf{x}_\mathrm{s}$ respectively. With ε we introduce a water level, which ensures the stability of the inversion by damping areas, where less or no waves propagate.

2.3.3. Hessian approximation with a multi-parameter L-BFGS method

We mentioned in chapter 2.3.1, that an exact calculation of the Hessian is too costly for the size of the FWI problem. Therefore, we use a limited-memory version of the quasi-Newton Broyden-Fletcher-Goldfarb-Shanno (BFGS) method, also known as L-BFGS, to approximate the inverse Hessian. In the following, we outline the key points to this method based on Nocedal and Wright (2006) and Brossier (2011).

The L-BFGS method differs from its unlimited version as such, that it saves memory by only using the last n most recent iterations. Therefore, only the gradient differences

$$\mathbf{y}_\mathrm{K} = \nabla_\mathbf{m} E(\mathbf{m})_{\mathrm{K}+1} - \nabla_\mathbf{m} E(\mathbf{m})_\mathrm{K} \qquad (2.37)$$

and the model differences

$$s_\mathrm{K} = \mathbf{m}_{\mathrm{K}+1} - \mathbf{m}_\mathrm{K} \qquad (2.38)$$

for the last n iterations have to be stored to calculate the approximated inverse Hessian. Nocedal and Wright (2006) suggest, that a total of 3 to 20 iterations is sufficient. Using equations (2.37) and (2.38) the L-BFGS algorithm returns the model updates

$$\Delta\mathbf{m}_\mathrm{K} = -\mathbf{H}_\mathrm{K}^{-1} \nabla_\mathbf{m} E(\mathbf{m})_\mathrm{K} \qquad (2.39)$$

directly. Furthermore, this allows us to calculate the new model:

$$\mathbf{m}_{\mathrm{K}+1} = \mathbf{m}_\mathrm{K} + \alpha_\mathrm{K} \cdot \Delta\mathbf{m}_\mathrm{K} \, , \qquad (2.40)$$

where α_K denotes the step length. For the algorithm to work, it is necessary to acquire an initial guess of the Hessian beforehand. We calculate the initial guess $\mathbf{H}_{0\mathrm{K}}$ with the gradient and model differences from the previous iteration:

$$\mathbf{H}_{0\mathrm{K}} = \frac{\mathbf{s}_{\mathrm{K}-1}^T \mathbf{y}_{\mathrm{K}-1}}{\mathbf{y}_{\mathrm{K}-1}^T \mathbf{y}_{\mathrm{K}-1}} \cdot \mathbf{I} \, , \qquad (2.41)$$

which is why we have to use a classical steepest descent model update using a parabolic line search to estimate the step length α_K every time we make a significant change in the inversion process.

2.3.3.1. Wolfe conditions

To ensure, that all model updates bring the objective function closer to a local minimum, we have to satisfy the basic curvature condition:

$$\mathbf{s}_\mathrm{K}^T \cdot \mathbf{y}_\mathrm{K} > 0 \ , \tag{2.42}$$

which implies that the inverse Hessian is positive definite. This can be accomplished, if the step length α satisfies the Wolfe conditions (Nocedal and Wright, 2006). The first condition is called *sufficient decrease condition*:

$$E(\mathbf{m} + \alpha \Delta \mathbf{m}) \leq E(\mathbf{m}) + c_1 \alpha \cdot \nabla_\mathbf{m} E(\mathbf{m})^T \cdot \Delta \mathbf{m} \ , \tag{2.43}$$

where c_1 is a constant value between zero and one. For our purposes $c_1 = 0$ is used, which is sufficient and guarantees a steady decrease of the misfit function without compromising the inversion.
The second Wolfe condition is called *curvature condition* and refuses a step length, if it would lead to a too small improvement of the misfit function:

$$\nabla_\mathbf{m} E(\mathbf{m} + \alpha \Delta \mathbf{m})^T \cdot \Delta \mathbf{m} \geq c_2 \cdot \nabla_\mathbf{m} E(\mathbf{m})^T \cdot \Delta \mathbf{m} \ . \tag{2.44}$$

The parameter c_2 is set to 0.9 in accordance with Nocedal and Wright (2006).

2.3.3.2. Line search

In equation (2.40), we introduced the step length α to the quasi-Newton model update scheme. The line search algorithm is always initiated with a step length of $\alpha = 1$. In most cases, $\alpha = 1$ satisfies the Wolfe conditions and is therefore used in subsequent iterations. If any of the Wolfe conditions is not met, the step length is reduced and will be retested. A step length that meets the second Wolfe condition but does not meet the first will be rejected and increased, until both conditions are fulfilled.

3. Physical properties of gas hydrate bearing sediments

The most suitable method to detect large distributions of gas hydrate bearing sediments is to acquire seismic reflection and refraction profiles. However, from seismic methods we can only infer elastic properties. Recent studies tried to quantify gas hydrate saturation in marine sediments using a predictive model that relates gas hydrate saturation in the pore space of sediments to seismic velocities. Therefore, we need a very good understanding of the elastic properties of the hydrate-sediment composite.

In this chapter, we give a short introduction on gas hydrate and outline different mathematical models to describe the physical properties of gas hydrate bearing sediments, which we later use to create the synthetic test model for our FWI experiments.

3.1. Introduction

Gas hydrates are crystalline compounds composed of a gas molecule that is surrounded by a cagelike structure of water molecules. The most common and naturally occurring gas hydrate is composed of water and methane. Hydrate formation is possible, wherever plenty of water is available in the vicinity of gas at temperatures above and below 273 K and at high ambient pressures (Sloan, 1998). The zone where all these conditions apply is called *gas hydrate stability zone* (GHSZ).

The aforementioned stability conditions can be found in marine sediments and in permafrost environments. Figure 3.1 shows the redrawn phase diagrams from Kvenvolden and Lorenson (2001) which show the temperature and water depth required to form stable gas hydrate in marine sediments. Assuming that salty oceanic water cannot get any colder than 1.8 °C and that the average temperature increase is 3 °C per 100 m of sediment depth, figure 3.1 shows that gas hydrate cannot be stable at 100 m water depth. Therefore, in case of a seafloor in 1000 m water depth, we could expect an up to 600 m thick layer of gas hydrate. The true width of the gas hydrate layer obviously depends on the actual thermal gradient of the sediment and the sufficient supply of free gas in the area.

Burwicz et al. (2011) calculated the global GHSZ thickness based on global bathymetry, salinity, water temperature and heat flow. Their calculations predict up to 800 m thick zones in high-altitude regions and over 500 m thick zones along continental margins.

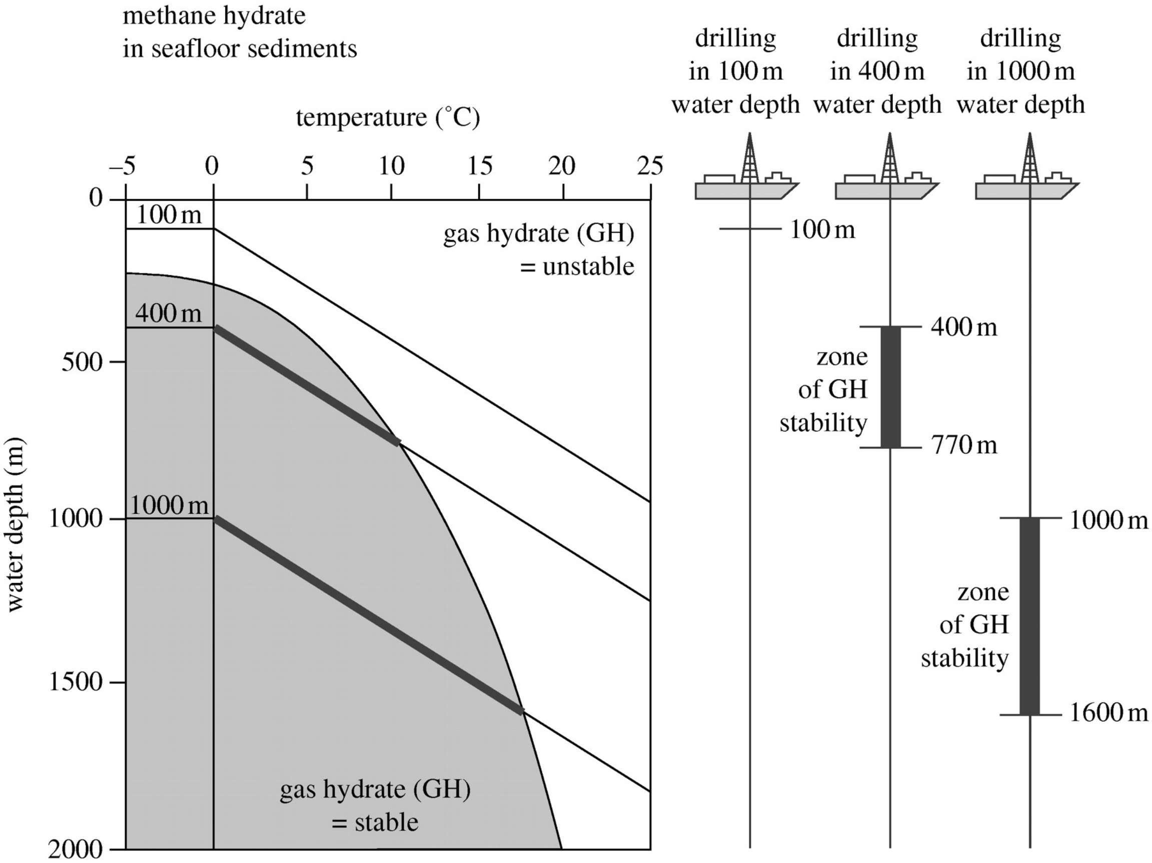

Figure 3.1.: Phase diagram, showing the temperature and water depth required for the stability of gas hydrate in marine sediments (redrawn from Kvenvolden and Lorenson (2001))

The base of the GHSZ is an essential characteristic for seismic surveys in hydrate bearing sediments, since it often acts as an anomalous reflector with reversed polarity, called *bottom simulating reflector* (BSR). This is due to the fact that the temperatures in the sediment become too warm at a certain depth to support solid gas hydrates. Therefore, any gas produced below the hydrated sediment will be trapped as a layer of free gas in the pore space. A BSR indicates the lower boundary of gas hydrate stability and can be observed even when little hydrate is present. Although, a BSR needs not to be observed in hydrate bearing sediment (Klauda and Sandler, 2005). Further, even if a BSR exists, it cannot give any information about the gas hydrate saturation in the sediment. To quantify gas hydrates from seismic data, a solid inversion method for the elastic parameters and rock-physics based models are necessary. A short overview of the most recent models is given in the next section.

3.2. Comparison of rock-physics based gas hydrate models

Seismic detection of gas hydrate occurrences is possible due to hydrate stiffening the host sediment and therefore increasing the P- and S-wave velocities. J.-Y. Lee (2007) demonstrated this effect comprehensively in hydrate-bearing clay, silt and sand at different stress and hydrate saturation levels. The propagation of seismic waves is controlled by the sediment's small-strain bulk modulus, $K_\mathrm{b} = \lambda + \frac{2}{3}G$, and the shear modulus, $G = \mu$, according to equation (2.7). Therefore, P and S waves are sensitive to different material properties: the bulk modulus K_b is sensitive to the grain and pore fluid properties, however the shear modulus G is sensitive to the shear stiffness of the mineral skeleton.
The density ρ can also be interpreted as the bulk sediment density ρ_b, which is a volume average of the individual densities, as a function of porosity ϕ and phase saturations S:

$$\rho_\mathrm{b} = \phi\rho_\mathrm{fl} + (1-\phi)\rho_\mathrm{m} \text{ with } \rho_\mathrm{fl} = \rho_\mathrm{w}S_\mathrm{w} + \rho_\mathrm{h}S_\mathrm{h} + \rho_\mathrm{g}S_\mathrm{g} \tag{3.1}$$

where the subscripts w, h, g and m describe the water, gas, hydrate and mineral phases respectively.

Several ways to calculate the elastic moduli have been proposed in the past. The most important one originates from Gassmann (1951). Gassmann's equations relate the bulk modulus of a rock to its pore, frame and fluid properties and is used to model elastic moduli and density of reservoirs by fluid substitution. The Gassmann equation yields

$$K_\mathrm{b} = K_\mathrm{sk} + \frac{\left(1 - \frac{K_\mathrm{sk}}{K_\mathrm{m}}\right)^2}{\frac{\phi}{K_\mathrm{fl}} + \frac{1-\phi}{K_\mathrm{m}} - \frac{K_\mathrm{sk}}{K_\mathrm{m}^2}}\,, \tag{3.2}$$

where K_fl is the bulk modulus of the substituted fluid and K_sk denotes the bulk modulus of the sediment skeleton and is defined as

$$K_\mathrm{sk} = \frac{2(1+\nu_\mathrm{sk})}{3(1-2\nu_\mathrm{sk})}G\,, \tag{3.3}$$

using the standard theory of elasticity relation and the Poisson ratio for the skeleton ν_sk. Alongside Gassmann's equations, there have been further developments that often use equation (3.2) as a starting point. The following paragraphs shortly summarize the most recent methods used to model the elastic parameters of gas hydrate bearing sediments.

Empirical models An empirical model based on a weighted combination of the time-average equation (Pearson et al., 1983)

$$\frac{1}{v_\mathrm{P,Avg}} = \frac{\phi(1-S_\mathrm{h})}{v_\mathrm{P,w}} + \frac{\phi S_\mathrm{h}}{v_\mathrm{P,h}} + \frac{(1-\phi)}{v_\mathrm{P,m}} \tag{3.4}$$

and the Wood equation (Nobes et al., 1986)

$$\frac{1}{\rho_\mathrm{b} v_\mathrm{P,Wood}^2} = \frac{\phi(1-S_\mathrm{h})}{\rho_\mathrm{w} v_\mathrm{P,w}^2} + \frac{\phi S_\mathrm{h}}{\rho_\mathrm{h} v_\mathrm{P,h}^2} + \frac{(1-\phi)}{\rho_\mathrm{m} v_\mathrm{P,m}^2} \tag{3.5}$$

has been developed by M. W. Lee et al. (1996) to relate seismic velocities to gas hydrate quantities:

$$\frac{1}{v_\mathrm{P}} = \frac{W\phi(1-S_\mathrm{h})^n}{v_\mathrm{P,Wood}} + \frac{1-W\phi(1-S_\mathrm{h})^n}{v_\mathrm{P,Avg}} \,, \tag{3.6}$$

where W denotes a weighting factor and n is a constant simulating the rate of lithification with hydrate concentration. A value of $W > 1$ favors the Wood equation and $W < 1$ favors the time-average equation. Furthermore, the weighted equation approaches the time-average equation for increasing n and decreasing ϕ, since $(1 - S_\mathrm{h}) \leq 1$.
Pearson et al. (1983) applied the time-average equation to gas hydrate bearing rocks and concluded that it was adequate to describe hydrate bearing sediment in consolidated media. However, the time-average equation could not predict observed velocities consistently and had to be used with an artificially low matrix velocity for unconsolidated sediments (M. W. Lee et al., 1996). The Wood equation is valid for particles in suspension and the predictions from this equation form a lower limit when compared with velocity values from observed data. M. W. Lee et al. (1996) overcomes these problems of the previously mentioned methods, by combining them with a weighting factor W and an exponent n to favor either greater consolidation and rigidity (time-average equation) or greater saturation (Wood equation). The main criticism of the weighted equation is that it uses an empirical relation (time-average equation) as part of its equations. Figure 3.2 shows the predictions for velocities and hydrate concentrations for porosities from 30 % to 80 % for P- and S-waves.

Effective medium theory (EMT) Gas hydrate bearing sediments have been modeled using effective medium theory by Helgerud et al. (1999) and Jakobsen et al. (2000). Based on the rock-physics model proposed by Dvorkin et al. (1999)

$$K_\mathrm{sk} = \begin{cases} \left[\frac{\phi/\phi_\mathrm{c}}{K_\mathrm{HM}+\frac{4}{3}G_\mathrm{HM}} + \frac{1-\phi/\phi_\mathrm{c}}{K_\mathrm{m}+\frac{4}{3}G_\mathrm{HM}}\right]^{-1} - \frac{4}{3}G_\mathrm{HM} & \text{if } \phi < \phi_\mathrm{c}\,, \\ \left[\frac{(1-\phi)/(1-\phi_\mathrm{c})}{K_\mathrm{HM}+\frac{4}{3}G_\mathrm{HM}} + \frac{(\phi-\phi_\mathrm{c})/(1-\phi_\mathrm{c})}{\frac{4}{3}G_\mathrm{HM}}\right]^{-1} - \frac{4}{3}G_\mathrm{HM} & \text{if } \phi \geq \phi_\mathrm{c}\,; \end{cases} \tag{3.7a}$$

$$G_\mathrm{sk} = \begin{cases} \left[\frac{\phi/\phi_\mathrm{c}}{G_\mathrm{HM}+Z} + \frac{1-\phi/\phi_\mathrm{c}}{G_\mathrm{m}+Z}\right]^{-1} - Z & \text{if } \phi < \phi_\mathrm{c}\,, \\ \left[\frac{(1-\phi)/(1-\phi_\mathrm{c})}{G_\mathrm{HM}+Z} + \frac{(\phi-\phi_\mathrm{c})/(1-\phi_\mathrm{c})}{Z}\right]^{-1} - Z & \text{if } \phi \geq \phi_\mathrm{c}\,; \end{cases} \tag{3.7b}$$

$$Z = \frac{G_\mathrm{HM}}{6}\left(\frac{9K_\mathrm{HM} + 8G_\mathrm{HM}}{K_\mathrm{HM} + 2G_\mathrm{HM}}\right) \,, \tag{3.7c}$$

where

$$K_\mathrm{HM} = \left[\frac{n^2(1-\phi_\mathrm{c})^2G_\mathrm{m}^2}{18\pi^2(1-\nu_\mathrm{m})^2}P\right]^{\frac{1}{3}} \,, \quad G_\mathrm{HM} = \frac{5-4\nu_\mathrm{m}}{5(2-\nu_\mathrm{m})}\left[\frac{3n^2(1-\phi_\mathrm{c})^2G_\mathrm{m}^2}{2\pi^2(1-\nu_\mathrm{m})^2}P\right]^{\frac{1}{3}} \tag{3.8}$$

are the effective bulk and shear moduli at critical porosity ϕ_c given by the Hertz-Mindlin contact theory (Mindlin, 1949), n is the average number of contacts per grain in a sphere pack at ϕ_c, P is the effective pressure and the subscript m indicates the properties of the mineral phase respectively. The effective pressure P is calculated as the difference between lithostatic and hydrostatic pressure

$$P = (\rho_\mathrm{b} - \rho_\mathrm{w})gD \,, \tag{3.9}$$

where g is the acceleration due to gravity and D is the depth below sea floor. We can calculate the elastic moduli ($K_\mathrm{m}, G_\mathrm{m}$) of the mineral phase using the Voigt-Reuss-Hill average equation:

$$K_\mathrm{m} = \frac{1}{2}\left[\sum_{i=1}^{k} f_i K_i + (\sum_{i=1}^{k} f_i/K_i)^{-1}\right] \,, \quad G_\mathrm{m} = \frac{1}{2}\left[\sum_{i=1}^{k} f_i G_i + (\sum_{i=1}^{k} f_i/G_i)^{-1}\right] \,, \tag{3.10}$$

where k is the number of mineral constituents and f_i the volumetric fraction of the i-th constituent in the solid phase.

Helgerud predicted the velocity of gas hydrate bearing sediments consistent with observed well log data using physics based parameters only. He considered two possible formation scenarios: (a) hydrate is part of the pore fluid and therefore does not affect the stiffness of the dry frame and (b) hydrate is a component of the dry frame which reduces the porosity and alters the solid phase properties. In case (a), the concentration of gas hydrate in the pore space is given by $S_\mathrm{h} = C_\mathrm{h}/\phi$, where C_h is the volumetric concentration of hydrate in the rock. If we assume that hydrate and water are homogeneously distributed throughout the pore space, the effective bulk modulus of the pore fluid can be calculated using the Reuss average

$$K_\mathrm{fl} = [S_\mathrm{h}/K_\mathrm{h} + (1 - S_\mathrm{h})/K_\mathrm{w}]^{-1} \,. \tag{3.11}$$

Equations (3.7), (3.10) and (3.11) can now be used to calculate the elastic moduli, and therefore the velocities, of a sediment saturated with a composite pore fluid with equation (3.2). In this case, the shear modulus G_b is the same as that of the dry frame ($G_\mathrm{b} = G_\mathrm{sk}$). In case (b), hydrate reduces the original porosity ϕ to $\phi^* = \phi - C_\mathrm{h}$ and changes the effective mineral moduli as calculated in equation (3.10), where f_i is replaced with

$$f_i^* = f_i(1 - \phi)/(1 - \phi^*) \,. \tag{3.12}$$

Additionally, gas hydrate has to be treated as a mineral component:

$$f_\mathrm{h} = \frac{C_\mathrm{h}}{1 - \phi^*} \,. \tag{3.13}$$

After comparing his predicted values with observed data, Helgerud's conclusion was that hydrate acts as a load bearing component of the sediment. One drawback of EMT is that it predicts unreasonably high v_s values at higher porosities.

Modified Biot-Gassmann-theory (BGTL) The method by M. W. Lee (2002) assumes that the velocity ratio (v_p to v_s) of an unconsolidated sediment is related to the velocity ratio of the matrix material of the formation and its porosity. Gas hydrate is considered to be

part of the frame with no consolidation or cementation present.
The variation of $\delta(V_{\mathrm{fl}})$ in the volume of the pore fluid as a function of the variation in the hydraulic pressure $\delta(p)$ and the variation in the volume $\delta(V)$ of the formation yields (Biot, 1941):

$$\delta(V_{\mathrm{fl}}) = \frac{\delta(p)}{M} + \beta\delta(V)\,, \tag{3.14}$$

where the Biot coefficient β measures the ratio of the change in fluid volume to the change in formation volume and is a function of the formation porosity. M measures the variation in hydraulic pressure necessary to force an amount of water into the formation without any change in formation volume. The Biot coefficient β and the term M can be used to link the Lamé coefficient λ of the formation to the Lamé coefficient of the skeleton λ_{sk} by the following equation:

$$\lambda = \lambda_{\mathrm{sk}} + \beta^2 M\,. \tag{3.15}$$

Gassmann's theory connects the bulk modulus of the formation (K_{b}) and its skeleton (K_{sk}). Using the bulk modulus of the mineral matrix (K_{m}), we can reformulate equation (3.2) to

$$K_{\mathrm{sk}} = K_{\mathrm{m}}(1-\beta) \text{ and } K_{\mathrm{b}} = K_{\mathrm{m}}(1-\beta) + \beta^2 M\,. \tag{3.16}$$

Furthermore, Gassmann's theory shows that M is dependant on β:

$$\frac{1}{M} = \frac{(\beta-\phi)}{K_{\mathrm{M}}} + \frac{\phi}{K_{\mathrm{fl}}}\,. \tag{3.17}$$

To derive the shear modulus of the formation (G_{b}), we assume the following relationship between v_{P} an v_{S} by M. W. Lee et al. (1996):

$$v_{\mathrm{S}} = v_{\mathrm{P}}\alpha(1-\phi)\,, \tag{3.18}$$

where $\alpha = (v_{\mathrm{P}}/v_{\mathrm{s}})^{-1}$. Using equations (2.7), (3.18) and (3.16) the shear modulus of the formation can be written as

$$G_{\mathrm{b}} = \frac{G_{\mathrm{m}}K_{\mathrm{m}}(1-\beta)(1-\phi)^2 + G_{\mathrm{m}}\beta^2 M(1-\phi)^2}{K_{\mathrm{m}} + 4G_{\mathrm{m}}(1-(1-\phi)^2)/3}\,. \tag{3.19}$$

Equation (3.15) indicates that $\beta^2 M$ approaches zero as soon as porosity approaches zero, since λ and λ_{sk} are identical at $\phi = 0$. In this case, equation (3.19) can be approximated by

$$G_{\mathrm{b}} = G_{\mathrm{m}}(1-\beta)\,, \tag{3.20}$$

meaning that β can be obtained if the shear modulus or the S-wave velocity of the mineral matrix is known with respect to porosity. M. W. Lee (2002) assumes in his theory that the shear modulus G_{b} is given by the shear velocities predicted from the weighted equation or EMT.

Figure 3.3 shows the velocities predicted by BGTL and EMT methods in terms of water-filled porosity for gas hydrate bearing sediments with porosities of $\phi = 20\,\%$, $30\,\%$ and $40\,\%$ and a volume clay content of $30\,\%$. Additionally, the velocity of non gas hydrate bearing

sediment is plotted. At 0% water-filled porosity, the pore space is fully saturated with gas hydrate. The velocities of the non-gas hydrate bearing sediment can be interpreted that $\phi = 0$ at 0 % water-filled porosity.
Equation (3.2) suggests that the presence of free gas has a significant effect in decreasing the bulk modulus K_b ($K_\mathrm{g} \ll K_\mathrm{w}, K_\mathrm{h}$ and K_m) and the P wave velocity, whereas the decrease in bulk density ρ_b is insignificant in comparison. Even at low gas saturations v_p rapidly approaches approx. $1.5v_\mathrm{s}$.
With these insights, we can now construct a proper model to calculate the (pseudo-) observed data (chapter 4) to perform the FWI reconstruction tests. A comprehensive overview of all relevant physical properties of gas hydrate is given by Waite et al. (2009).

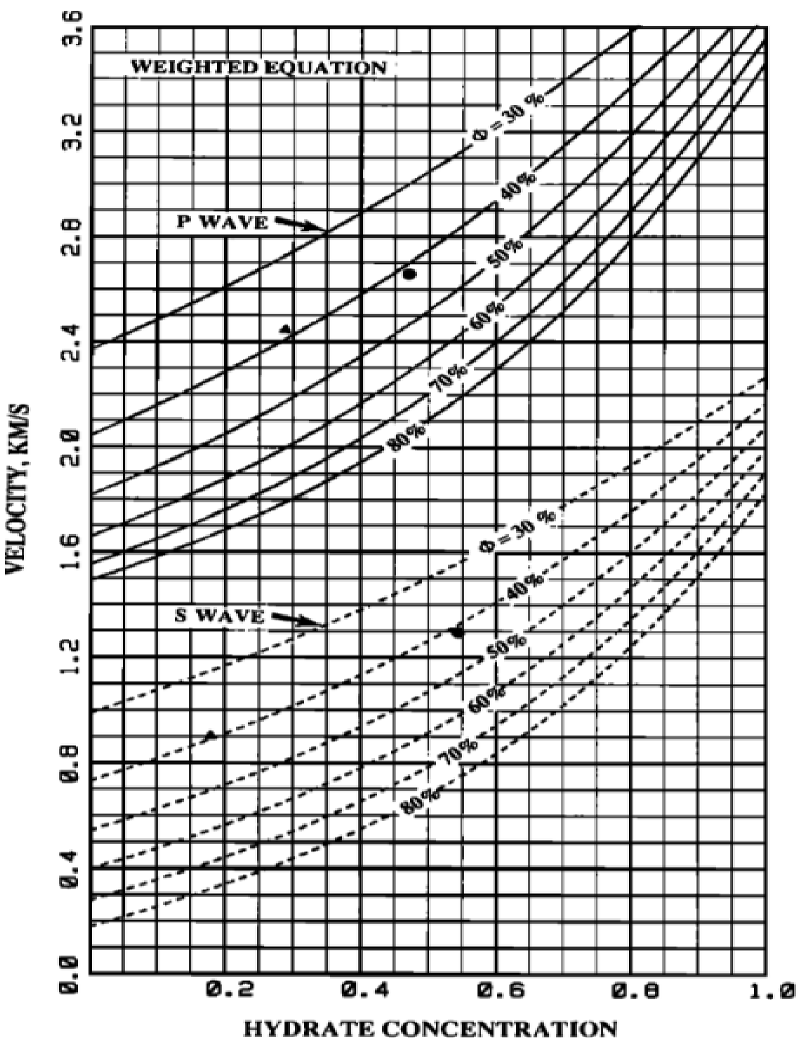

Figure 3.2.: Velocities predicted by the weighted equation for gas hydrate bearing sediments with respect to porosity and hydrate concentration in the pore space using $W = 1.0$ and $n = 1$. Dots and triangles indicate observed P- and S-wave velocities from permafrost samples. Adapted from M. W. Lee et al. (1996).

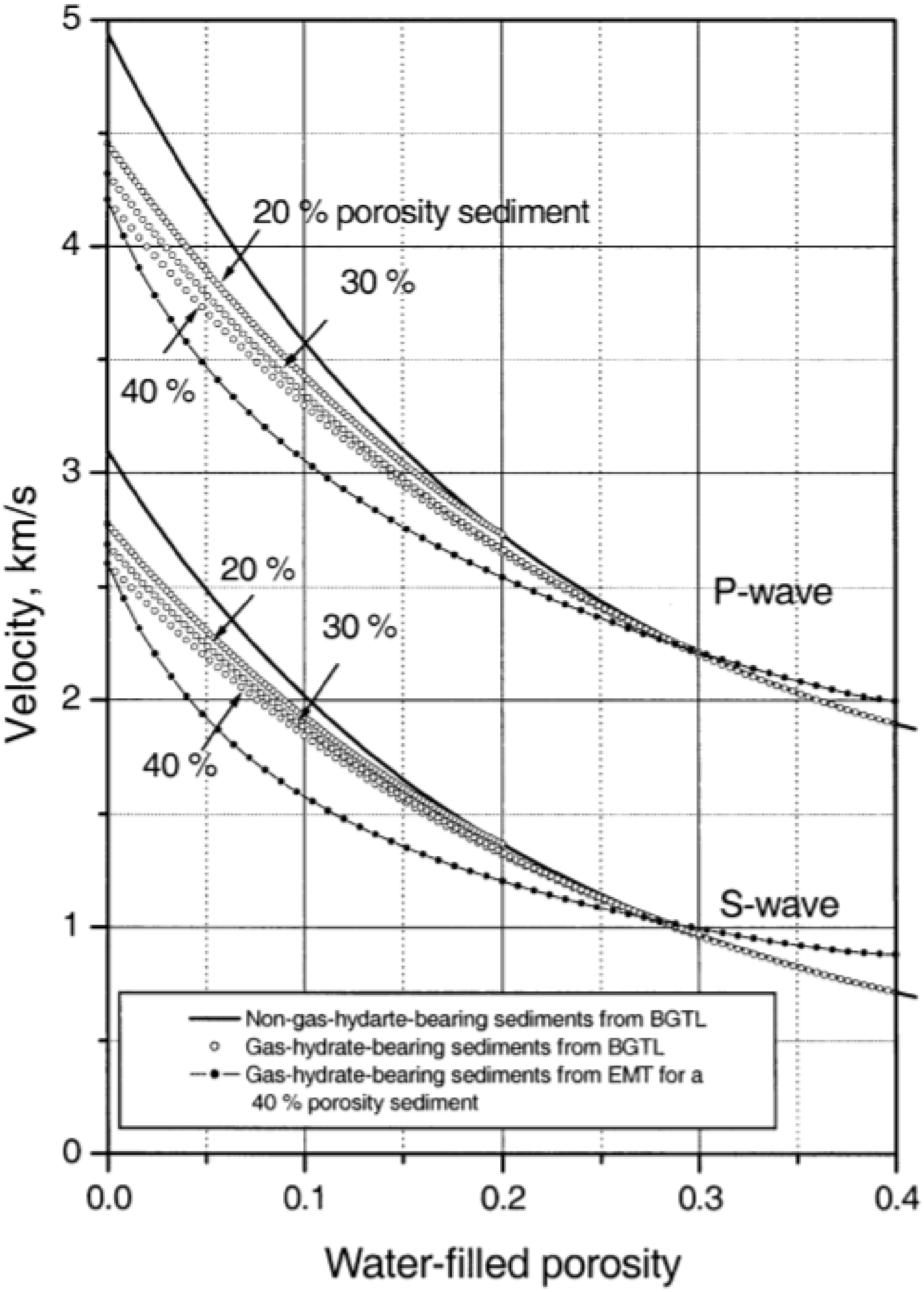

Figure 3.3.: Velocities predicted by the BGTL and EMT methods for gas hydrate bearing sediments with a porosity of ϕ =20 %, 30 % and 40 % and a volume clay content of 30 %. Adapted from M. W. Lee (2002).

4. (Pseudo-)Observed data

In this chapter, we describe the acquisition geometry and the subsurface model, as well as the setup of the finite-difference forward modeling scheme (see chapter 2.2) used to generate pseudo-observed data. The obtained seismograms serve as a set of true data for the reconstruction tests we conduct in chapter 5. Furthermore, we compare acoustic with elastic forward modeling to identify possible P- to S-wave conversion.

4.1. Setting

Within the scope of the SUGAR project, a marine seismic survey, which confirmed the existence of multiple BSR, was conducted from December 2013 to January 2014. We use the acquisition geometry, picked horizons and traveltime tomography results of this survey to construct a subsurface model with the best transferability to the field data. An exemplary seismogram of the field data acquired in the northwestern part of the Black Sea is shown in figure 4.1. The data was filtered with a 4th order Butterworth low-pass filter with a cutoff frequency of $f_c = 30\,\text{Hz}$.

4.1.1. Acquisition geometry

The field data acquisition in the Black Sea used five ocean bottom seismometers (OBS) and 1690 shots. The OBS were equipped with a hydrophone and a three-component seismometer. A GI-airgun was used to generate seismic waves in an interval of 5 s (equivalent to roughly 10 m shot distance) and a water depth of 2 m.
To downscale the amount of disk space required for the inversion, we reduce the number of shots to 169 without any loss in resolution. Additionally, we take advantage of the reciprocity theorem. This allows us to exchange source and receiver positions, which drastically improves computational efficiency. A validation of the reciprocity theorem in conjunction with the FD scheme described in chapter 2.2 can be found in section A.2 of the appendix. Therefore, we only need to simulate five shots instead of 169. Figure 4.2 shows the acquisition geometry used in this study. The receivers are placed in a water depth of 10 m instead of 2 m due to the choice of spatial discretization. The sources are placed at the first grid point above the seafloor for the pressure data, and at the first grid

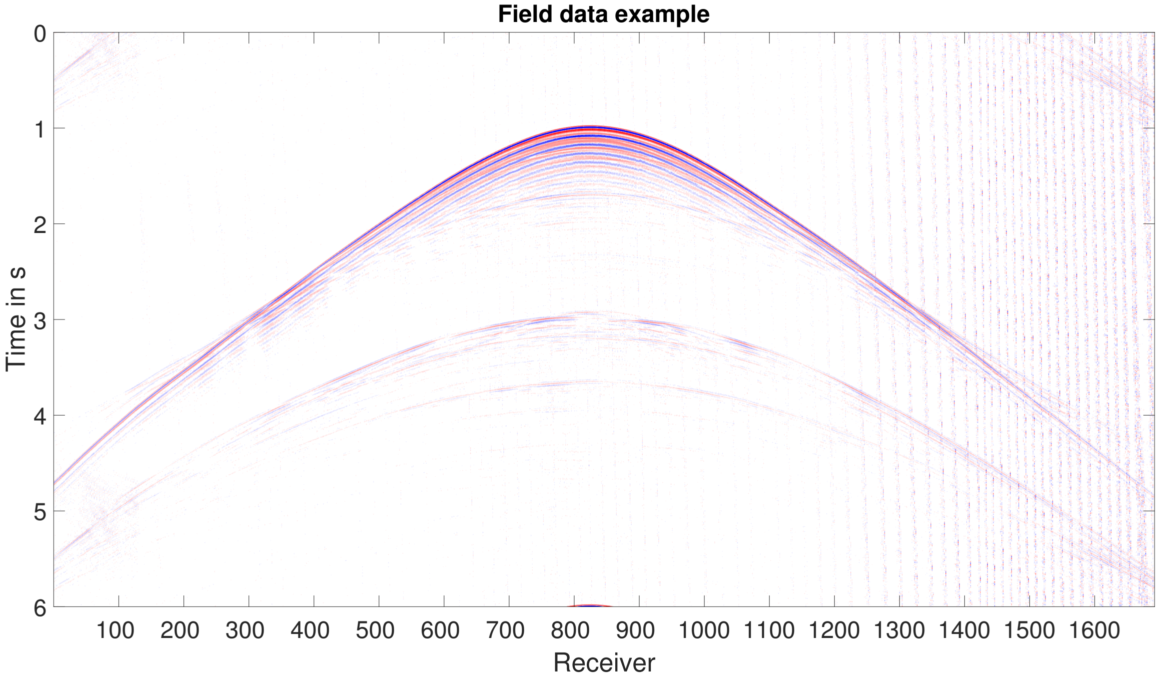

Figure 4.1.: Exemplary field data acquired in the northwestern part of the Black Sea. A 4th order Butterworth low-pass filter with a cutoff frequency of $f_c = 30\,\text{Hz}$ was applied to allow a qualitative comparison with the forward modeled (pseudo-) observed data.

point below the seafloor for the particle velocity data at their respective X-coordinates. Only the source positions of the pressure data is mapped to improve visibility. Hereafter, we only show the subsurface model and inversion results inside the area of the dashed black line to improve clarity, since the subsurface model consists of over 50 % water.

4.1.2. True and initial models

The true models are based on horizons, which were obtained from a high resolution 3D P-Cable survey during the field data acquisition in the Black Sea. The fourth horizon is corresponds to the BSR reflection. We create the v_P background model by averaging a provided travel time tomography model to fit the sediment layers divided by the horizons. The background v_S model is calculated from the v_P model using constant $\frac{v_\text{P}}{v_\text{S}}$-ratios ranging from 2.75 to 2.2 from sea floor to the bottom of the model for each layer respectively. These values are not necessarily realistic. Especially the shallow sediments in our model, where $\frac{v_\text{P}}{v_\text{S}}$-ratios of 5 to 7 are more common, have higher velocities. However, using such low S-wave velocities increases the computational requirements drastically, since it would require less than half the spatial discretization to forward model data with the same frequency content. The density model is calculated from v_P using Gardner's

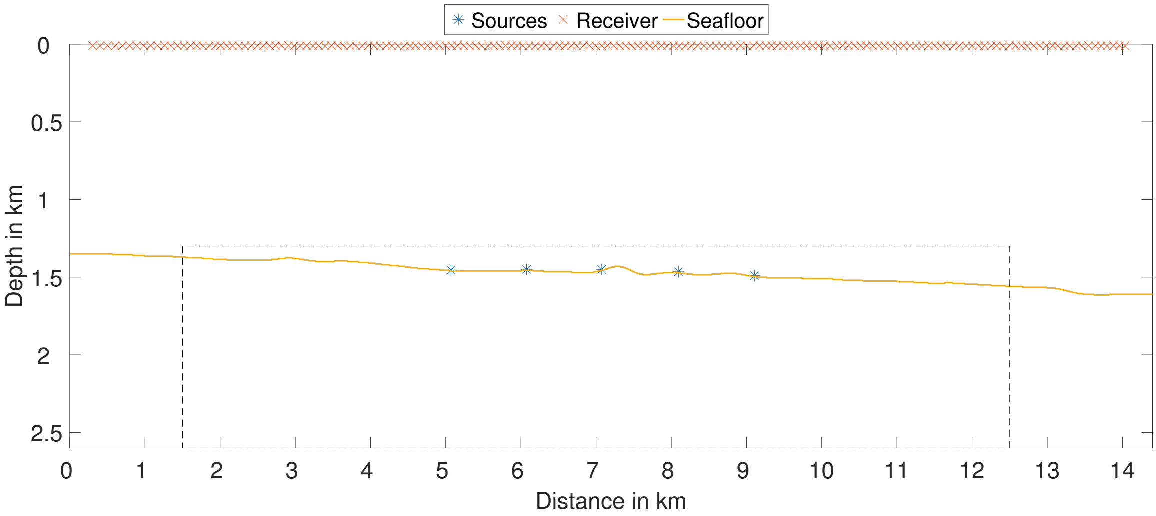

Figure 4.2.: Acquisition geometry used in this study. Blue stars denote the source positions and red crosses the receiver positions. The yellow line marks the seafloor depth. Hereafter, only the area inside the dashed black line is considered.

relation (Gardner et al., 1974):

$$\rho = 0.31 \cdot v_{\mathrm{P}}^{0.25} , \tag{4.1}$$

where v_{P} is given in units of m/s and ρ is given in units of g/cm^3.
In chapter 3.2, we showed how gas hydrate and free gas change the characteristics, especially the velocities, of marine sediments. Therefore, we use the rock-physics based gas hydrate models of Helgerud et al. (1999) and M. W. Lee (2002) to adjust the velocities above and below the BSR. We assume that gas hydrate is stable above the BSR, thus increasing P- and S-wave velocities. The gas hydrate concentration steadily increases from 0 % to approx. 25 % leading up to the BSR, since free gas supply is highest at the base of the GHSZ. This increases P-wave velocity by 300 m/s and S-wave velocity by 200 m/s in comparison to the background model. Below the BSR, we assume an accumulation of free gas in the range of 1 % to 5 % pore space saturation. We inferred from Gassmann's equation (eq. 3.2) that low concentrations of free gas in the pore space lead to a rapid decrease in P-wave velocity, thus decreasing P-wave velocity by 300 m/s compared to the background model. The influence of gas hydrate and free gas on density is negligible. Therefore, we keep the background density model unchanged. The initial models are derived from the true models, shown in figure 4.4 (left column), by filtering the true models in the frequency domain with a 2D Gaussian window

$$w(n) = \mathrm{e}^{-\frac{1}{2}\left(\alpha\frac{n}{(N-1)/2}\right)^2} = \mathrm{e}^{-n^2/2\sigma^2} , \tag{4.2}$$

where $-(N-1)/2 \leq n \leq (N-1)/2$ and α is inversely proportional to the standard deviation, σ, of a Gaussian random variable. The exact correspondence between α and σ is $\sigma = (N-1)/(2\alpha)$. The parameters of the Gaussian window are $N_{\mathrm{X}} = X+2\alpha$, $N_{\mathrm{Z}} = Z+2\alpha$ and $\alpha = 100$, where $X = 14.4$ km and $Z = 2.6$ km are the horizontal width and depth of the model respectively. Figure 4.3 shows the corresponding cross sections at $X = 6000$ m of the true and initial P- and S-wave velocities as well as density.

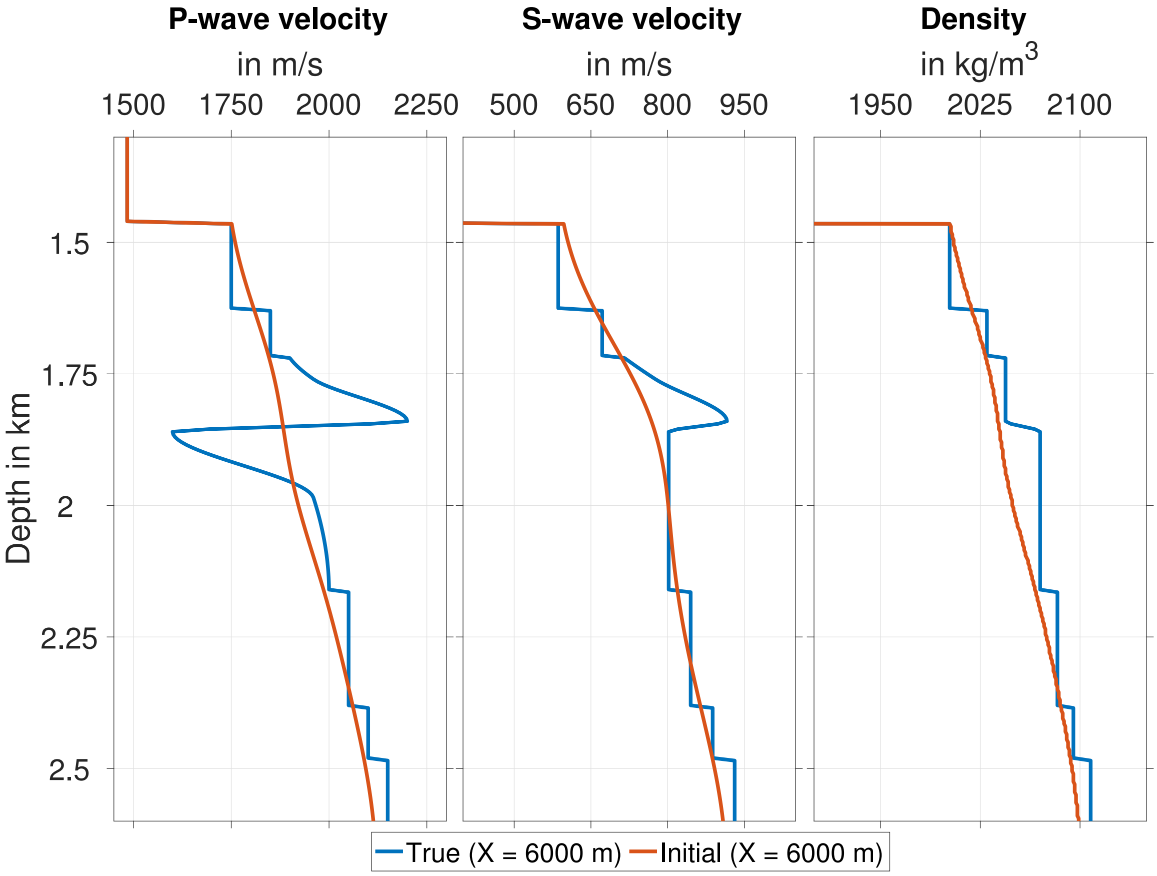

Figure 4.3.: Cross section of the true and initial models for P-wave velocity, S-wave velocity and density.

4.2. Forward modeling

In this section, we introduce the parameters for the forward modeling of the observed data and compare the results of acoustic and elastic forward modeling for pressure data.

4.2.1. Setup

We use the finite-difference forward modeling scheme described in chapter 2.2 to generate the observed data from the true model shown in figure 4.4 and the acquisition geometry in figure 4.2. For the simulation of these data, we discretize the model on an equidistant grid using a spacing of 5.0 m and use a temporal sampling of $5.0 \cdot 10^{-4}$ s. A free surface boundary condition is applied at the top of the model. To prevent artificial reflections from the remaining edges of the model, we apply a C-PML boundary with a width of 30 grid points. Additionally, we use an explosive source for the pressure data and a unidirectional force as a source for the components of the particle velocity data. To satisfy the grid

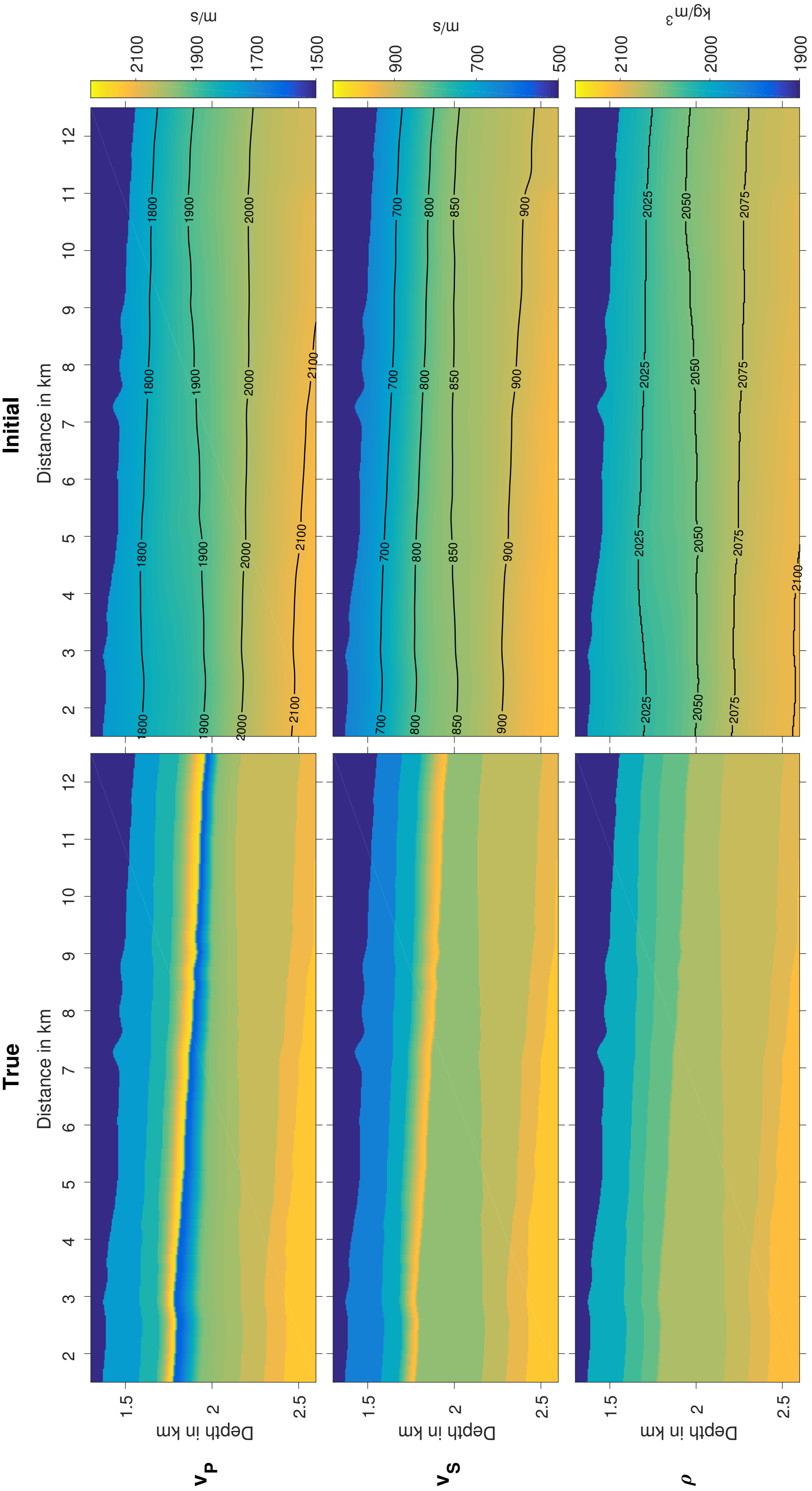

Figure 4.4.: Section of the 2D true and initial models for v_P, v_S and ρ, which contain sediment layers saturated with gas hydrate and free gas.

dispersion and instability criteria described in chapter 2.2.2, we use a Ricker wavelet

$$r(\tau) = (1 - 2\tau^2)\mathrm{e}^{-\tau^2} \text{ with } \tau = \frac{\pi(t - 1.5/f_\mathrm{p})}{1/f_\mathrm{p}}\,, \tag{4.3}$$

with a peak frequency of $f_\mathrm{p} = 10\,\mathrm{Hz}$ as a source wavelet. Figure 4.5 shows the applied source wavelet in the time and frequency domain.

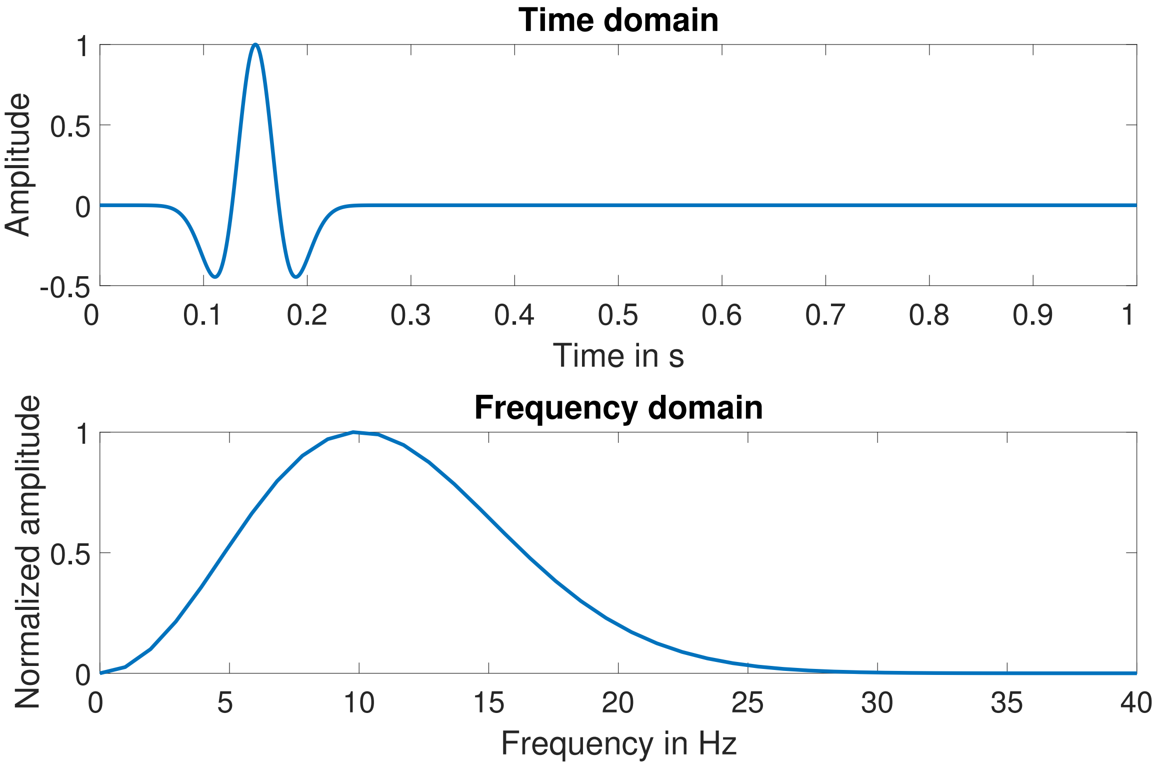

Figure 4.5.: Ricker wavelet in the time (top) and frequency (bottom) domain with a peak frequency of $f_\mathrm{p} = 10\,\mathrm{Hz}$.

An exemplary seismogram of the forward modeled data with the true model is given in figure 4.6 for the first shot. We can distinguish three major phases in the wavefield: the direct wave, reflected waves and refracted waves. The direct wave is mixed with the reflection of the seafloor due to the source positioning. The most prominent reflection originates from the BSR horizon and can be identified by its reversed polarity. Reflections from the shallow and deep sedimentary layers are considerably weaker. After roughly 3 s, the first multiple reflections arrive at the receivers that are closest to the source position. At far offsets, we can identify refracted waves arriving after 3.3 s.
The bandwidth of the modeled data reaches from 3 Hz to a maximum of 32 Hz and is shown in figure 4.7.

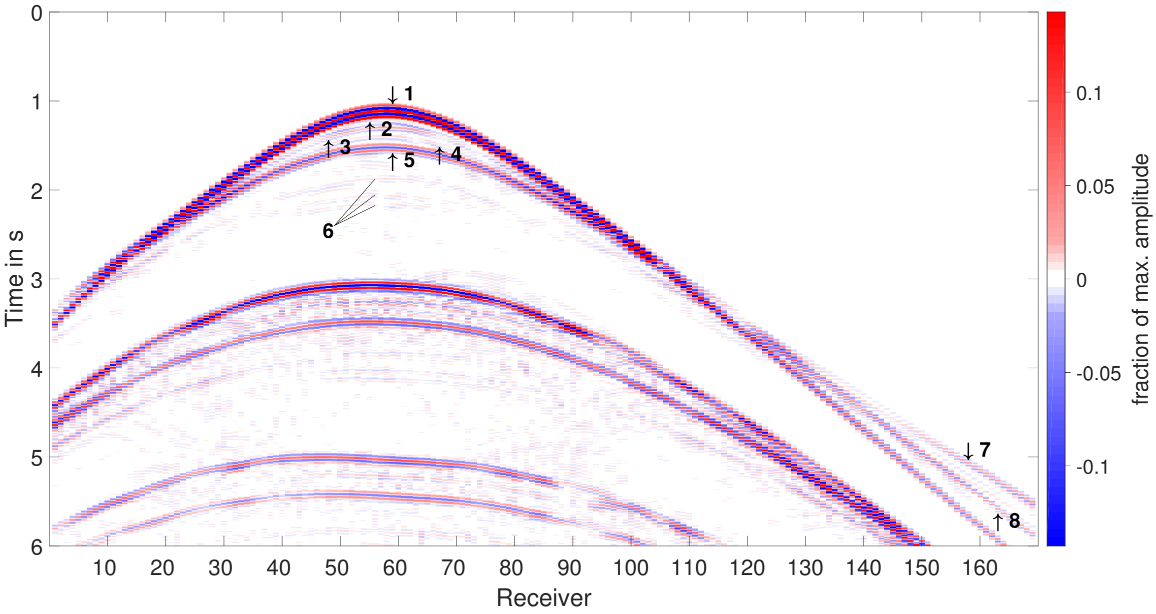

Figure 4.6.: Exemplary shot of the observed pressure data. Amplitudes are heavily clipped to make smaller phases visible. The numbers represent the following phases: 1: direct wave; 2: seafloor reflection; 3 and 4: shallow sedimentary layer reflections; 5: BSR reflection; 6: deep sedimentary layer reflections; 7: refracted wave from the seafloor; 8: refracted wave from the BSR.

4.2.2. Acoustic vs. elastic forward modeling

Seismic data acquisition in marine environments utilizes an explosive source that is triggered under water. Therefore, it is reasonable to use acoustic forward modeling and inversion as a first tool, since we only emit acoustic waves into the subsurface. Although in reality, once the wavefield reaches the ocean sediments, P- to S-wave conversion is possible. This is not considered in the acoustic FD and FWI codes and might lead to artifacts when using field data. To be able to properly interpret the inversion results of acoustic full-waveform inversion, it is necessary to identify the major differences between the acoustic and elastic forward modeled data.

Figure 4.9 shows the data residuals of the acoustic and elastic forward modeled data. We can see that the amplitude of the reflected and refracted wavefields is the most significant difference. Additionally, the residuals are bigger in the mid- to far-offset range, whereas the least model errors can be found close to the source. This is an indicator for P- to S-wave conversion especially at the water-seafloor interface. Nonetheless, we can identify several phases that are completely missing in the acoustic forward modeled data.

The significant differences in signal amplitude between the reflected acoustic and elastic wavefields in the mid- to far-offset range can be explained with the Zoeppritz equations. With the Zoeppritz equations, we can calculate angle-dependent reflection and transmis-

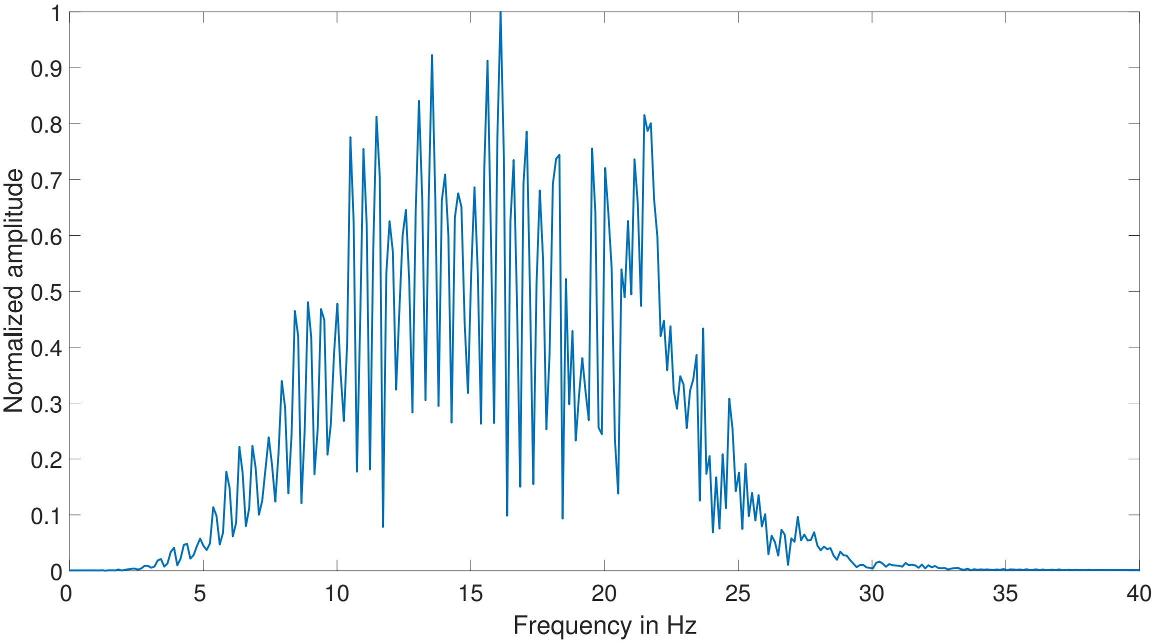

Figure 4.7.: Frequency content of the data shown in figure 4.6.

sion coefficients for elastic waves at a non-slip horizontal boundary between two horizontal isotropic elastic media. Figure 4.8 shows the relative amplitudes of the reflected (Rpp and Rps) and transmitted (Tpp and Tps) waves for an incoming P-wave as a function of the incidence angle on the water-seafloor interface given in our model. The critical incident angle is at about 58° and P- to S-wave conversion is highest in the mid- and far-offset regions.

We can see in figure 4.10 that the wavefields at near-offsets match almost perfectly. For mid- to far-offsets, we see increasing differences in signal amplitude.

4.3. Summary

We created a 2D subsurface model containing gas hydrate bearing sediments with an underlying layer of sediment partially saturated with free gas. The background velocity model, reflection horizons as well as the acquisition geometry are based on a set of field data measurements in the northwestern Black Sea. This subsurface model was used to simulate a set of observed data using a time-domain finite-difference scheme to solve the acoustic and elastic wave equations. We found that the differences in the data of acoustic and elastic forward modeling are considerable, despite using a marine acquisition geometry. The main differences were identified to be the result of wave conversion at the sediment interfaces. Furthermore, the differences are more pronounced in mid- to far-offset regions.

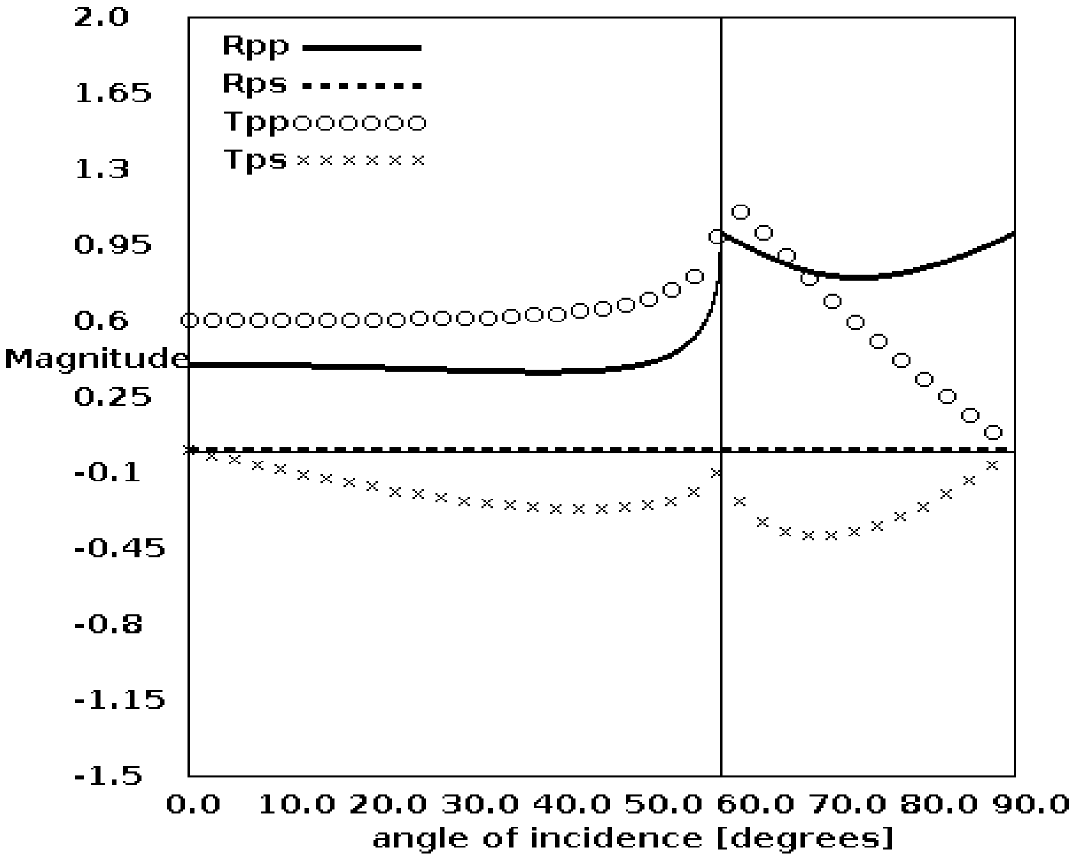

Figure 4.8.: Relative amplitudes of the reflected (Rpp and Rps) and transmitted (Tpp and Tps) waves for an incoming P-wave as a function of the incidence angle calculated with the Zoeppritz Magnitude Plotter 1.0 applet (Consortium for Research in Elastic Wave Exploration Seismology, 2017).

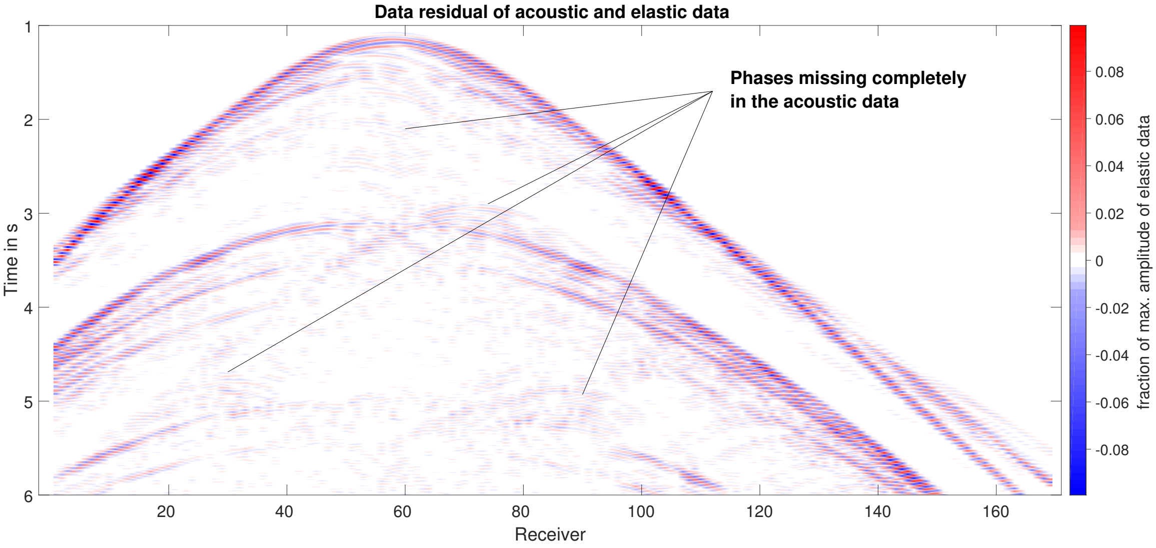

Figure 4.9.: Data residuals $\Delta\mathbf{d}$ of the acoustic and elastic forward modeled data. Amplitudes are shown as a fraction of the maximum amplitude of the observed elastic data.

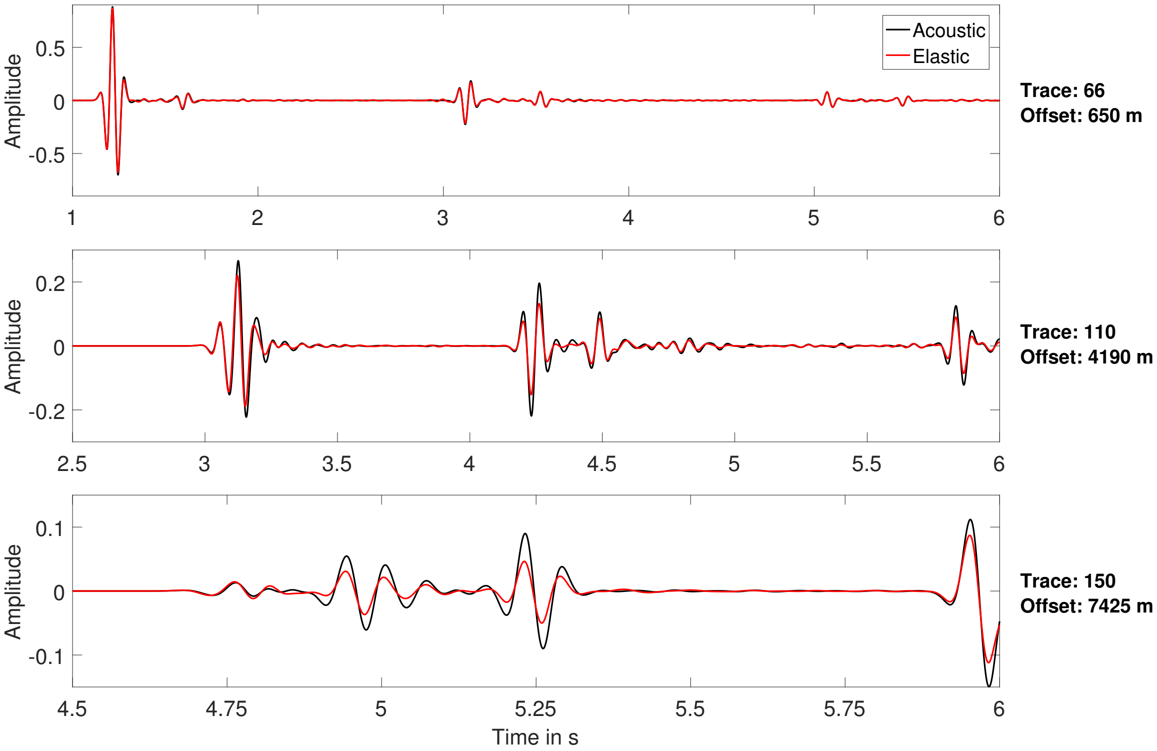

Figure 4.10.: Comparison of acoustic and elastic forward modeled data for different offsets. The data was simulated using the model shown in figure 4.4 with pressure receivers.

5. FWI reconstruction tests

In this chapter, we present the workflow as well as results for the acoustic and elastic full-waveform inversion reconstruction tests. The reconstruction tests are performed with the FWI software **IFOS** (**I**nversion of **F**ull **O**bserved **S**eismograms), which is maintained by the Geophysical Institute of the Karlsruhe Institute of Technology (KIT). It is published and distributed on the GitLab server at the KIT and can be found at `https://git.scc.kit.edu/GPIAG-Software/IFOS2D`.

5.1. FWI setup

We perform the reconstruction tests for the gas hydrate containing subsurface model presented in the previous chapter. The smoothed model shown in figure 4.4 is used as an initial model. The gradient is calculated with the adjoint state method presented in chapter 2.3.2. Additionally to the preconditioning methods mentioned in chapter 2.3.2.2, we apply a simple taper to the water column of the model. All gradient values inside the water column will be set to zero. This is reasonable, since v_P, v_S and ρ of water and the location of the seafloor both are typically well defined and we do not need model updates in this region. We use a radius of 125 m for the circular taper that is applied at the source positions.
As an objective function, we use the least-squares L_2-norm between the synthetic data simulated during the inversion and the observed data. To ensure the stability of the finite-difference forward modeling scheme, we set a lower limit for the $v_\mathrm{P}/v_\mathrm{S}$-ratio of 1.2 and restrict model updates for v_P, v_S and ρ to the values given in table A.2 in appendix A.
The inversion process is divided into multiple stages to have better control over the model parameters and frequency content. We gradually increase the frequency content from 5 Hz to 25 Hz, by increasing the corner frequency of the fourth order Butterworth low-pass filter in 5 Hz steps. Furthermore, the model parameters are introduced sequentially to the inversion process. First, we only allow updates of v_P until the automatic abort criterion is reached. We start with v_P, since marine data acquisition is most sensitive to compressional waves. Second, we invert for v_P and v_S simultaneously. Finally, we run the full multi-parameter inversion until the misfit can no longer be decreased. The complete inversion workflow is shown in table 5.1 for the acoustic FWI and in table 5.2 for the elastic FWI. A minimum of 3 iterations is performed at the beginning of each workflow stage.

Table 5.1.: Multi-stage workflow for the acoustic FWI.

Stage	Updates		Abort criterion in %	LP filter in Hz
	v_P	ρ		
1	yes	no	1	5
2	yes	yes	1	5
3	yes	yes	1	10
4	yes	yes	1	15
5	yes	yes	1	20
6	yes	yes	1	25

Table 5.2.: Multi-stage workflow for the elastic FWI.

Stage	Updates			Abort criterion in %	LP filter in Hz
	v_P	v_S	ρ		
1	yes	no	no	1	5
2	yes	yes	no	1	5
3	yes	yes	yes	1	5
4	yes	yes	yes	1	10
5	yes	yes	yes	1	15
6	yes	yes	yes	1	20
7	yes	yes	yes	1	25

5.2. Acoustic FWI

We only record acoustic waves in marine seismics. Therefore, it is reasonable to perform the first reconstruction test with acoustic FWI. In other words we neglect all information about shear waves and converted waves which are presumably present in the observed data. First we perform an acoustic reconstruction test with acoustic forward modeled data to be able to evaluate the resolution capabilities of FWI with omitted S-wave information before we perform an acoustic reconstruction test with the more realistic elastic forward modeled data.

The acoustic forward modeled data was successfully reconstructed by the acoustic FWI. We resolved the layer of gas hydrate bearing sediments as well as the layer containing free gas in its full extent. Furthermore, the sediment interfaces of the background velocity model could be resolved up to the full depth of the model. The lateral resolution is limited to the area shown in figure 5.3 (1.5 km to 12.5 km) due to the limited wavefield coverage in the left- and rightmost parts of the subsurface model. The reconstruction of the background density model is successful for the location of the sedimentary interfaces, but the density values themselves deviate from the real values by about 15 kg/m^3. In the area of the gas hydrates and free gas bearing sediments, the reconstructed density model

is inconsistent. It shows more fluctuation compared to other parts of the model.
The fit of the final synthetic seismograms is close to perfect for all offsets. The remaining data residual is hardly visible. Figure 5.2 shows the evolution of the objective function. The misfit reduces smoothly and is four orders of magnitude smaller for the last subsurface model of the inversion. All sudden increases of the misfit function are explained by a change in frequency content through a progression in the workflow stages.

The acoustic FWI of the elastic observed data was able to reveal the gas hydrate and free gas bearing sediment, as shown in figure 5.4. However, the P-wave velocity of the gas hydrate bearing sediment is underestimated by up to 150 m/s. Nevertheless, the P-wave velocity of the free gas bearing sediment layer as well as its location is resolved well. In contrast to the FWI with acoustic data, we could not reconstruct the sediment interfaces of the background model. Additionally, using elastic data with acoustic FWI introduced a significant amount of inversion artifacts to the subsurface model. The first few grid points of the sediment show substantially elevated velocities as well as circular shaped artifacts around the source positions. Moreover, the P-wave velocity model shows lateral inhomogeneities that appear in an equidistant pattern especially in the deeper parts of the model. They are roughly located below the source positions and are strongest below the middle source. The most plausible reason for these artifacts is the missing S-wave velocity information.
The reconstruction of the density model was not successful. It is dominated by strong artifacts with values that deviate up to 300 kg/m^3 from the true model and shows similar patterns when compared to the artifacts in the P-wave velocity model. This suggests that the strong artifacts in the density model are a result of cross-talk by the v_P gradients, since the P-wave velocity artifacts are already visible in the first workflow stage, where density is not considered.
The remaining data residuals, displayed in figure 5.1, show the biggest differences in the amplitude of the seafloor reflection similar to the differences we observed in chapter 4.2.2, when we compared the acoustic forward modeled data to the elastic forward modeled data. However, there is relatively low residual energy for all other reflections even though the interfaces which cause these reflections were not reconstructed properly. The phases that were completely missing in the acoustic forward modeled data , miss in the acoustic FWI as well and were not fitted to the elastic observed data. As shown in figure 5.2, the misfit could be reduced continuously. However, it did not improve as significantly as with the acoustic data.

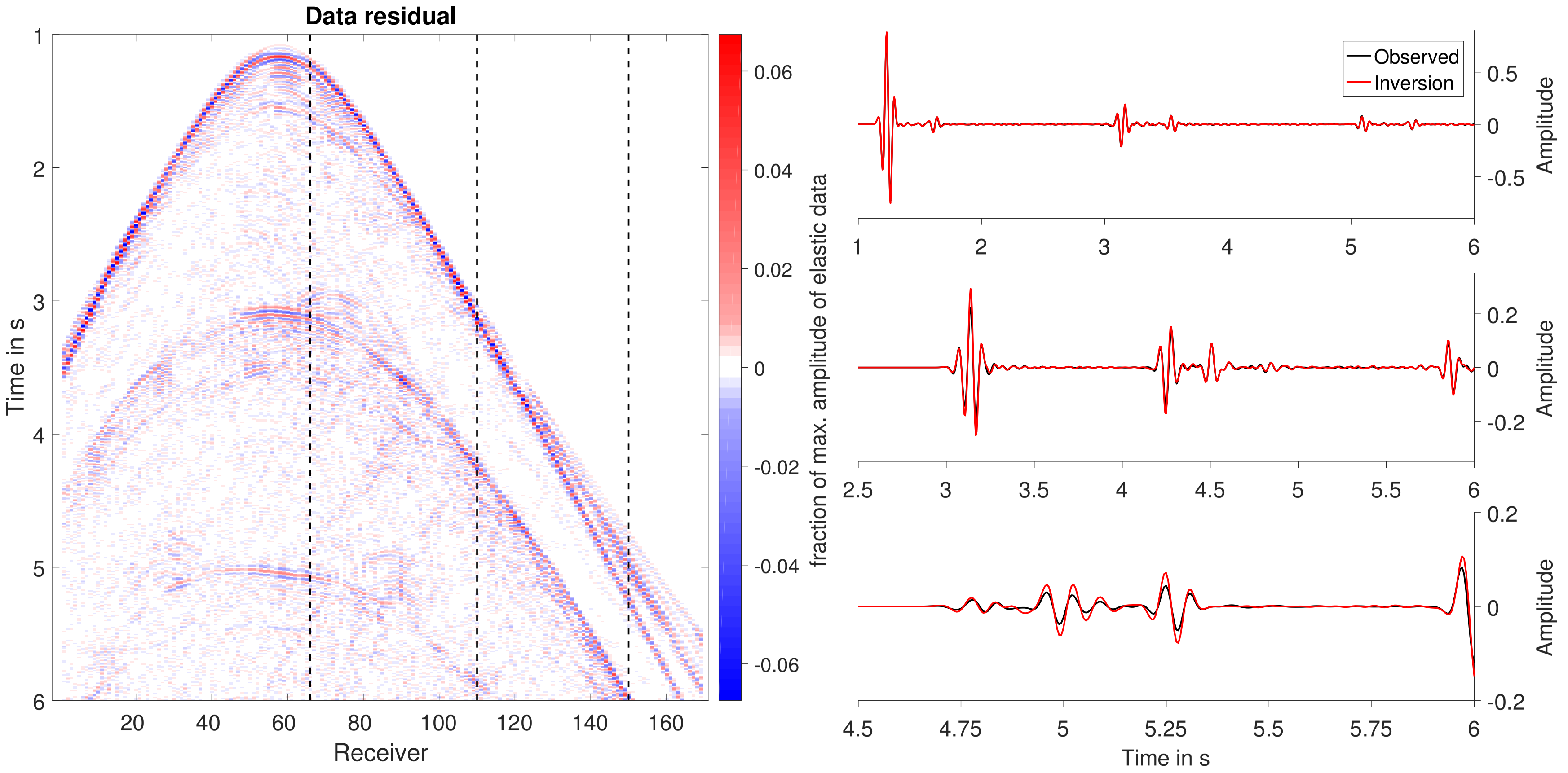

Figure 5.1.: Data residuals of the observed elastic data and the final synthetic data of the acoustic FWI reconstruction test are shown on the left. Illustrated on the right, is the comparison of observed and inverted data at the position of the dashed black lines.

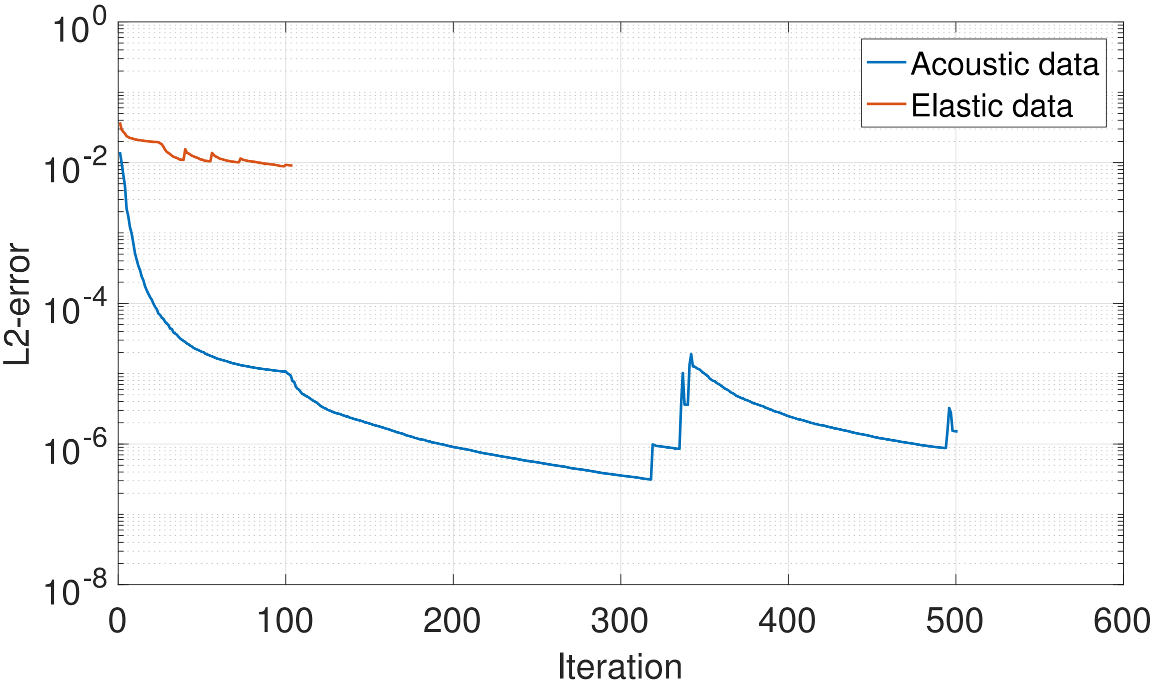

Figure 5.2.: Misfit evolution for the acoustic FWI reconstruction tests with acoustic and elastic observed data.

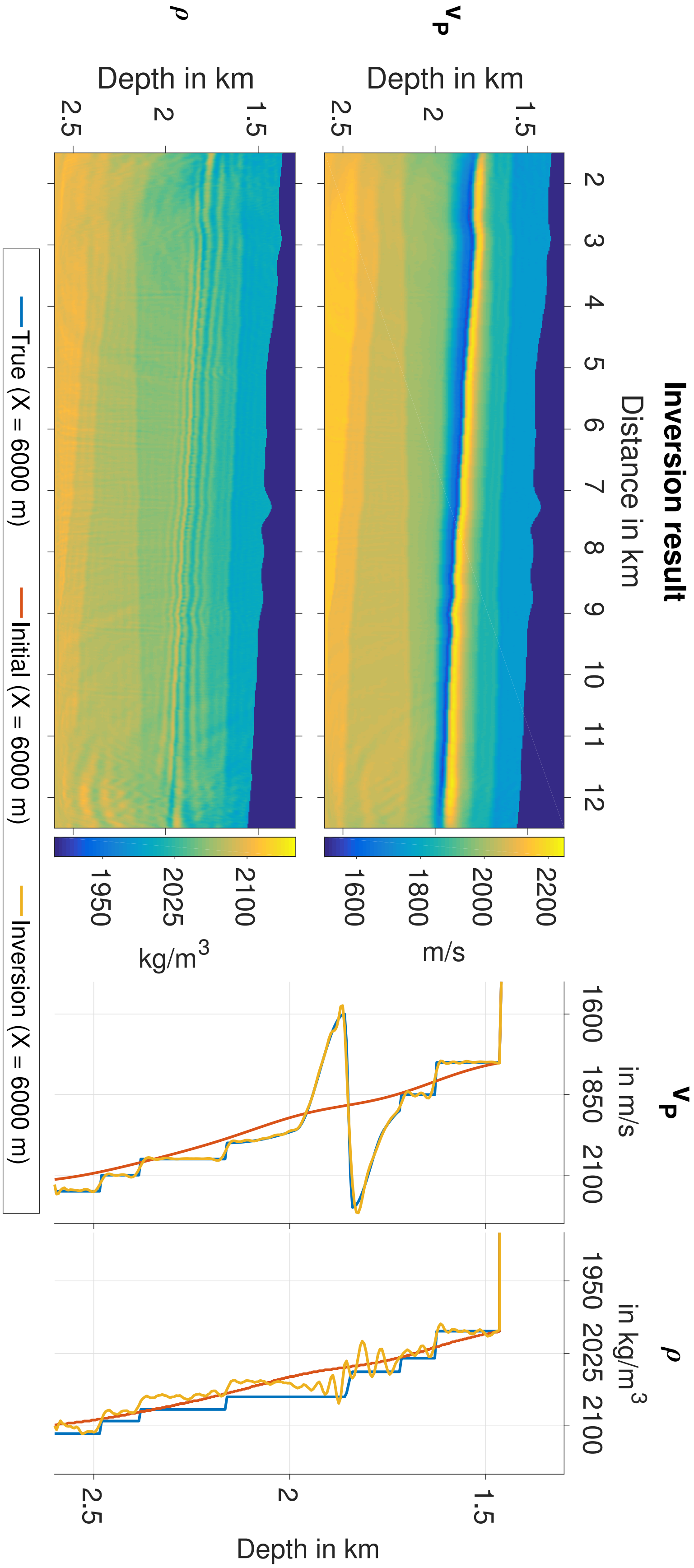

Figure 5.3.: Result of the acoustic FWI reconstruction test using acoustic forward modeled data. Left: 2D v_P and ρ inversion result; right: 1D cross sections at $X = 6$ km for the true, initial and inversion result model.

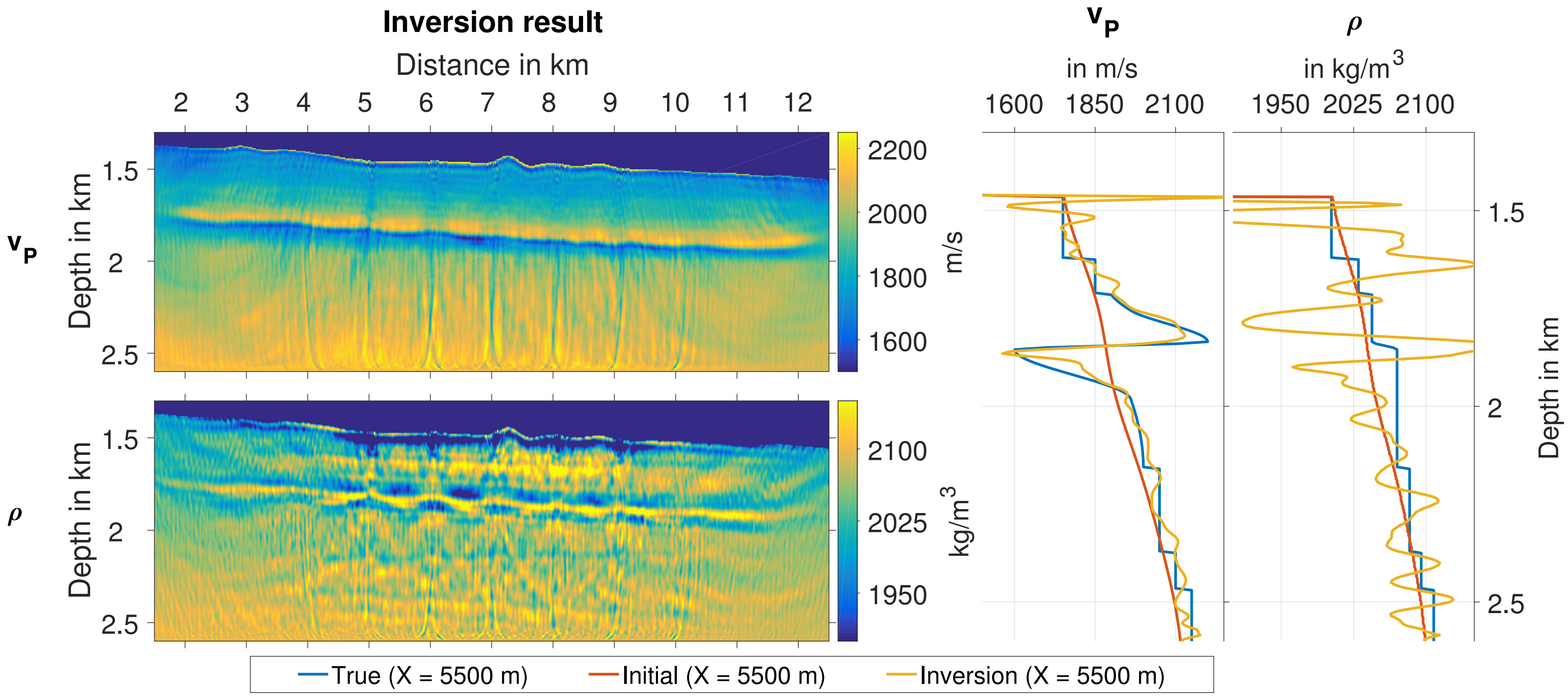

Figure 5.4.: Result of the acoustic FWI reconstruction test using elastic forward modeled data. Left: 2D v_P and ρ inversion result; right: 1D cross sections at $X = 5.5\,\mathrm{km}$ for the true, initial and inversion result model.

5.3. Elastic FWI

The ocean bottom seismometers (OBS) that are used in marine seismic surveys are oftentimes equipped with hydrophones to record pressure changes in the water column as well as a three-component seismometer to record the particle velocity on the seafloor. Therefore, we perform the elastic FWI reconstruction tests with pressure data and the horizontal and vertical component of the particle velocity data.

5.3.1. FWI of pressure data

The final 2D models of the inversion for all three parameters and cross-sections at 8.5 km are shown in figure 5.5 including the cross-sections of the true and initial models respectively. We were able to successfully reconstruct the gas hydrate and free gas bearing sediments using the elastic pressure data. Additionally, we have reconstructed all sedimentary interfaces including their absolute P- and S-wave velocity. Similar to the acoustic FWI of elastic data in the previous section, we can observe lateral inhomogeneities in the deeper parts of the model. However, they are significantly smaller than in the acoustic FWI. S-wave velocity does not suffer from these inhomogeneities. The final density model contains mainly fluctuations around the initial density model. These fluctuations are bigger than any present density contrast, hence it does not yield any qualitative information about the true density model. The sedimentary interfaces in the upper part of the model are vaguely discernible, but this is most likely in consequence of cross-talk from the v_P and v_S gradients.

As shown in figure 5.7, the misfit is smoothly reduced by 3 orders of magnitude with discrete increases of the misfit whenever the frequency content is increased throughout the workflow stages. Overall, the fit of the final synthetic seismograms is very accurate. Individual differences between the waveforms of the observed data and the synthetic data are negligible, as shown in figure 5.6.

5.3.2. FWI of particle velocity data

In this section, we consider the horizontal and vertical component of the partical velocity data as observed data for the elastic FWI reconstruction tests to ascertain if it has further benefits compared to using pressure data. We described the differences for the acquisition and the forward modeling setup between pressure and particle velocity data in the chapters 4.1.1 and 5.1.

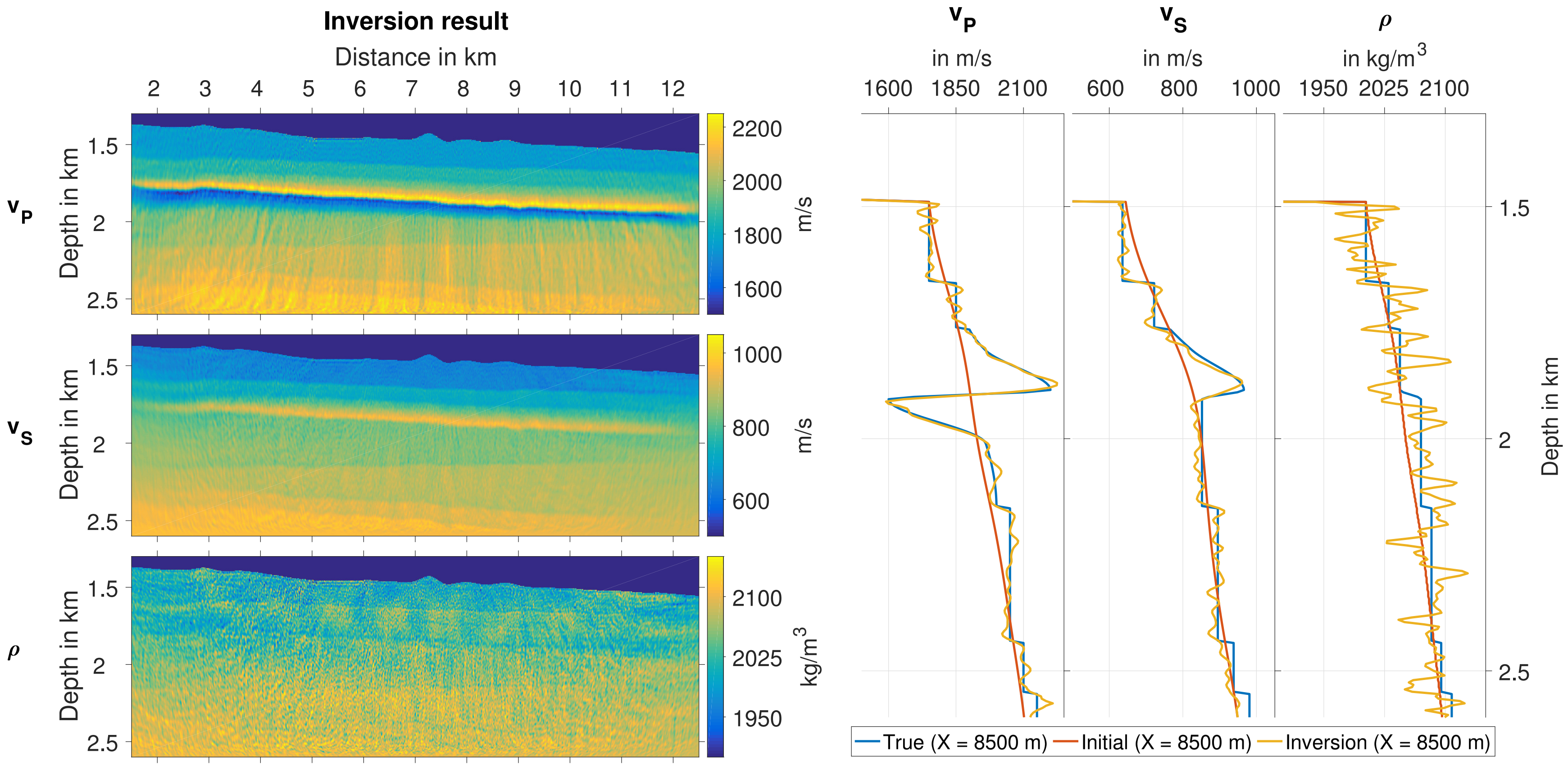

Figure 5.5.: Result of the elastic FWI reconstruction test using pressure data. Left: 2D v_P, v_S and ρ inversion results; right: 1D cross sections at $X = 8.5\,\mathrm{km}$ for the true, initial and inversion result model.

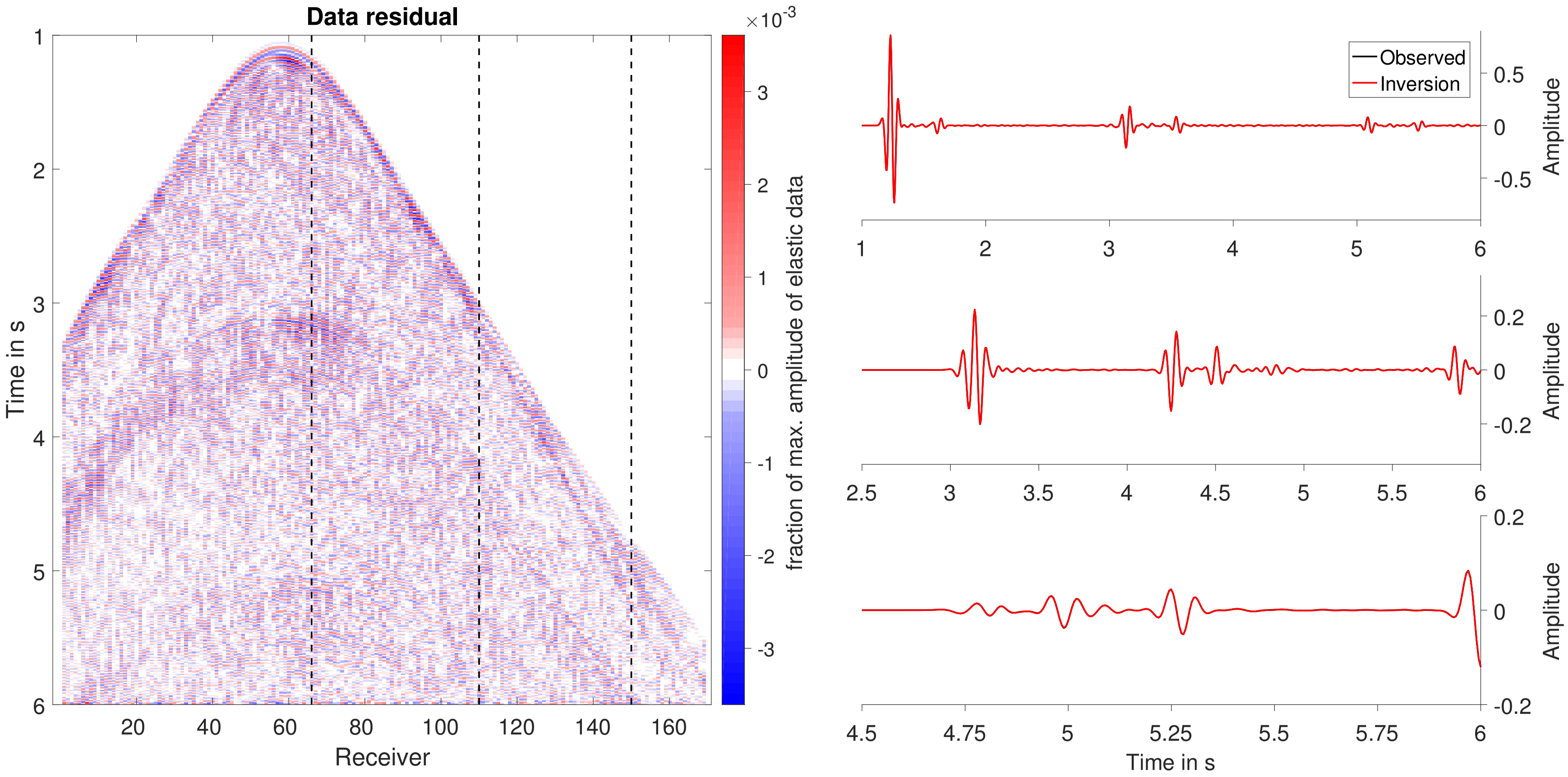

Figure 5.6.: Comparison of the observed pressure data and the synthetic data resulting from the final elastic FWI model at the location of the dashed black lines (right). The data residual at the last iteration is shown on the left as a fraction of the maximum amplitude of the observed data.

Horizontal component of the particle velocity

We were able to reconstruct the gas hydrate and free gas bearing sediment using the horizontal component of the particle velocity data, as shown in figures 5.8 and 5.9 (center column). The absolute values of the P- and S-wave velocity as well as the dimensions of the gas hydrate and free gas bearing sediment layers are accurately reconstructed with FWI. The lateral inhomogeneities in the deeper parts of the P-wave velocity model are partially bigger compared to the results of the pressure data. Nonetheless, the sedimentary interfaces can be inferred from the final inversion model. The inhomogeneities do not show in the S-wave velocity model. Yet again, the reconstruction of the density model failed.

Vertical component of the particle velocity data

The FWI with the vertical component of the particle velocity resulted in a less accurate subsurface model. Nonetheless, figure 5.8 (right column) shows that the gas hydrate and free gas bearing sediments are reconstructed adequately. The sedimentary interfaces are only reconstructed up to the base of the gas hydrate bearing sediment. In the deeper parts of the subsurface, the P-wave velocity is dominated by strong lateral inhomogeneities. Therefore, we cannot infer sedimentary interfaces. S-wave velocity resolution appears to be limited to a more narrow region than before (6 km to 9 km) and we observe stronger artifacts in the region between 3 km to 5 km. Figure 5.9 (right column) shows that the S-wave velocity of the gas hydrate bearing sediment is underestimated by our FWI approach. The quality of the final density model is dominated by considerably larger artifacts than before and cannot be used for any interpretation in regards to the subsurface model.

The inversion reduces the misfit adequately until it reaches the workflow stage with the highest frequency content, where the misfit only improves by one order of magnitude. For low frequencies, the misfit is reduced by two orders of magnitude (fig. 5.7).

An explanation for the lower quality of the inversion and the surplus of artifacts is most likely the accuracy of the spatial finite-difference operator we used during the forward modeling process. The reciprocal approach to marine acquisition requires the use of a unidirectional force as a seismic source. In case of the particle velocity data, the sources are located on the second grid point below the seafloor. In combination with the 8th order spatial operator, this leads to instabilities at the seafloor due to the relatively high contrast of water and sediment. Using a lower spatial accuracy and a smaller disceretization to keep the same frequency content fixes all of the problems that arise in comparison to the FWI with the horizontal component of the particle velocity and the pressure data. Therefore, the FWI of the vertical component of the particle velocity is not comparable with the others due to a systematic error in the setup of the reconstruction test.

Summary

In our synthetic experiment, we observe no additional benefits of using particle velocity data over pressure data to perform FWI. Nonetheless, the components of particle velocity data work equally well as an alternative if pressure data is not available. The resolution capabilities in regards to the reconstruction of gas hydrate and free gas bearing sediments is equivalent in all cases. The vertical component of the particle velocity data suffers from instabilities caused by the choice of the order of the spatial FD-operator. Using a second order FD-operator would have drastically increased the overall computation time of the FWI, which was too time consuming within the scope of this work. However, we were able to confirm that an inversion with the vertical component works as well as the inversion with the horizontal component when we put the source in greater depths, where the instabilities do not occur.

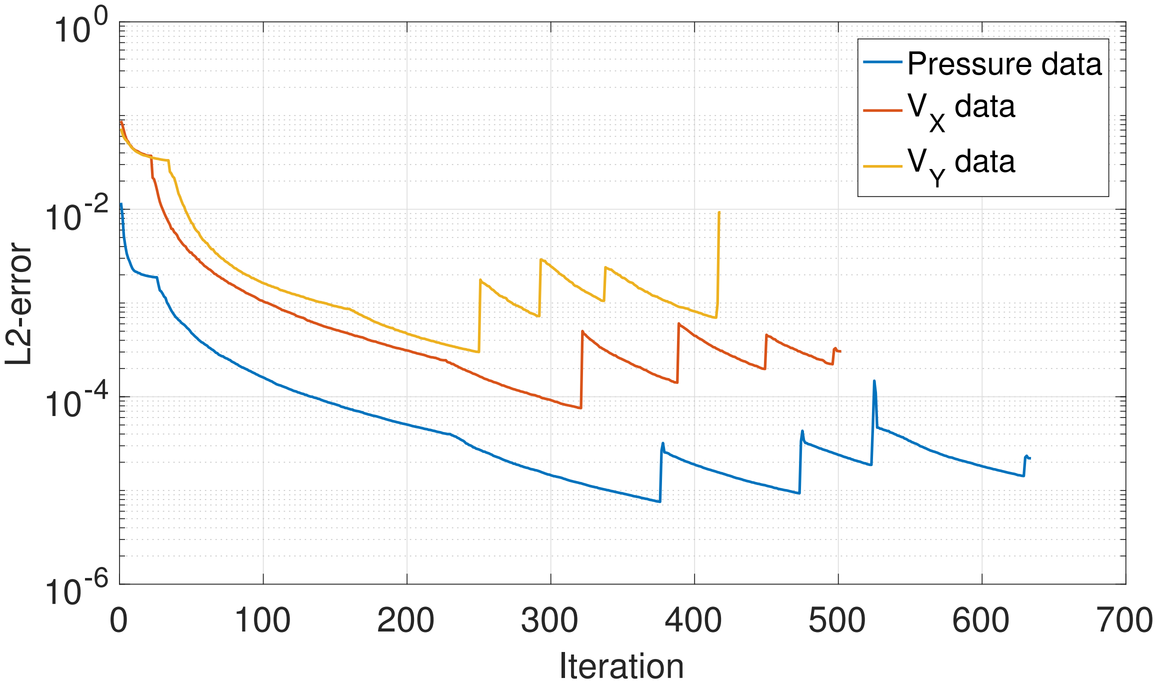

Figure 5.7.: Misfit evolution for the elastic FWI reconstruction tests with (pseudo-) observed data of the horizontal and vertical particle velocity as well as pressure.

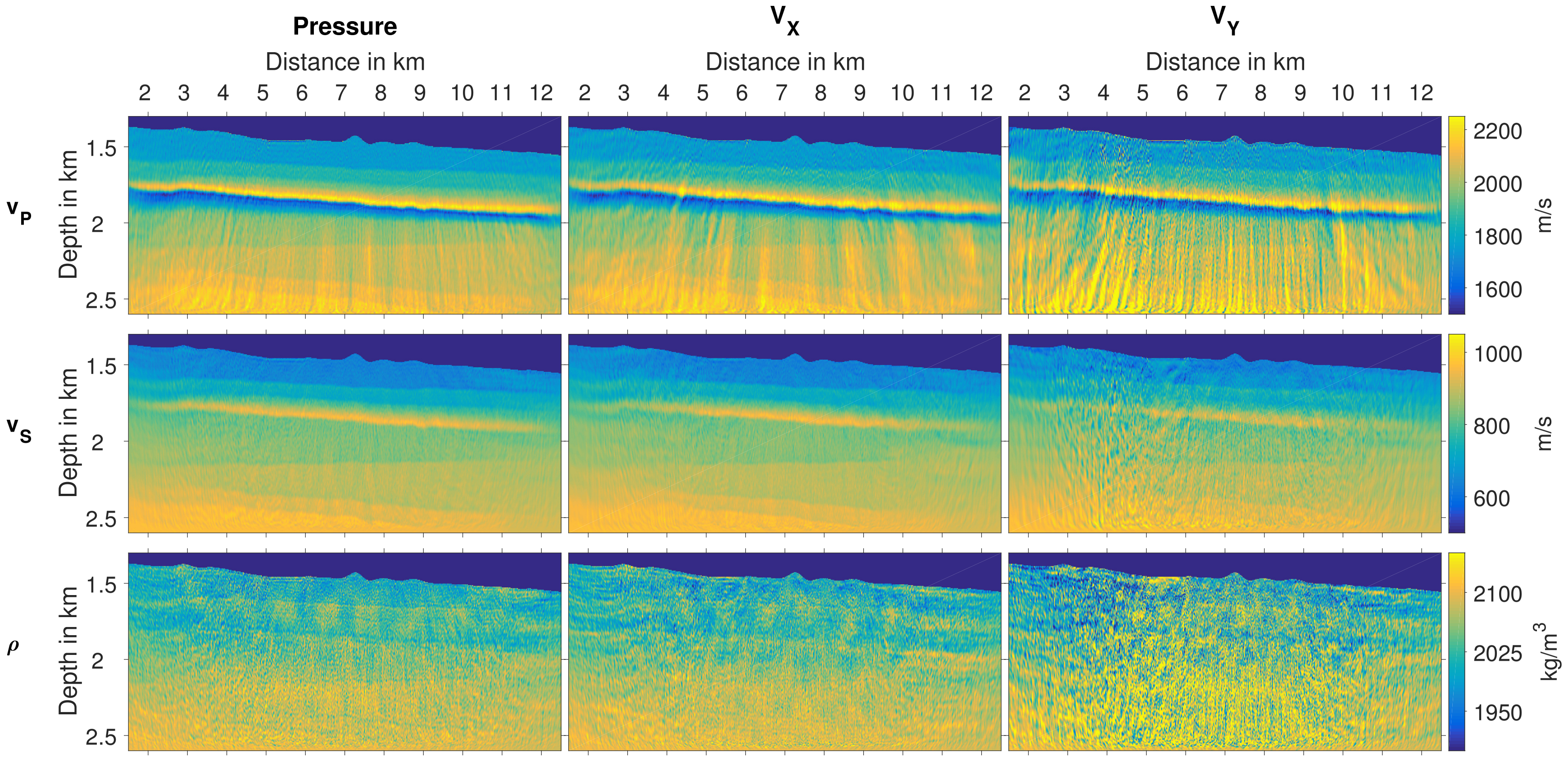

Figure 5.8.: Comparison of the elastic FWI results of the pressure data (left column), the horizontal component (center column) and the vertical component (right column) of the particle velocity data. Illustrated are the final FWI results of v_P (top row), v_S (middle row) and ρ (bottom row).

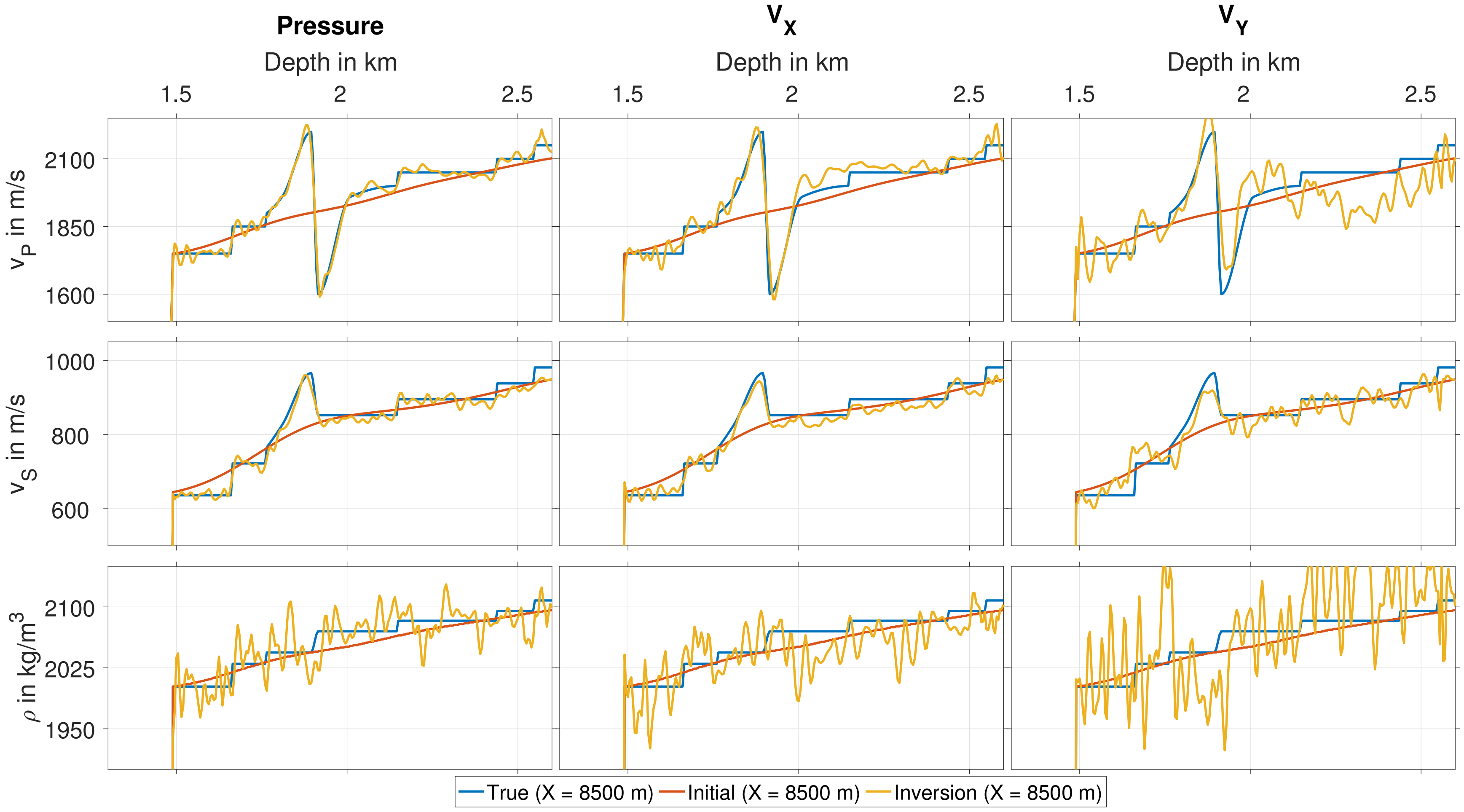

Figure 5.9.: Comparison of the elastic FWI results of the pressure data (left column), the horizontal component (center column) and the vertical component (right column) of the particle velocity data. Illustrated are the cross-sections of v_P (top row), v_S (middle row) and ρ (bottom row) at $X = 8500\,\mathrm{m}$.

5.4. FWI of noise contaminated data

Most of the time, field data acquisition is accompanied by unswayable circumstances, such as environmental noise or instrument failure. The finite-difference scheme we use to simulate synthetic data cannot account for these circumstances. Therefore, we add synthetic noise to the observed pressure data to perform a more realistic FWI reconstruction test.

We used the *suaddnoise* function of the open source seismic utility package Seismic Unix (Cohen and Stockwell Jr, 2001) to add band limited Gaussian white noise with a signal-to-noise ratio of $S/N = 8$ to our observed data. The bandwidth of the added noise ranges between 0 Hz and 80 Hz as shown in figure 5.12. As we can see in figure 5.10, the noise is more dominant than the reflections of the sedimentary interfaces and the refracted waves. This becomes more clear in figure 5.11, which shows a direct comparison of the noise contaminated and noise-free data.

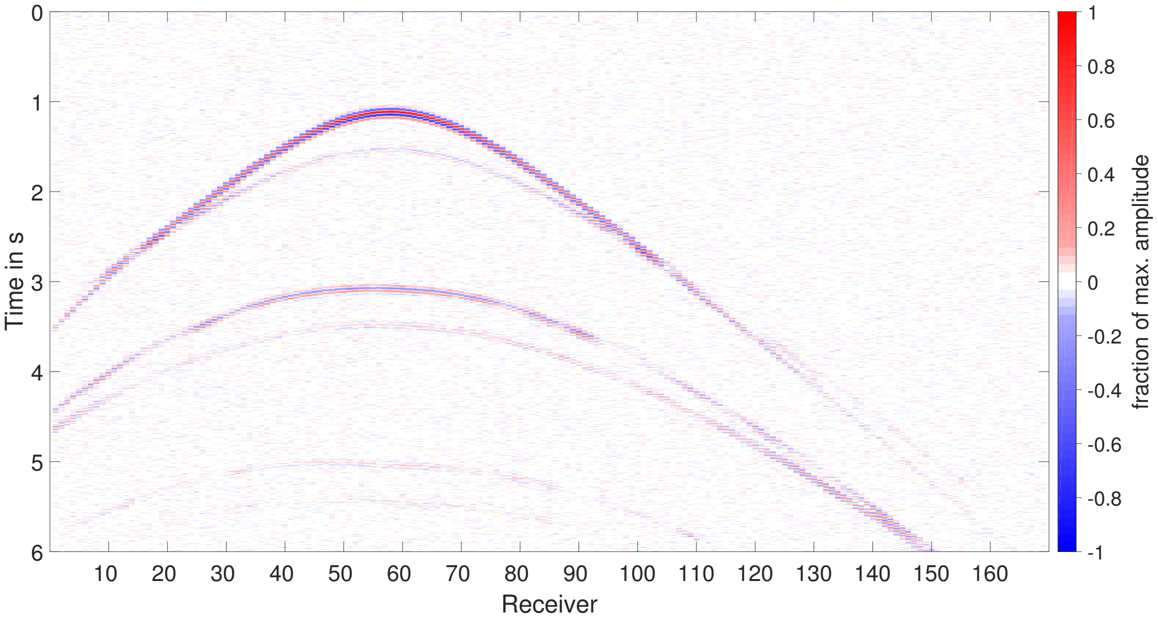

Figure 5.10.: Exemplary shot of the noise contaminated pressure data with a signal-to-noise ratio of $S/N = 8$.

Investigations during tests with the subsurface model in figure 4.4 show that the application of specific time windows during FWI does not significantly change its ability to reconstruct the properties of gas hydrate and free gas bearing sediments as shown in section A.5 in the appendix. We observed that S-wave resolution decreases slightly if we omit the information of refracted waves. Therefore, we only use a time-window to mute all signals before the first-arrivals. An example of elastic FWI and noise contaminated data using a more sophisticated time window is shown in the appendix in figure A.12. Furthermore, we adapted the workflow of the elastic FWI (tab. 5.2) by removing the stages with a 5 Hz low pass filter and added a 3 Hz high pass filter to all workflow stages. The reason for this is that the observed pressure data almost only contains noise when filtered with

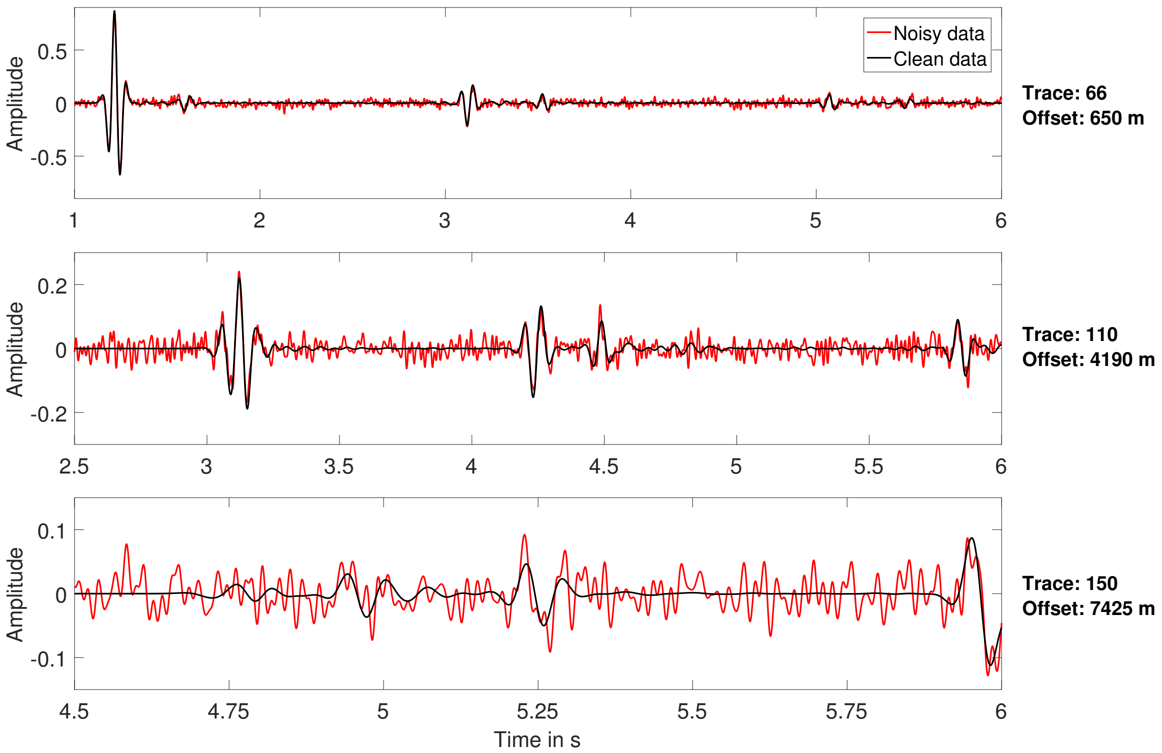

Figure 5.11.: Trace comparison for the near-, mid- and far offset region of the noise contaminated data and the noise-free data.

a 5 Hz low pass filter, thus leading to strong inversion artifacts during the 5 Hz workflow stages. The adapted workflow is shown in table 5.3

Table 5.3.: Multi-stage workflow for the elastic FWI with noise contaminated data.

Stage	Updates			Abort criterion in %	HP filter in Hz	LP filter in Hz
	v_P	v_S	ρ			
1	yes	no	no	1	3	10
2	yes	yes	no	1	3	10
3	yes	yes	yes	1	3	10
4	yes	yes	yes	1	3	15
5	yes	yes	yes	1	3	20
6	yes	yes	yes	1	3	25

The final model of the FWI is shown in figure 5.13. Although, we can observe an increased amount of artificial oscillations in the P-wave velocity due to noise, the gas hydrate and free gas bearing sediments were reconstructed well. However, the P-wave velocity of the hydrated sediment was underestimated by 50 m/s to 100 m/s. The sedimentary interfaces above the BSR are well defined, whereas the deeper part of the subsurface is dominated by fluctuations around the initial model.

Contrary to previous results, S-wave velocity was not reconstructed. The model only shows slight oscillations around the initial model. Further investigations show that the observed pressure data are most sensitive to v_S at frequencies around 5 Hz, where noise is the dominating signal. At higher frequencies, the initial S-wave velocity model is not accurate enough. Therefore, cycle skipping prevents the proper reconstruction of v_S. The density model is dominated by strong fluctuations, thus it cannot be evaluated.

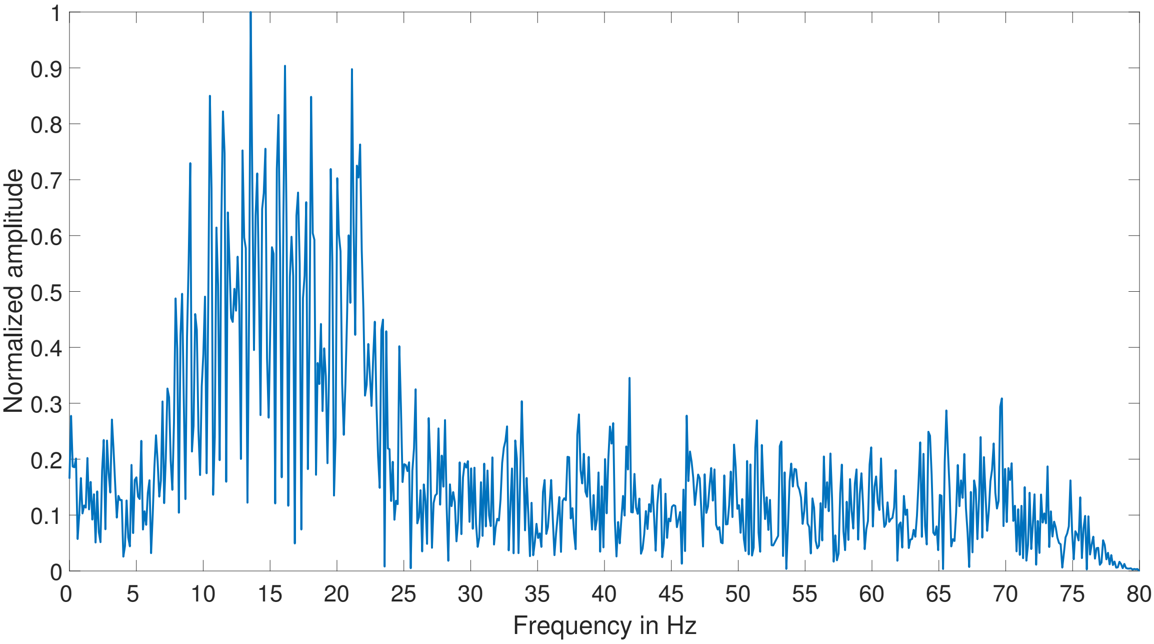

Figure 5.12.: Frequency content of the data shown in figure 5.10.

5.5. Case study: importance of initial model accuracy

In this case study, we investigate the influence of the initial model accuracy on the inversion. Previously, we used a smoothed version of the true models as initial models. This is similar to what we expect as a typical result from travel time tomography or other seismic imaging methods. However, the accuracy of these methods depends on data quality. For this reason, we vary the initial models to test, which accuracy is required to be able to reconstruct the P- and S-wave velocity characteristics of gas hydrate and free gas bearing sediments.

Test setting 1:
First, we assume the initial models shown in figure 4.4 to be the best initial models available. Next, we vary this model in ±2 % steps and keep the acquisition geometry and FWI settings identical to the previous reconstruction tests. Therefore, we change the overall kinematic information of the initial model and can asses the influence of inaccuracies in the initial model on the reconstruction ability of the inversion process. To be consistent

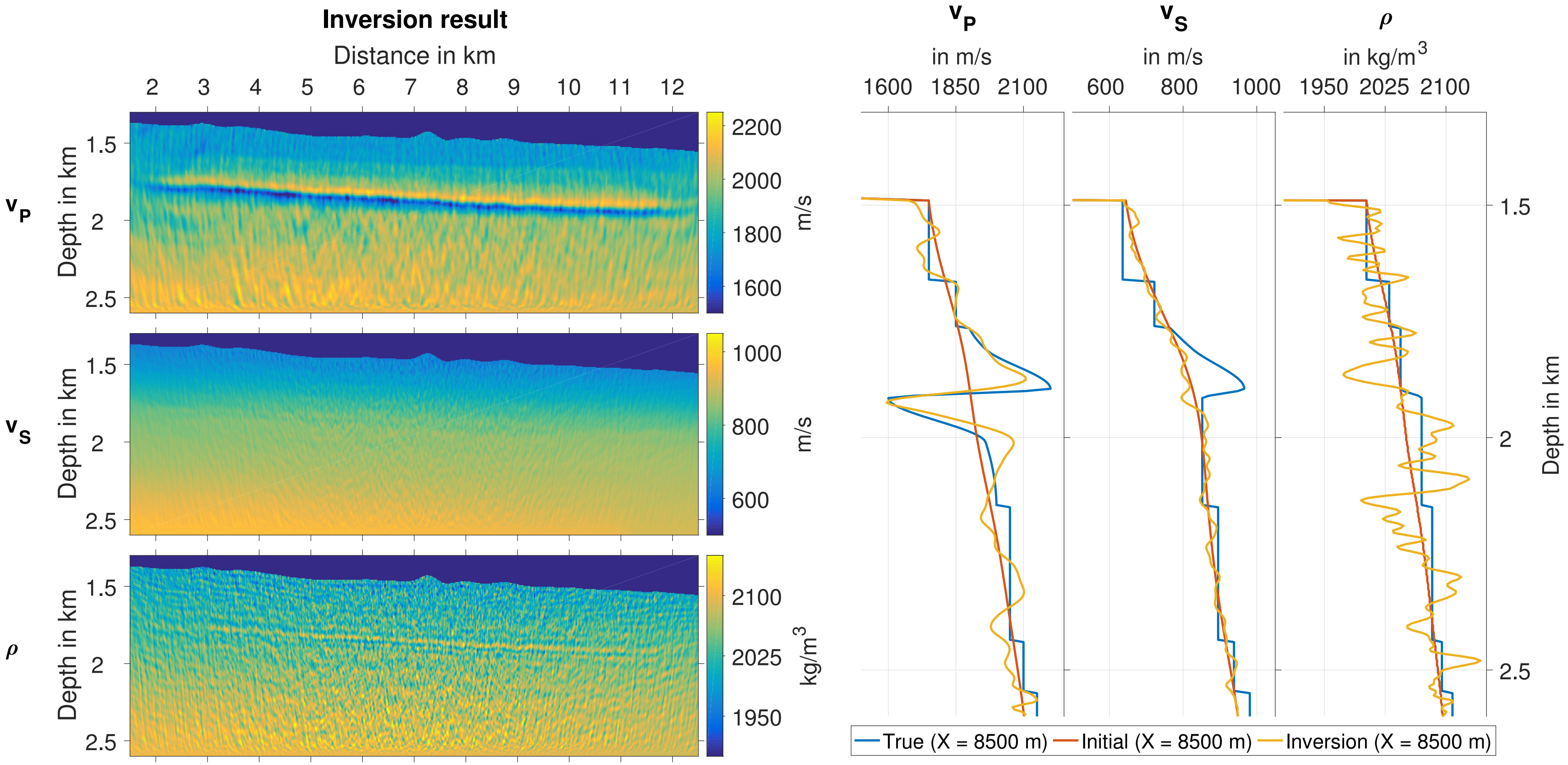

Figure 5.13.: Result of the elastic FWI reconstruction test using noise contaminated pressure data with a signal-to-noise ratio of $S/N = 8$. Left: 2D v_P, v_S and ρ inversion results; right: 1D cross sections at $X = 8.5\,\mathrm{km}$ for the true, initial and inversion result model.

with previous FWI, we only vary the initial model of v_P and v_S and calculate the density model using Gardner's relation (eq. 4.1).

The P-wave velocity characteristics of gas hydrate and free gas bearing sediment can be reconstructed by elastic FWI in the range of -10 % to +10 % of what is considered the optimal initial model as shown in figures 5.14 and 5.15. Furthermore, the sedimentary interfaces above the BSR are resolved in both cases. Deeper parts of the P-wave velocity model begin to suffer from strong lateral inhomogeneities with notably less variation of the initial model (±4 %). The same applies to the S-wave velocity model. The gas hydrate bearing sediment is detectable up to a variation of ±4 % of the initial model. However, the absolute values are consistently over- or underestimated respectively, making the evaluation of the model in regards to gas hydrates difficult. The density model cannot be evaluated in any of the performed reconstruction tests due to strong inversion artifacts. The remaining results are shown in section A.4 in the appendix.

Test setting 2:
In the previous test, we observed that the reconstruction of the S-wave velocity suffers more significant from a less accurate initial model. Additionally, the amount of artifacts, especially the lateral inhomogeneities in the deeper part of the P-wave velocity model, increase in a similar manner. Therefore, we change the initial S-wave velocity model individually to test if a correlation between the inhomogeneities and the accuracy of the initial S-wave velocity exists. We create the new initial S-wave velocity model by using a Gaussian window (eq. 4.2) with $\alpha = 50$ instead of $\alpha = 100$ to smooth the true model. This way, we use a more accurate kinematic model than before. The acquisition geometry, FWI setup and initial models for the P-wave velocity and density remain unchanged.

The reconstruction test shows that the lateral inhomogeneities are far less notable in the P-wave velocity model. Additionally, the overall resolution of the reflection interfaces is considerably sharper than before and small scale oscillations throughout the model decreased as shown in the cross-sections in figure 5.16. Another important improvement is that the sedimentary interfaces are now depicted in the density model and it shows less fluctuations compared to the reconstruction test in figure 5.5.

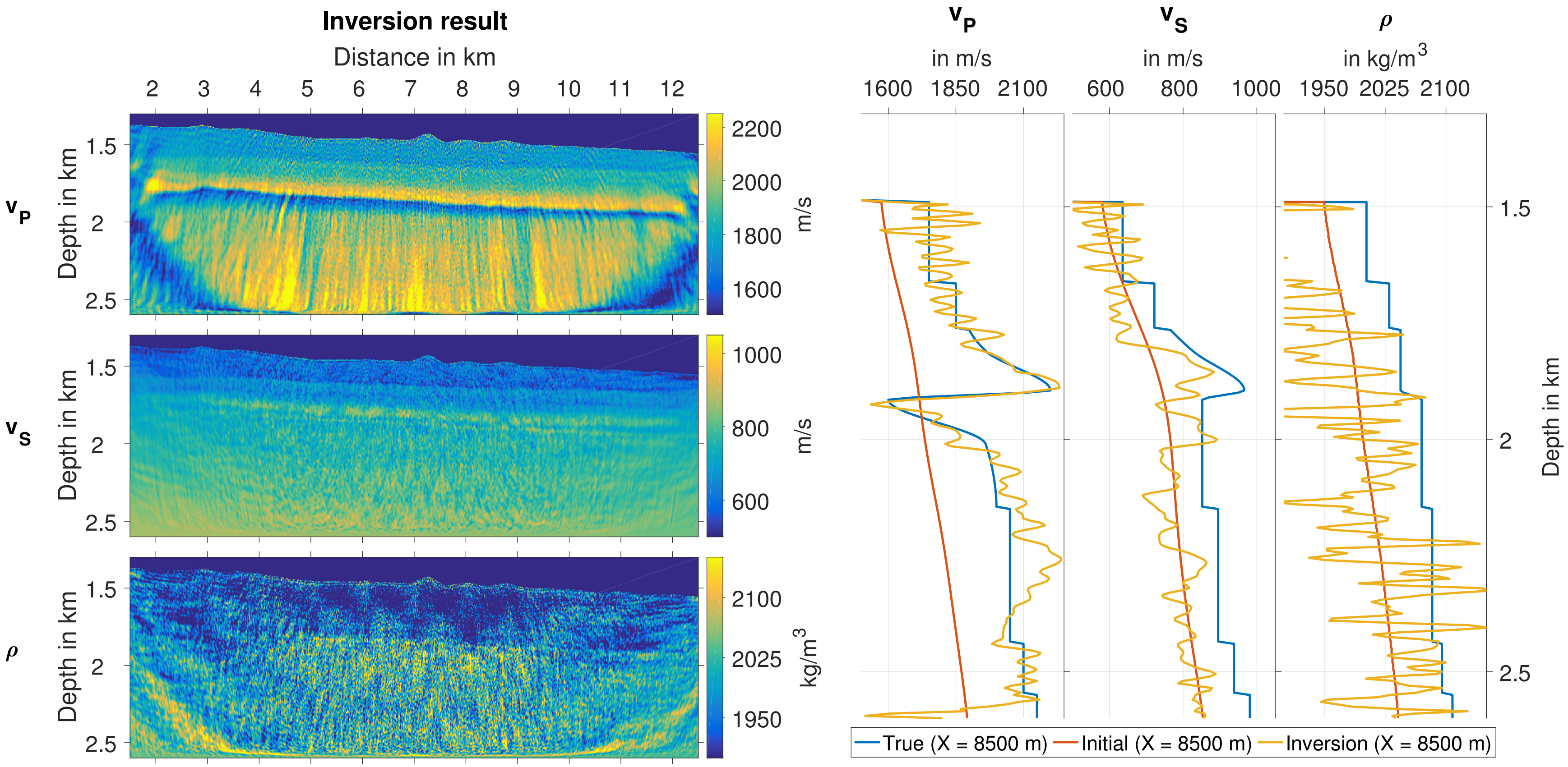

Figure 5.14.: Result of the elastic FWI reconstruction test using initial models of v_P, v_S and ρ with a variation of $-10\,\%$. Left: 2D v_P, v_S and ρ inversion results; right: 1D cross sections at $X = 8.5\,\mathrm{km}$ for the true, initial and inversion result model.

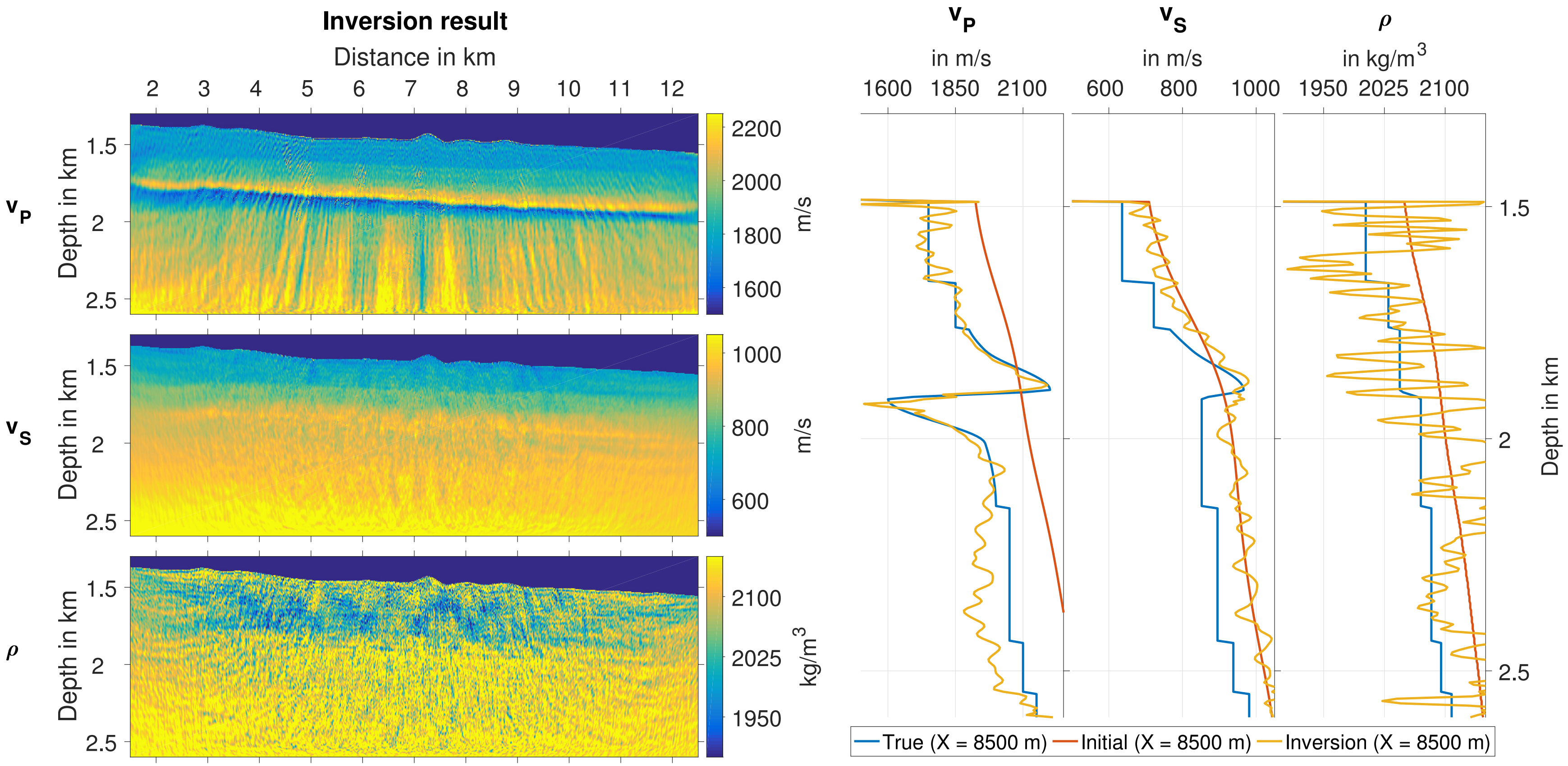

Figure 5.15.: Result of the elastic FWI reconstruction test using initial models of v_P, v_S and ρ with a variation of +10 %. Left: 2D v_P, v_S and ρ inversion results; right: 1D cross sections at $X = 8.5$ km for the true, initial and inversion result model.

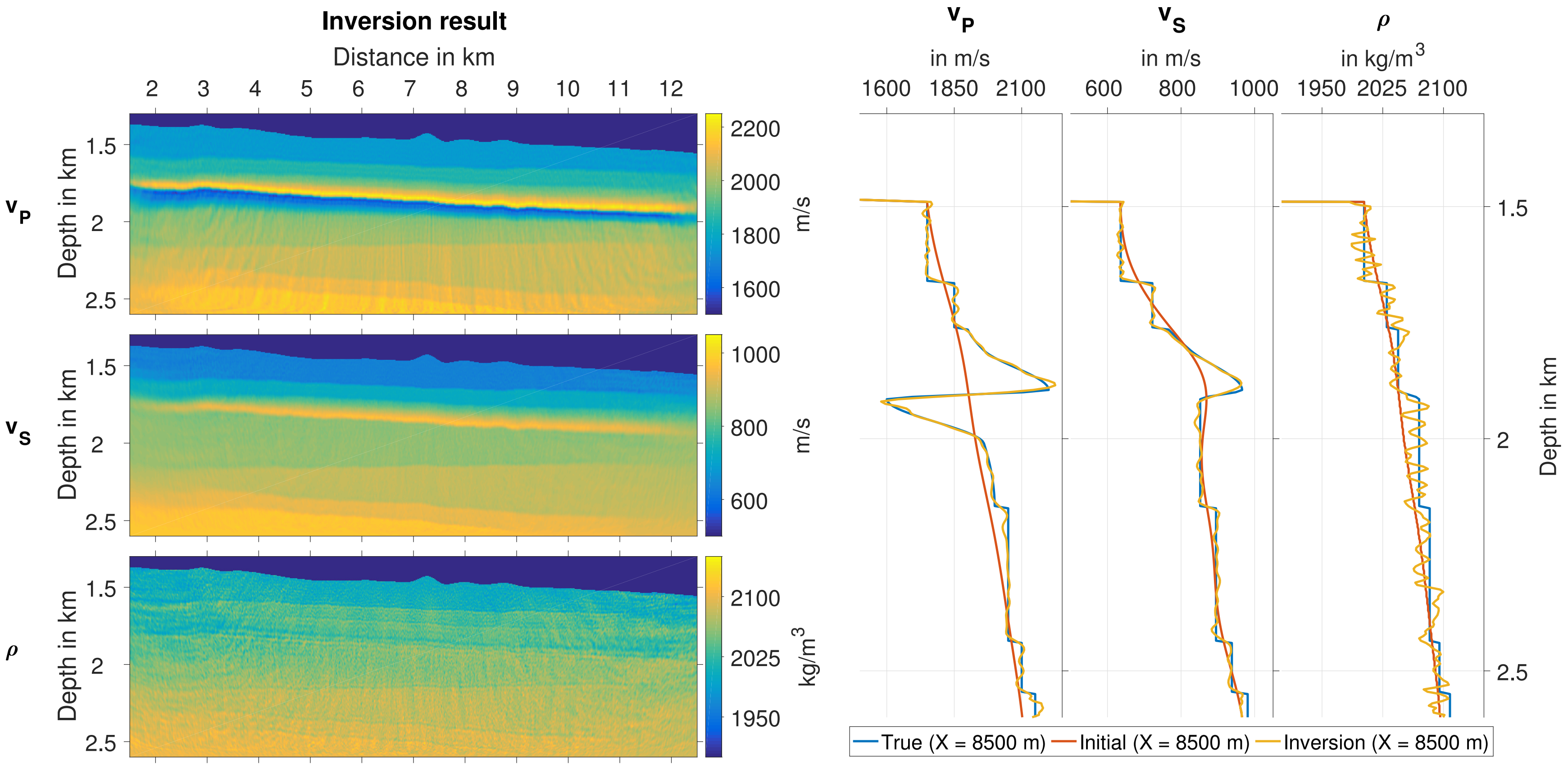

Figure 5.16.: Result of the elastic FWI reconstruction test using an improved initial model for v_S. Left: 2D v_P, v_S and ρ inversion results; right: 1D cross sections at $X = 8.5$ km for the true, initial and inversion result model.

5.6. Summary

We performed acoustic and elastic 2D full-waveform inversion reconstruction tests on acoustic and elastic observed pressure data as well as on the horizontal and vertical component of observed particle velocity data. Moreover, we discussed the application of a multi-stage workflow and the parameter setup for the inversion.

The application of acoustic FWI on elastic pressure data introduced three distinguishable inversion artifacts. Two of them are located in the first few meters below the seafloor. Circular artifacts appear around the source locations and heavily elevated P-wave velocities dominate the first grid points of the uppermost sediments. Additionally, the deeper part of the subsurface is characterized by strong lateral inhomogeneities. Nonetheless, the gas hydrate and free gas bearing sediments were reconstructed. However, the absolute P-wave velocity values in the gas hydrate bearing zone were underestimated by up to 150 m/s. General resolution of the sedimentary interfaces was lost in comparison to the FWI results with acoustic observed pressure data due to the superimposed artifacts.

The gas hydrate and free gas bearing sediments were fully reconstructed using elastic FWI, except when we applied it to the vertical component of the observed particle velocity data. There, we reconstructed the localization of the gas hydrate layer but underestimated the absolute S-wave velocity values. However, this is more likely the result of instabilities at the water-seafloor interface due to the choice of the spatial accuracy of the finite-difference operator. Fluctuations in the density model were generally too dominant to make an interpretation possible.

When we performed an elastic FWI with relatively strong noise levels for marine seismics, we observed that the characteristic P-wave velocity of gas hydrate and free gas bearing sediment could be reconstructed very well. However, we did not have any resolution capability in the S-wave velocity and density model.

A reoccurring problem was observed using acoustic and elastic FWI with elastic forward modeled data: artificial, lateral inhomogeneities superimposed mainly the P-wave velocity model in a depth of 1.75 km to 2.6 km, which, in some situations, made the observation of the sedimentary interfaces difficult. These inhomogeneities are connected to the accuracy of the initial S-wave velocity model, which is supported by the fact that they are stronger with acoustic FWI, since it does not use S-wave velocity information. Additionally, we carried out a case study with a more accurate initial v_S model and observed almost no lateral inhomogeneities. Further testing showed that P-wave velocity characteristics of gas hydrate and free gas bearing sediment were reconstructed with initial model inaccuracies of up to ±10 %, whereas S-wave velocity resolution deteriorated at inaccuracies of ±4 % and above.

6. Discussion & conclusion

In this thesis, we conducted acoustic and elastic 2D full-waveform inversion reconstruction tests of submarine gas hydrate models. Based on data of a seismic survey in the northwestern part of the Black Sea, we created a 2D subsurface model containing a layer of gas hydrate and free gas bearing sediment respectively. Subsequently, we evaluated the performance of acoustic and elastic 2D FWI with pressure and particle velocity data and investigated the impact of different initial models on the inversion result.

6.1. Discussion

Acoustic FWI proved to be a very efficient method to obtain a first estimate of the subsurface, especially in marine environments. In comparison to elastic FWI, acoustic FWI only required 1/10th of the computation time (tab. A.3) to converge and P-wave velocity is less sensitive to inaccuracies of the initial model, which makes acoustic FWI optimal for the initial testing phase. Despite using a marine acquisition geometry, we observed considerable differences between acoustic and elastic observed data caused by converted waves (ch. 4.2.2). These differences are compensated for by inversion artifacts, which make the observation of sedimentary interfaces difficult. Nevertheless, we were able to reveal the gas hydrate and free gas bearing sediment layers. However, at some locations the P-wave velocity of the hydrated sediment was underestimated by up to 150 m/s.
Therefore, it is suggested to use elastic FWI to study the parameters of hydrated marine sediments. We observed significantly less inversion artifacts and fully reconstructed the P- and S-wave velocity of the gas hydrate and free gas bearing sediments as shown in figure 5.5. Additionally, the elastic FWI revealed the remaining sedimentary interfaces and resulted in the most accurate subsurface model. The density model is dominated by big fluctuations, which makes an interpretation impossible. We observed that an inversion using particle velocity data yielded no additional benefit over the use of pressure data. If anything, it is more prone to errors due to the more complicated reciprocal relationship (app. A.2) and the instabilities at higher orders of the spatial finite-difference operator (cha. 5.3.2).
Finally, we performed a case study to investigate the consequences of inaccurate initial models. We observed that S-wave velocity is much more sensitive to inaccurate initial models or bad data quality than P-wave velocity. Likewise, a better initial v_S model decreased the amount of artifacts in the P-wave velocity even further as shown in figure

5.16. Additionally, it improved the resolution of density to a point, where we are able to reconstruct density contrasts in the subsurface. On the other hand, an inaccurate initial model or increased levels of noise lead to a complete loss of S-wave resolution as shown in figures 5.13, 5.14 and 5.15.

6.2. Conclusion

The acoustic and elastic 2D FWI were both able to reconstruct the P-wave velocity characteristics of gas hydrate and free gas bearing sediment in a marine environment. However, for improved resolution and the least amount of inversion artifacts, it is necessary to use elastic FWI. The reconstruction of S-wave velocity features of gas hydrate and free gas bearing sediments is heavily dependent on data quality and initial model accuracy. In this study, the inversion of particle velocity data yielded no further benefits compared to the inversion of pressure data.

6.3. Recommendations

We demonstrated that full-waveform inversion is the go-to method to study the velocity structure of a BSR. P- and S-wave velocity were properly reconstructed using elastic FWI. Nevertheless, we recommend to perform reconstruction tests with more complex hydrate formations to accentuate these results even further. Additionally, further investigations should include the FWI with viscoelastic forward modeling, especially while using field data. Guerin and Goldberg (2002) show that hydrate bearing zones have significant attenuation at seismic frequencies of 10 to 200 Hz with Q-values of around 10. Hence, not including attenuation into the FWI process can lead to a misinterpretation of the BSR signal amplitude and introduces measurable errors to the quantification of gas hydrate.

List of Figures

List of Tables

A. Appendix

A.1. Forward modeling and inversion parameters

Table A.1.: Setup of the finite-difference forward modeling scheme.

Modeling parameter:	
Model size	2880 × 520 grid points
Spatial discretization	5.0 m
Temporal discretization	5.0×10^{-4} s
Recording time	6.0 s
Spatial FD order	8th
C-PML boundary width	30 grid points
C-PML reference velocity	2150 m/s
C-PML reference frequency	10 Hz
Free surface	mirroring technique

Table A.2.: Setup of the full-waveform inversion.

Inversion parameter:	
Min. number of iterations per stage	3
Frequency filter	4th order Butterworth
Frequency steps	5 Hz
Frequency bandwidth	up to 25 Hz
Circular logarithmic source taper	125 m
Lower limit $v_\mathrm{P}/v_\mathrm{S}$-ratio	1.2
Min/max v_P	1484/2500 m/s
Min/max v_S	0/1250 m/s
Min/max ρ	1020/2200 kg/m^3
Hessian water level	0.005
Historic L-BFGS information	10
Wolfe condition c_1	0.0
Wolfe condition c_2	0.9

A.2. Validation of reciprocity

Aki and Richards (2002) show that the displacement field u_i of a body force f_i, which is applied impulsively in the n-direction to a given particle at $x = \xi$ and $t = \tau$ is represented by the elastodynamic Green's function $G_{in}(\mathbf{x}, t; \xi, \tau)$. This Green function is a second order tensor and depends on both receiver and source coordinates respectively. If we state boundary conditions we can specify the Green's function G uniquely. In the case of homogeneous boundary conditions, i.e. the free surface boundary condition (chapter 2.2.3), we obtain an important reciprocal relationship for source and receiver coordinates:

$$G_{nm}(\xi_2, \tau_2; \xi_1, \tau_1) = G_{mn}(\xi_1, -\tau_1; \xi_2, -\tau_2) \ . \tag{A.1}$$

Equation (A.1) signifies that a body force f applied in the m-direction at $x = \xi_1$ and $t = \tau_1$ generates a displacement field, which is equal to a displacement field generated by a body force g in n-direction at $x = \xi_2$ and $t = -\tau_2$, if $\tau_1 = \tau_2 = \tau = 0$.
In the case of an explosive source and hydrophones, we can exchange source and receiver positions without further ado, since the emitted wave field is recorded as the same physical parameter as the generated wave field , i.e. pressure. However, if we use an explosive source in conjunction with a three component geophone that records the particle velocity, we have to generate the wave field with a unidirectional force and record it with hydrophones in the reciprocal state. Additionally, we have to differentiate the data and adjust the amplitude with a constant k to yield the same results. Figure A.1 shows the results of the forward modeling test run to validate that the finite-difference scheme satisfies the reciprocity relationship. For the pressure data, we placed the instruments in the water column, whereas one of the instruments is placed in the sediments for the particle velocity data. In both cases, the reciprocal acquisition geometry yields identical results.

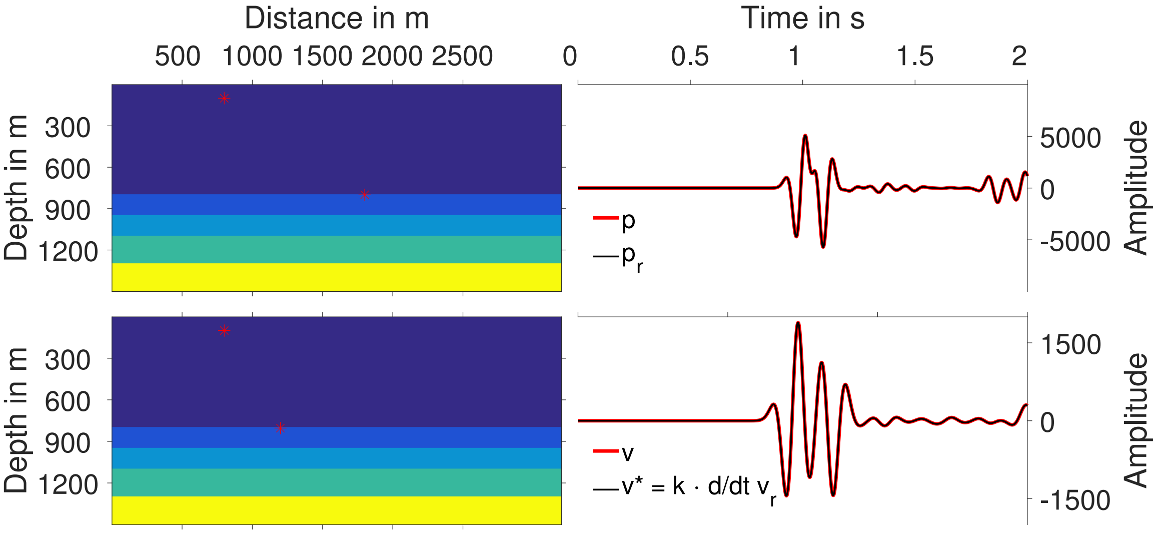

Figure A.1.: Validation of space-time reciprocity. Top: reciprocity applied to pressure data; bottom: reciprocity applied to particle velocity data.

A.3. Computational resources

All calculations were carried out on the InstitutsCluster II (IC2), which is funded by the German Research Foundation (`http://www.dfg.de`) and purchased by different institutes of the Karlsruhe Institute of Technology (KIT). IC2 is maintained and supported by the Steinbuch Centre for Computing (SCC). The computational "thin" nodes of IC2 use two octa-core Intel Xeon E5-2670 processors (Sandy Bridge) with a base frequency of 2.6 GHz, 64 GB memory and 2x1 TB local storage space. Table A.3 lists the number of processors, as well as the required computation time and number of iterations for each inversion conducted during this thesis.

Table A.3.: Computational resources required for the inversions presented in chapter 5.

Inversion	Number of cores	Computation time	Iterations	Figure #
Acoustic (ac. data)	400	485 min 0.3 s	502	5.3
Acoustic (el. data)	400	107 min 28.6 s	105	5.4
Elastic (P data)	400	1102 min 25.5 s	635	5.5
Elastic (V^{X} data)	400	883 min 22.4 s	500	5.8
Elastic (V^{Y} data)	400	869 min 17.8 s	419	5.8
Noisy data	400	74 min 13 s	26	5.13
-10% initial model	400	1152 min 35 s	655	5.14
+10% initial model	400	883 min 17.9 s	506	5.15
Improved v_{S} model	400	1328 min 16.4 s	713	5.16

A.4. Case study: remaining results

In this section, we present the remaining results of the case study carried out in chapter 5.5. Figures A.2, A.4, A.6 and A.8 show the FWI results with −2 %, −4 %, −6 % and −8 % variation of what is assumed to be the optimal initial model respectively. Additionally, figures A.3, A.5, A.7 and A.9 show the FWI results with +2 %, +4 %, +6 % and +8 % variation.

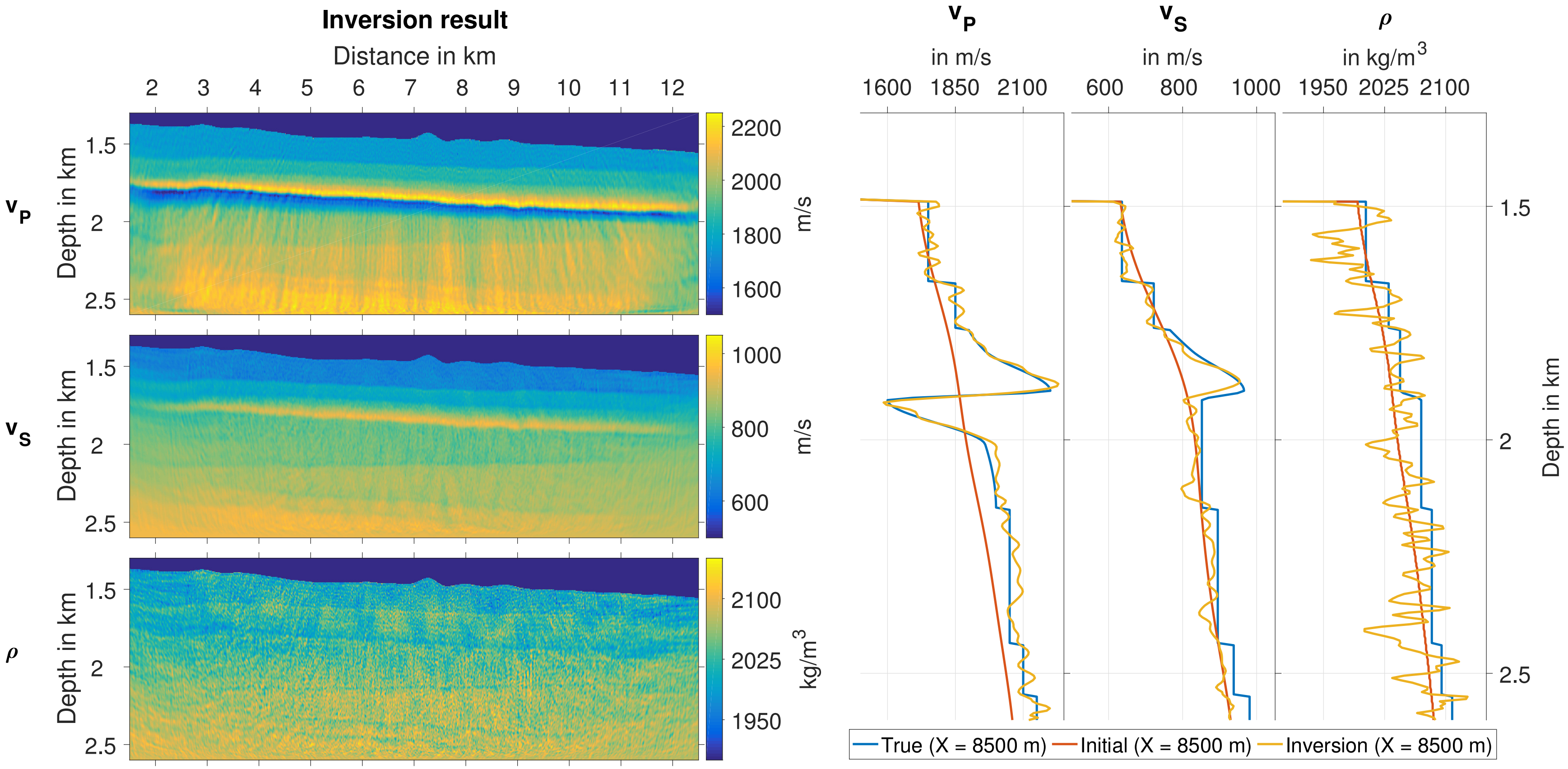

Figure A.2.: Result of the elastic FWI reconstruction test using initial models of v_P, v_S and ρ with a variation of $-2\,\%$. Left: 2D v_P, v_S and ρ inversion results; right: 1D cross sections at $X = 8.5\,\mathrm{km}$ for the true, initial and inversion result model.

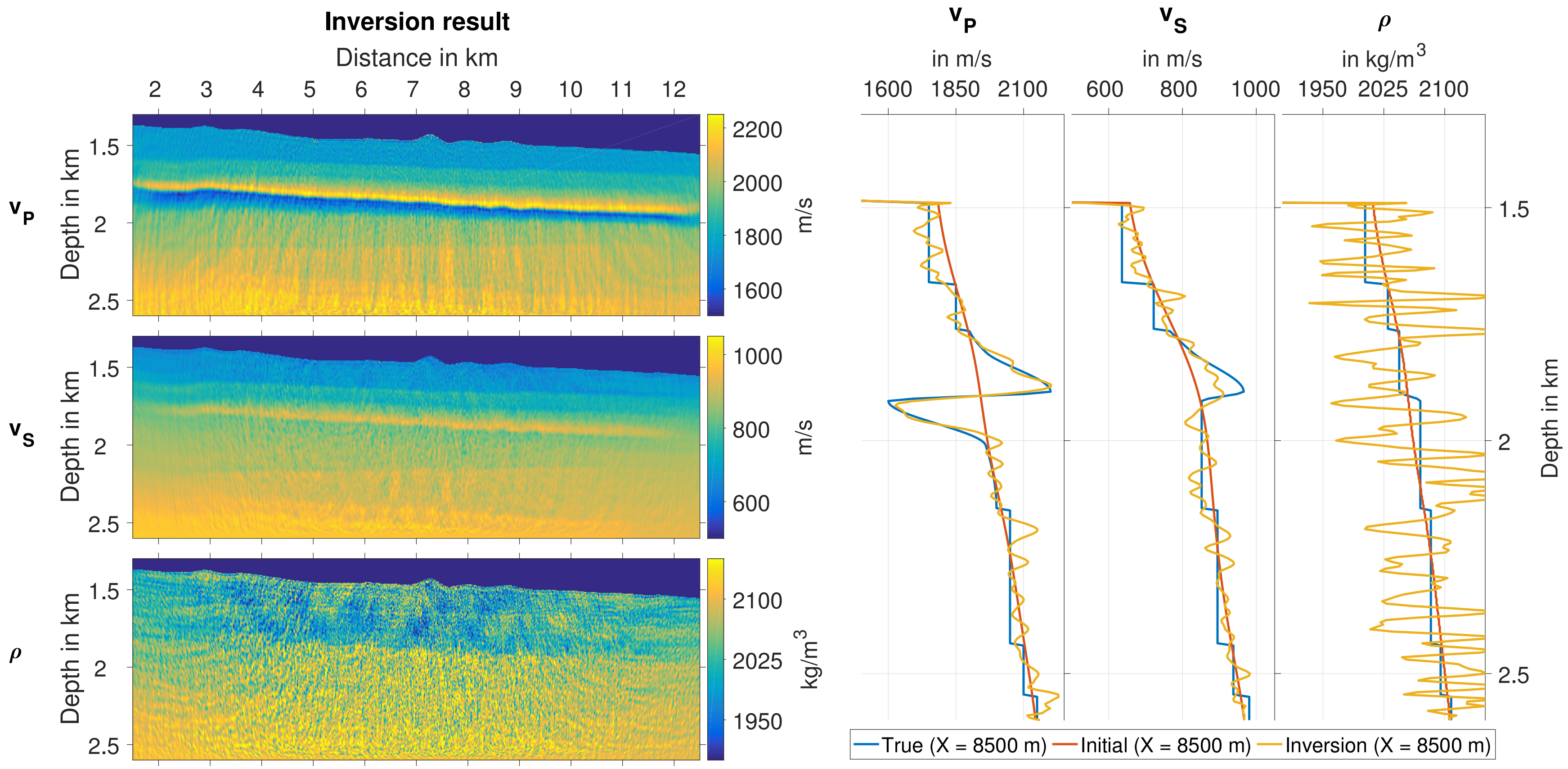

Figure A.3.: Result of the elastic FWI reconstruction test using initial models of v_P, v_S and ρ with a variation of +2%. Left: 2D v_P, v_S and ρ inversion results; right: 1D cross sections at $X = 8.5$ km for the true, initial and inversion result model.

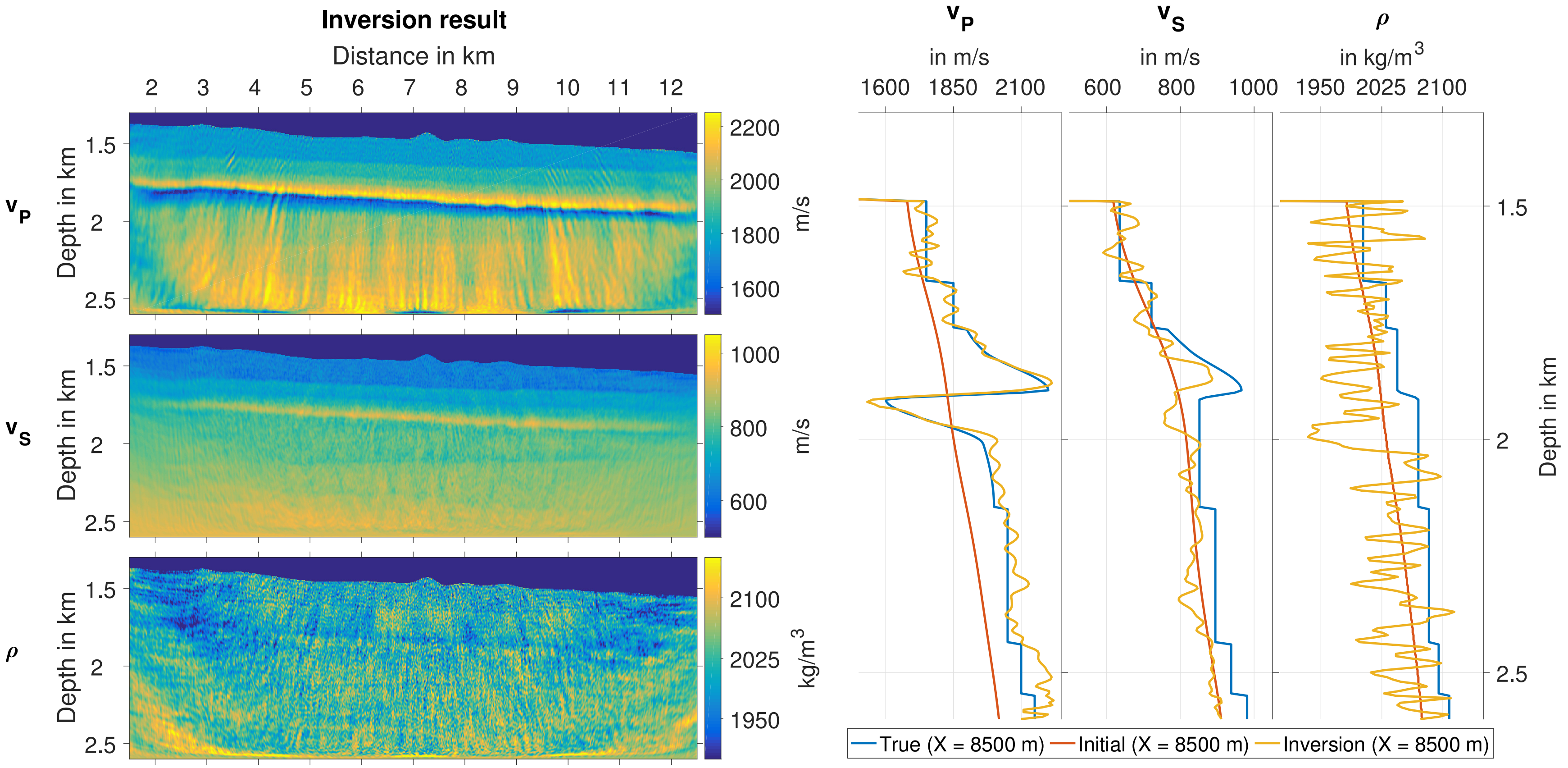

Figure A.4.: Result of the elastic FWI reconstruction test using initial models of v_P, v_S and ρ with a variation of -4%. Left: 2D v_P, v_S and ρ inversion results; right: 1D cross sections at $X = 8.5$ km for the true, initial and inversion result model.

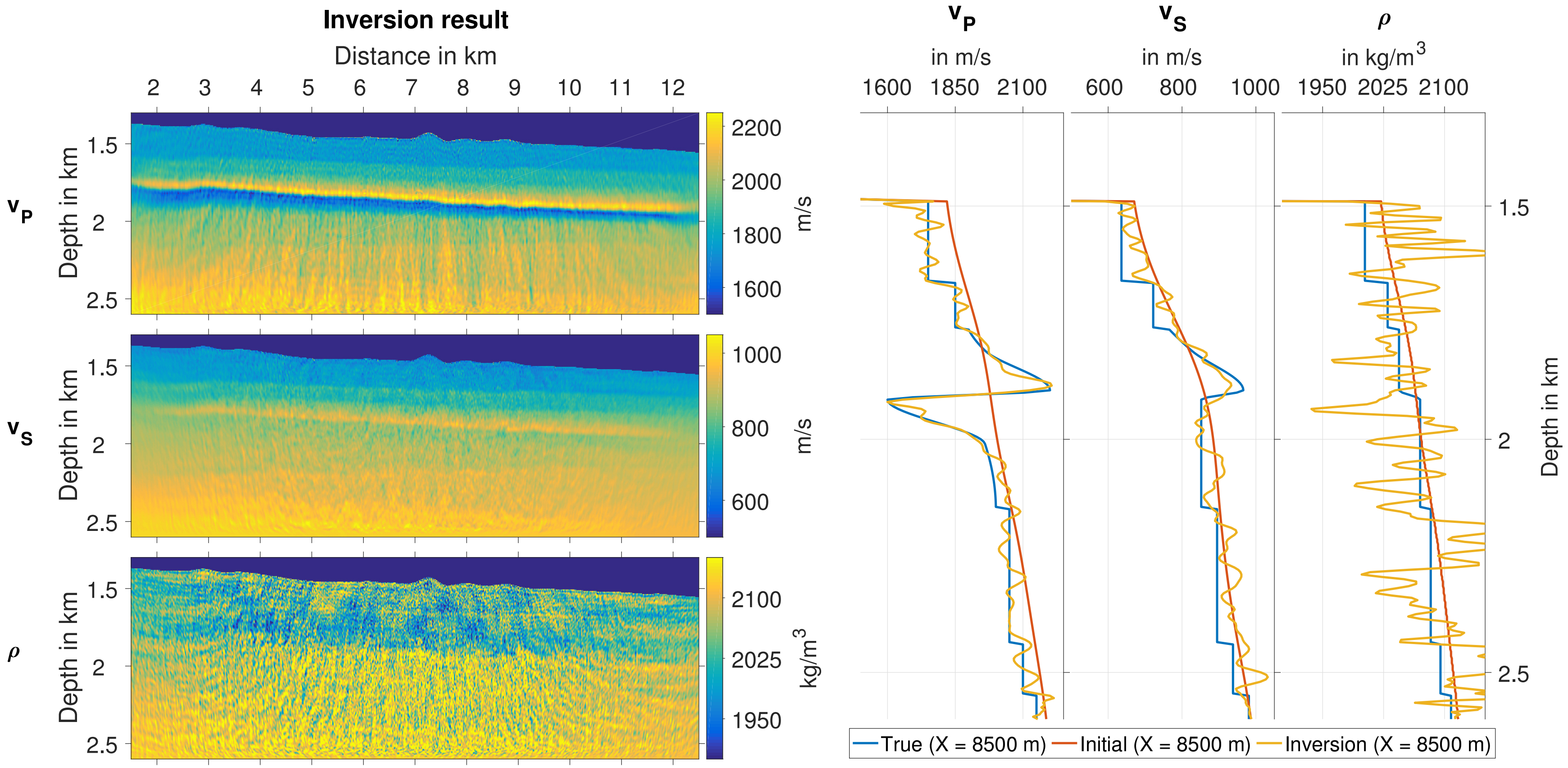

Figure A.5.: Result of the elastic FWI reconstruction test using initial models of v_P, v_S and ρ with a variation of +4%. Left: 2D v_P, v_S and ρ inversion results; right: 1D cross sections at $X = 8.5$ km for the true, initial and inversion result model.

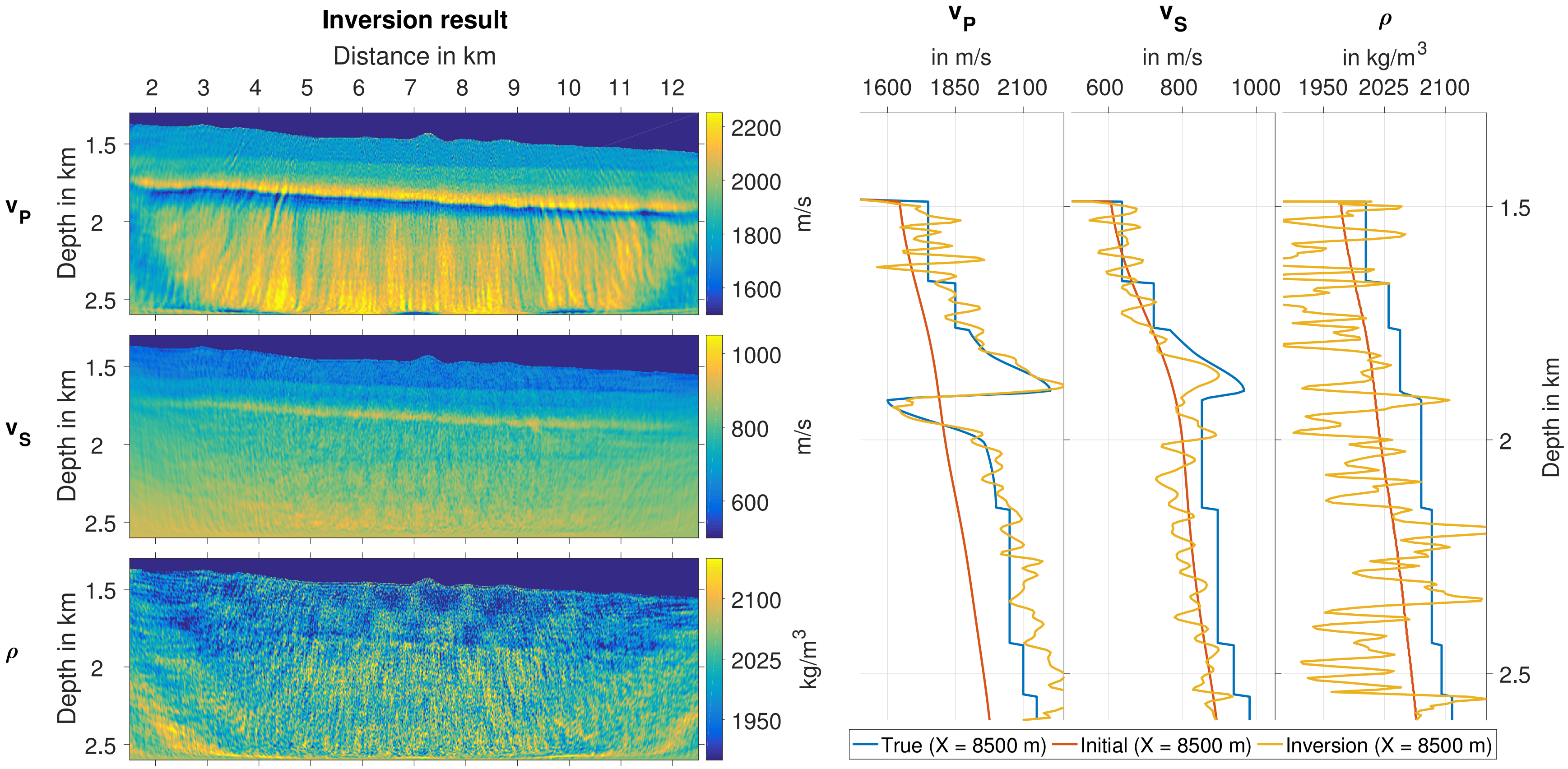

Figure A.6.: Result of the elastic FWI reconstruction test using initial models of v_P, v_S and ρ with a variation of -6%. Left: 2D v_P, v_S and ρ inversion results; right: 1D cross sections at $X = 8.5$ km for the true, initial and inversion result model.

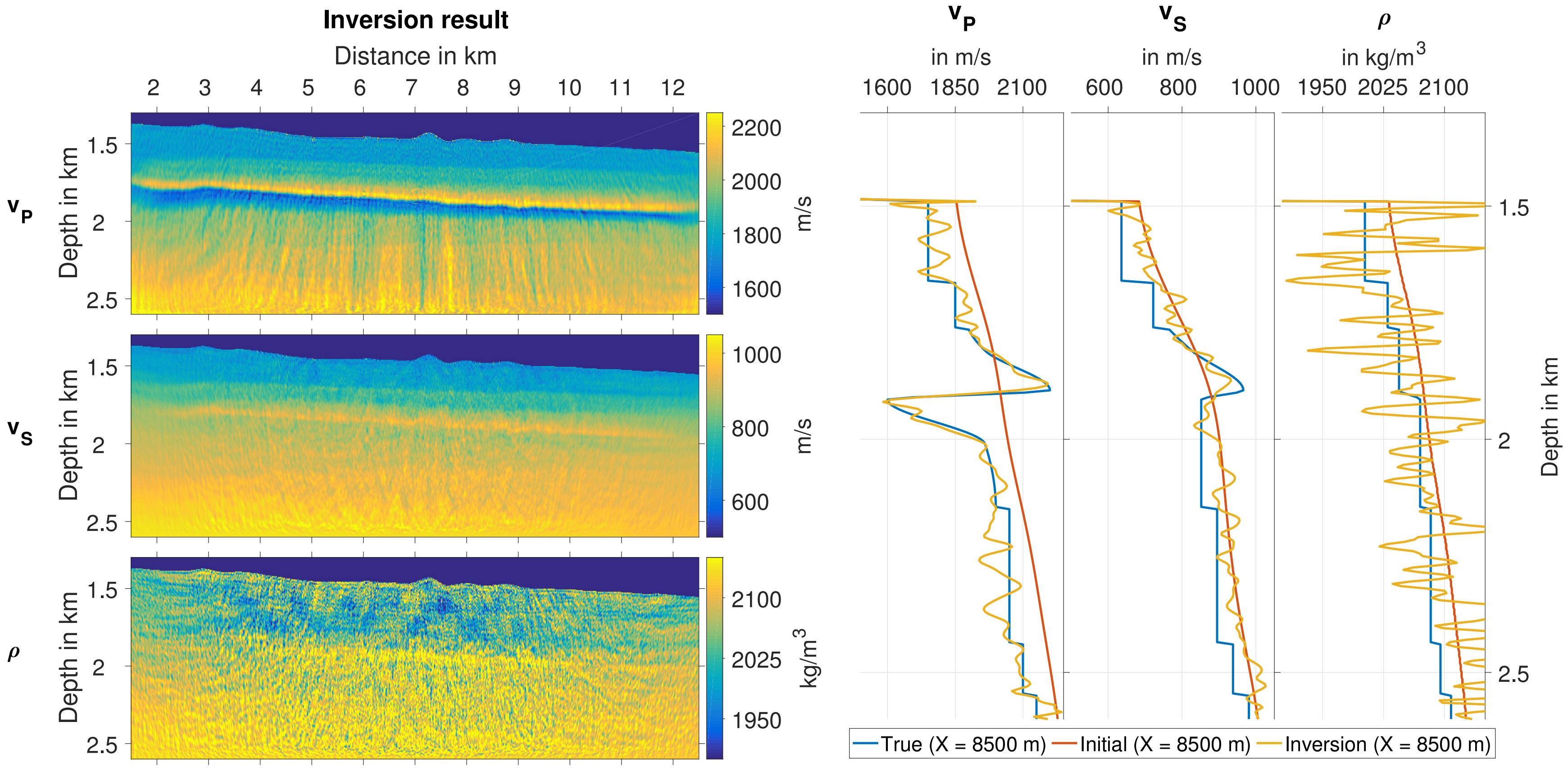

Figure A.7.: Result of the elastic FWI reconstruction test using initial models of v_P, v_S and ρ with a variation of +6%. Left: 2D v_P, v_S and ρ inversion results; right: 1D cross sections at $X = 8.5$ km for the true, initial and inversion result model.

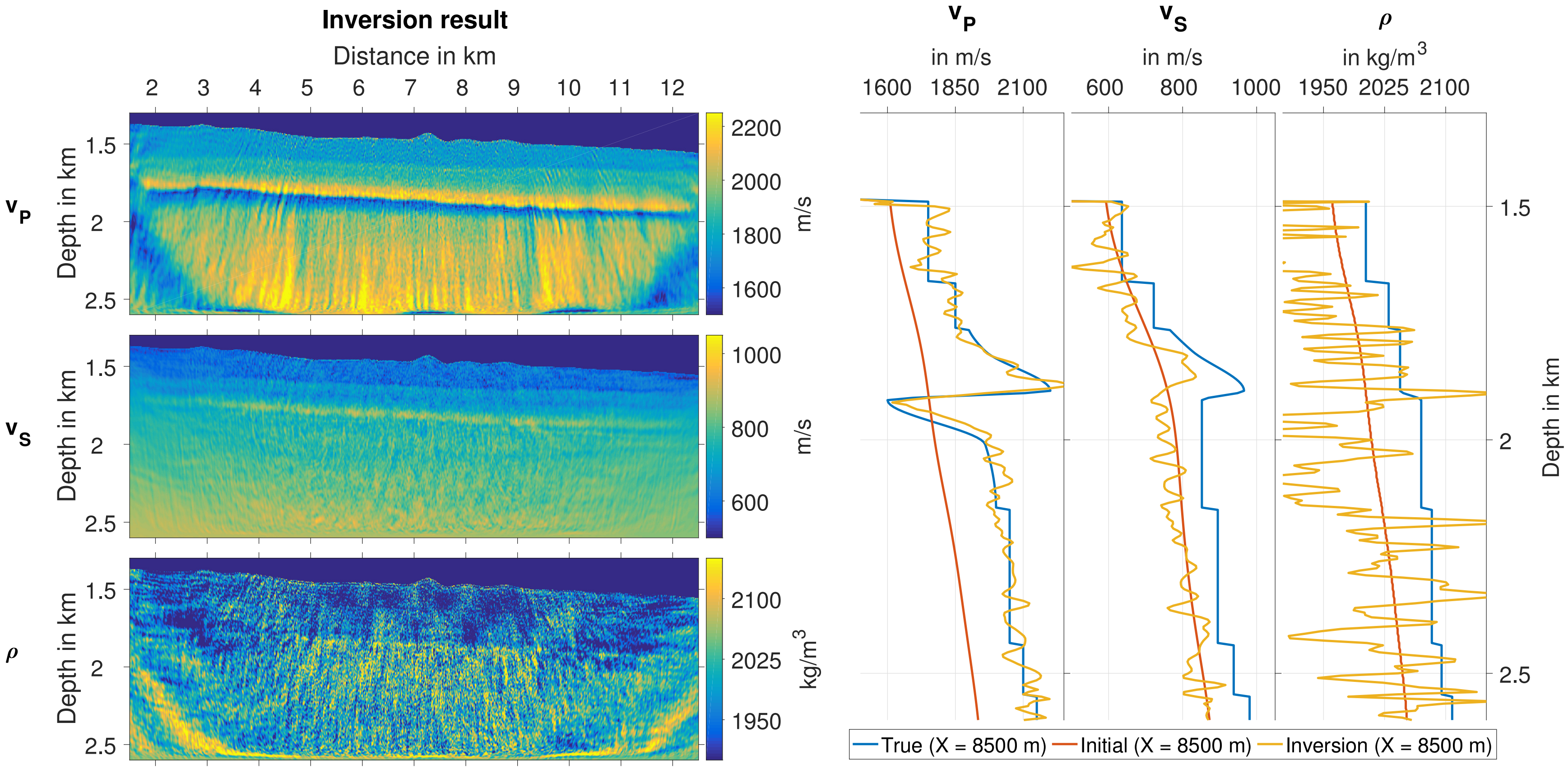

Figure A.8.: Result of the elastic FWI reconstruction test using initial models of v_P, v_S and ρ with a variation of -8%. Left: 2D v_P, v_S and ρ inversion results; right: 1D cross sections at $X = 8.5$ km for the true, initial and inversion result model.

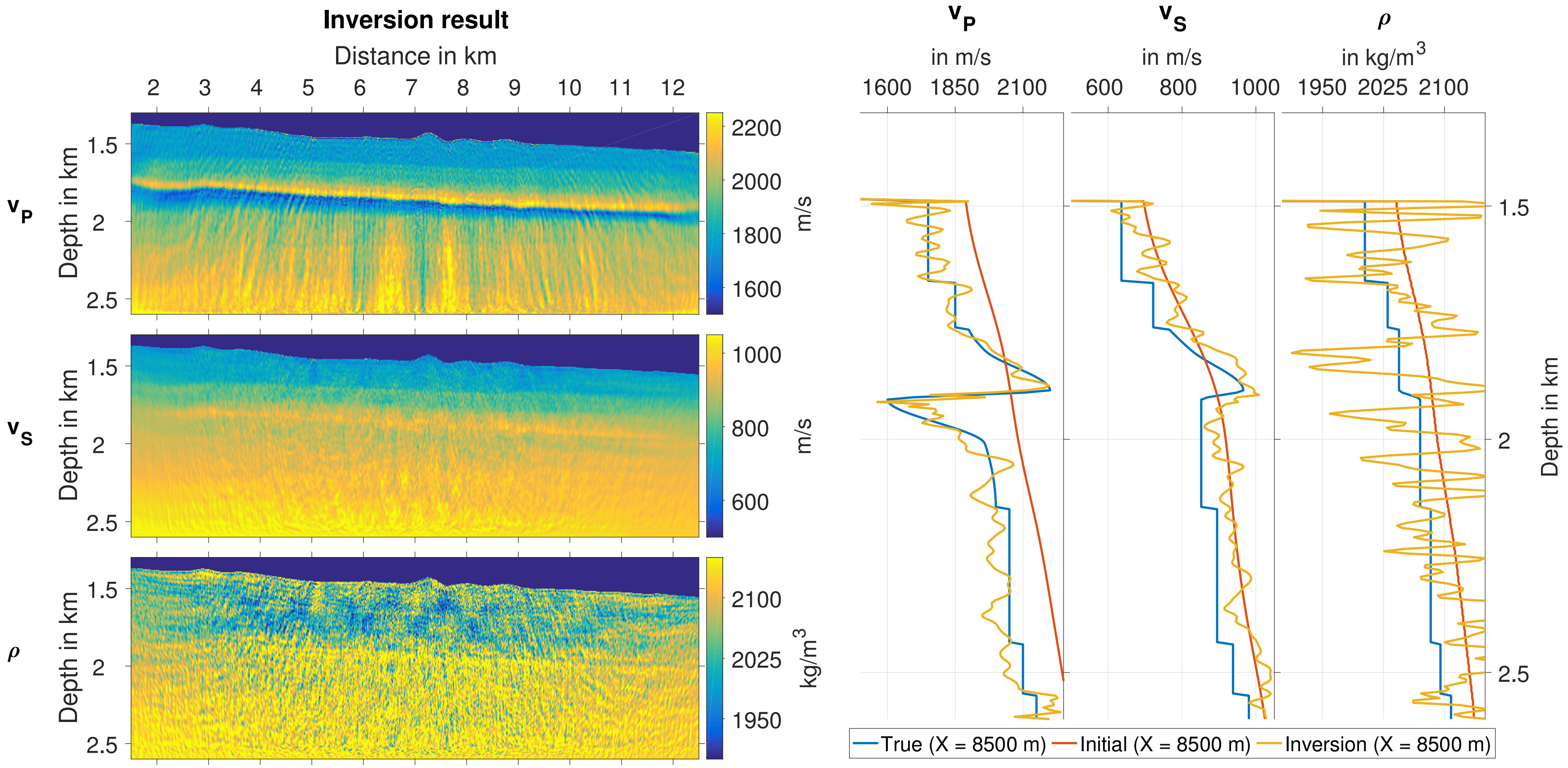

Figure A.9.: Result of the elastic FWI reconstruction test using initial models of v_P, v_S and ρ with a variation of +8%. Left: 2D v_P, v_S and ρ inversion results; right: 1D cross sections at $X = 8.5$ km for the true, initial and inversion result model.

A.5. Effects of time windowing during FWI

Sometimes, bad data quality or correlating noise prevents the successful convergence of FWI and makes the application of time-windows necessary. Therefore, we test multiple time-windows to evaluate, if they have any consequences on the FWI result itself. First, we use a time-window that mutes every signal but the multiple reflections in case the direct wave and the refracted waves are unusable (fig. A.10; number 2). The second time-window is shown in figure A.10 (number 1) and prevents all signals except the refracted waves. Finally, we use both, the refracted waves as well as the multiple reflections (fig. A.10; number 1 and 2) and even use it with the noise contaminated data from chapter 5.4.

The results of the inversions are illustrated in figure A.11. We can only observe a slight loss in S-wave resolution if we omit the refracted waves and only use the multiple reflections. The lateral inhomogeneities in the deeper part of the P-wave velocity model are marginally enhanced when solely using refracted waves. There is no observable difference in the inversion result if we use both, the refracted waves and the multiple reflections. Finally, we observe neither positive nor negative effects when we apply the time-windows 1 and 2 to noise contaminated data, as shown in figure A.12.

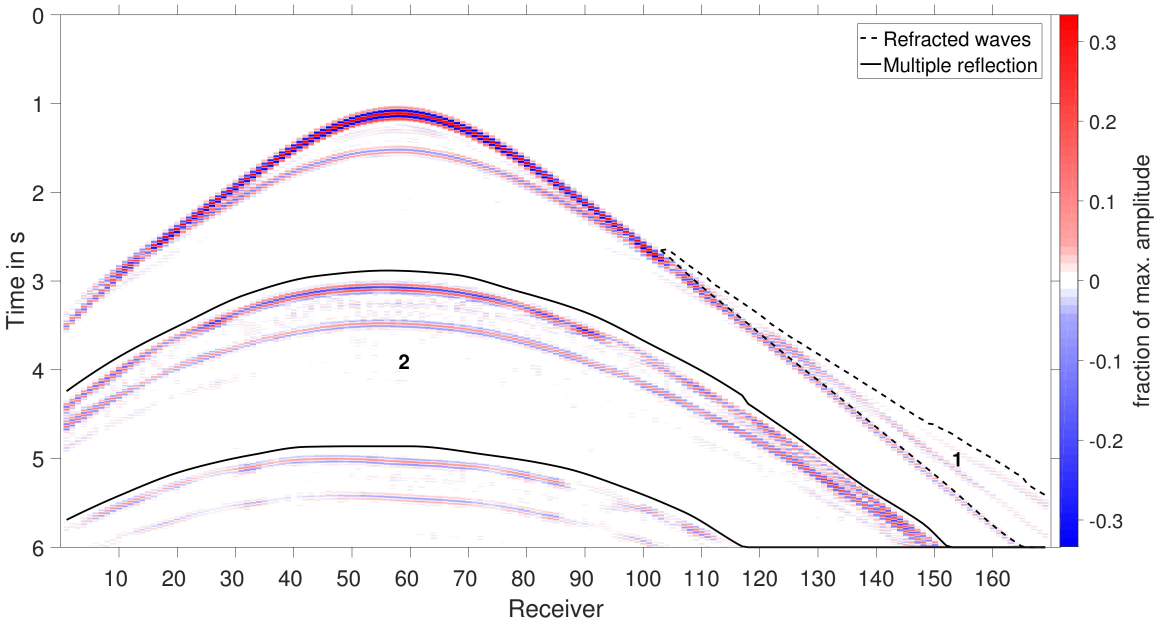

Figure A.10.: Time-windows we test with FWI; 1: we use only the refracted waves; 2: we use only the multiple reflections; 1+2: we use both, the refracted waves and the multiple reflection but neglect the direct wave.

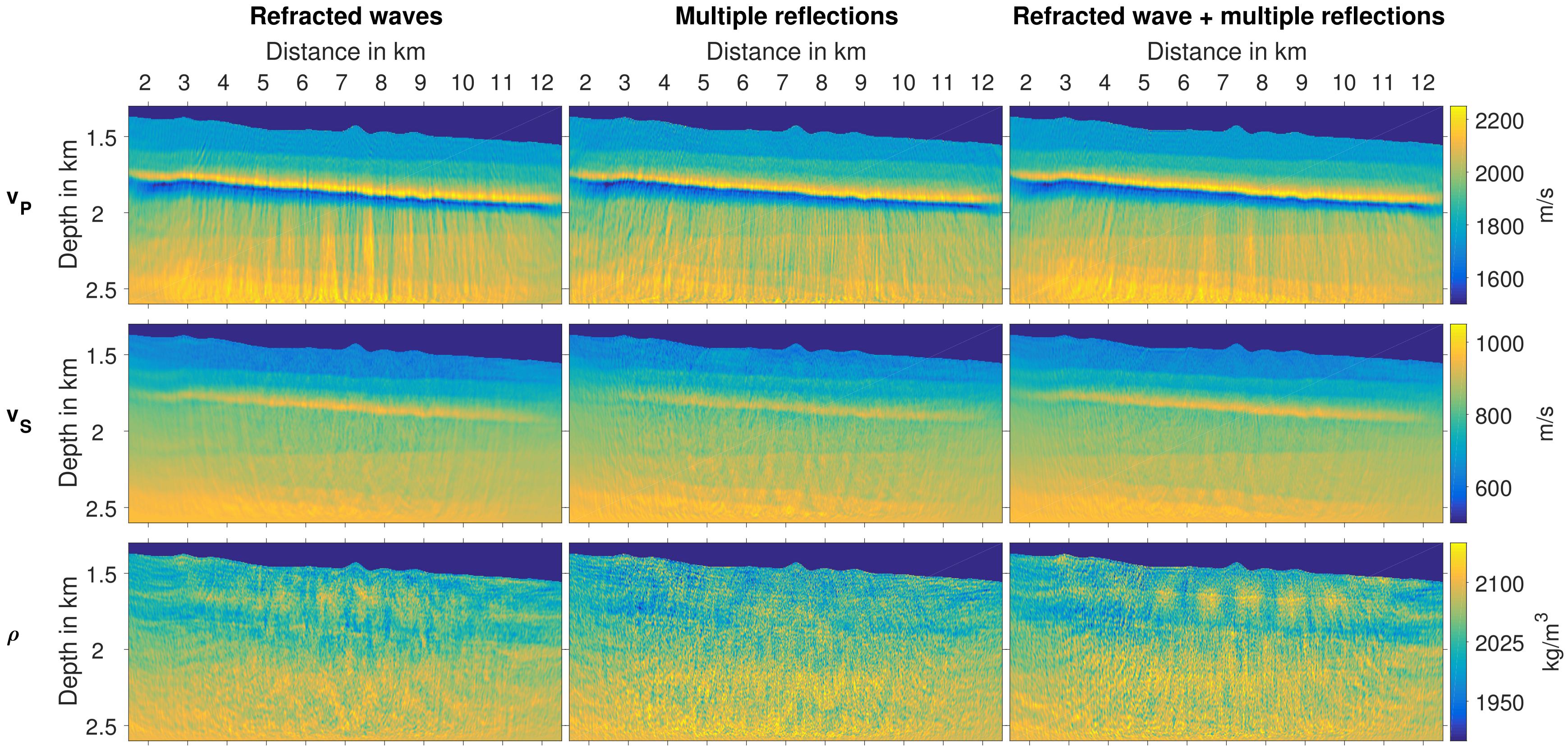

Figure A.11.: Comparison of the elastic FWI results while using time-windows. Illustrated are the final FWI results of v_P (top row), v_S (middle row) and ρ (bottom row).

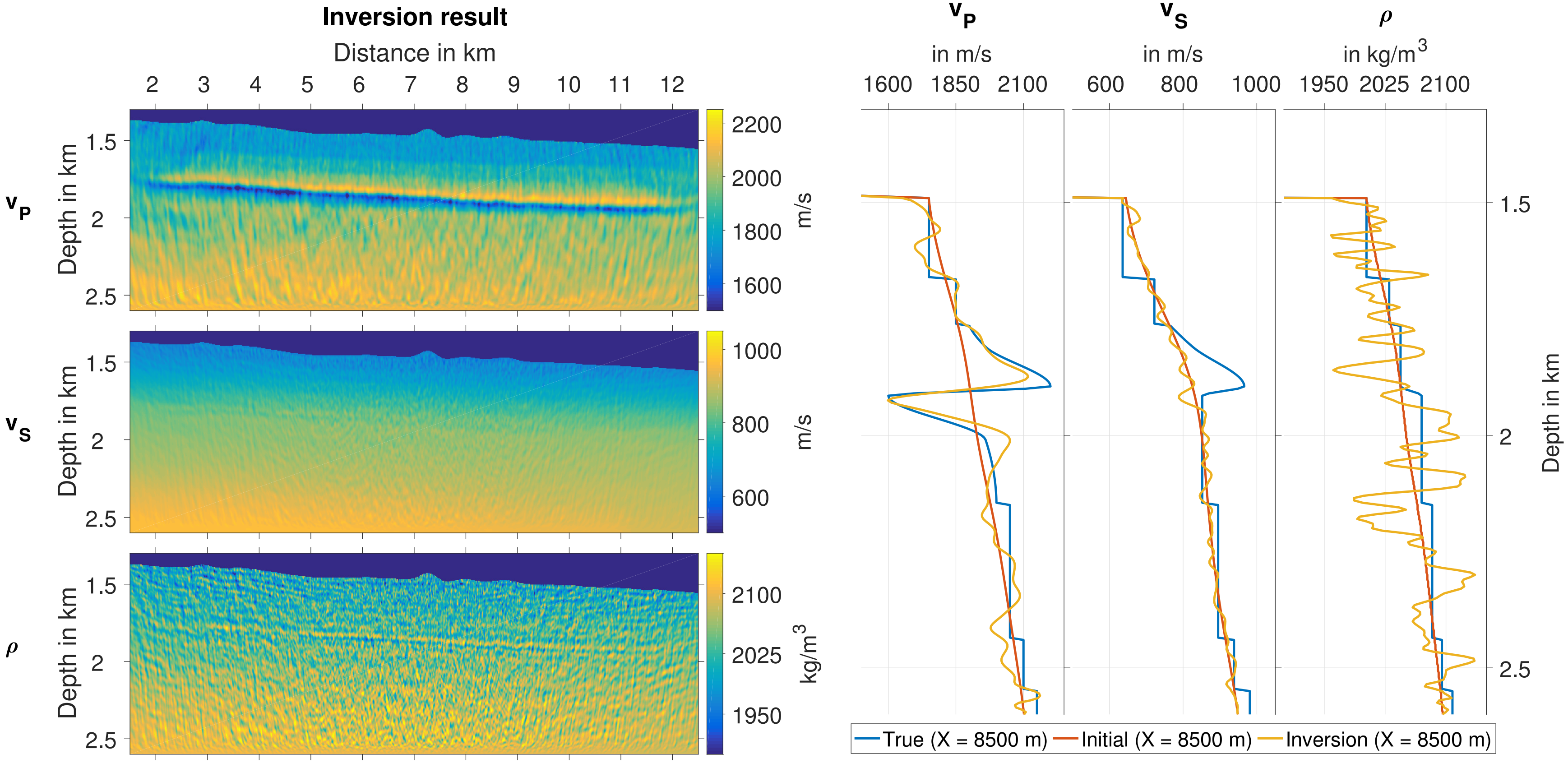

Figure A.12.: Result of the elastic 2D FWI with noise contaminated data while using time-windows 1 and 2. Illustrated are the final FWI results of v_P, v_S and ρ on the left with cross-sections at $X = 8500\,\mathrm{m}$ of the true, initial and final inversion model on the right.

Danksagungen

Als Erstes möchte ich mich bei Thomas Bohlen für die Idee und die Betreuung dieser Arbeit bedanken. Weiterhin bedanke ich mich bei Joachim Ritter für die Übernahme des Korreferats.

Der Arbeitsgruppe "Angewandte Geophysik" danke ich vielmals für die hilfreichen und interessanten Diskussionen rund um das Thema Seismik, insbesondere wenn es um das Verstehen und Debuggen des Codes ging. Bei Claudia Payne möchte ich mich für die Hilfe bei der Bezwingung der Bürokratie bedanken.
Besonderer Dank geht an Laura für das gewissenhafte Korrekturlesen der Arbeit und die vielen Denkanstöße ohne die ich manchmal nicht weiter gekommen wäre. Danke, dass du diese Arbeit betreut hast.

Vielen Dank auch an Alexandra für das Korrekturlesen und die Ablenkung während der letzten Monate, die mir durch etliche Motivationslöcher geholfen hat. Danke für deine zweifellose Unterstützung!

Acknowledgments

This work is carried out in the framework of the SUGAR-III project and is funded by BMWi (grant number 03SX381C). I would like to thank Timo Zander and Anke Dannowski from GEOMAR for providing me with the horizons and velocity models of the seismic survey in the Black Sea.